NAME	ADDRESS	DATE

THE FLORIDA STATE UNIVERSITY

COLLEGE OF ARTS AND SCIENCES

A NUMERICAL STUDY ON THE INFLUENCE OF THE MID-ATLANTIC

RIDGE ON NON-LINEAR BAROTROPIC AND FIRST MODE BAROCLINIC

ROSSBY WAVES GENERATED BY SEASONAL WINDS

by

BERNARD BARNIER

A Dissertation submitted to the
Geophysical Fluid Dynamics Institute
in partial fulfillment of the
requirements for the degree of
Doctor of Science

Approved:

James J. O'Brien
Professor Directing Dissertation

Albert Barcilon

Christopher Tam

George Weatherly

December, 1986

Abstract

A numerical model simulation investigates the influence of the
mid-Atlantic ridge on non-linear barotropic and first-mode baroclinic
Rossby waves generated by seasonal wind fluctuations. The north
Atlantic is simulated by a square-box, two-layer quasi-geostrophic
model. The bottom topography is ridge-like and compromises the QG
approximation and the actual shape of the ridge. Sponge layers
protect all boundaries except the eastern one from wave reflexion.
The model is forced by a purely fluctuating wind stress curl derived
from the most significant EOF's of the FGGE winds. A flat bottom and
a ridge experiment are compared. The topography is an important
source of barotropic variability for the eastern basin. The
topographic Rossby waves generated over the ridge, either by wave
reflexion or by direct wind forcing, account for at least 50% of the
barotropic variability of that basin. Their frequencies range from
0.01 to 0.05 cpd.

In both experiments the eastern boundary is an important source
of annual-period baroclinic Rossby waves. Wavetrains having a
wavelength of about 1060 km and a westward phase speed around 3.4 cm
sec^{-1} propagate energy westward at 3 cm sec^{-1}. In the flat bottom
experiment a source of directly wind-forced baroclinic waves of
annual period is found in the middle of the basin. Their amplitude

is smaller and they have a noticeable northward phase propagation resulting in a southward group velocity component. The topography blocks the waves coming from the eastern boundary but generates new wavetrains whose phase vector is almost normal to the ridge crest. Those waves propagate energy mostly westward at 2.9 cm sec^{-1}. The northern waves are out of phase with the southern ones because of the structure of the dominant wind pattern over the ridge region where they are generated. All waves have a small group velocity component in the meridional direction. It is northward (at 0.34 cm sec^{-1}) for the northern waves and southward (at 0.32 cm sec^{-1}) for the southern waves.

ACKNOWLEDGEMENTS

It is with the deepest respect that I thank Dr. James J. O'Brien as my major professor. In addition to his countless support, encouragement and advising, he made my stay in Tallahassee an unforgettable, enriching and pleasant experience to my family and I. I wish to express my deepest gratitude to Dr. Christian LeProvost. Besides his comments and enthusiasm, his voluntary support made possible the time-sharing between the Florida State University and the Institut de Mécanique de Grenoble this work has required. I would like to acknowledge Drs. A. Barcilon, D. Nof, C. Tam and G. Weatherly for serving on my doctoral committee.

My sincere appreciation extends to Ruth Pryor for her constant assistance and to Jim Merritt at FSU and the people of the CCVR in Palaiseau for their help in eluding the tricks the computers played on me. I thank Rita Kuÿper who typed the manuscript with skill and patience. I also wish to mention every member of MASIG.

It is with the deepest affection that I thank my wife Cathy for

giving me so much support, and my young son Guillaume for the many joyfull moments he brings us, keeping our spirit high. My family and I return affectionate thanks to our dearest friends Marie-Paule and William Howell with whom we shared the ups and downs of these past years.

TABLE OF CONTENTS

APPENDIX A: MEAN AND EDDY ENERGETICS OF A TWO-LAYER QUASI-GEOSTROPHIC OCEAN MODEL

APPENDIX B: TESTING A SPONGE-LAYER IN A TWO-LAYER QUASI-GEOSTROPHIC MODEL

ABSTRACT

LIST OF FIGURES

obtained by repetition of the one year long record of

the forcing composed of the four EOF's. Series are located

at point 3 (left) and point 6 (right) of Fig. 2.

They start December 1st. Both series present an

alternance of high winter and low summer amplitude.

Spectra look rather white. Annual variability accounts

for 10% of the total variance in series 3 and 16%

in series 6. Seasonal variability is dominant at

60 days in series 3 (20% of total variance) and

at 30 days in series 6 (18% of total variance).

Variance sharply decreases at frequencies larger

I. INTRODUCTION

In the last twenty years considerable progress has been made in observing and understanding the general circulation and eddy variability of the mid-latitude ocean. The gross features of the general circulation (gyre circulation, intensified western boundary current) have been known for more than thirty years (Sverdrup, 1947; Stommel, 1948; Munk, 1950). The observations of the eddy variability are more recent and are linked to the development of new observational tools and new techniques in data analysis and numerical modeling, supported by the increasing capability of computers.

The dynamical and energetical importance of variable currents was first suggested by the ARIES expedition (1959-1960) near Bermuda (Swallow, 1961). Since then, especially during the decade of the 1970s, the scientific community has made a considerable effort to observe, describe, and understand the variable oceanic circulation, its generation, and its interaction with and contribution to the larger scale circulation. These investigations include in-situ experiments like MODE, POLYMODE, NEADS and others, numerous analytical and numerical process studies, and the development of numerical models of general circulation like EGCMs (Eddy-Resolving General Circulation Models). Although many of the fundamental questions still remain to be answered, important results have been

obtained. They are extensively summarized in the volume <u>Eddies in</u> <u>Marine Sciences</u> (Robinson, 1983).

A major result is the identification of a primary mechanism for generation of eddies by nonlinear internal processes related to baroclinic and/or barotropic instability. This mechanism occurs in limited regions of the ocean near strong flows (western boundary currents, their mid-latitude extension, and their recirculation). Generated eddies then populate, by transport and radiative processes, larger regions of the ocean as the sub-tropical and the sub-polar gyres. As explained by Robinson (1982) and Schmitz, Holland, and Price (1983), this knowledge is a synthesis of the results obtained by the observed geographical distribution of the eddies and the results carried out by the EGCM experiments.

Many other important results have been obtained by analyzing many varieties of data collected during the 1970's. The geographical distribution of the eddy kinetic energy and eddy potential energy have been established (Wyrtki, Magaard, and Hager 1976; Dantzler, 1977). As noted above, eddy energy is large near strong currents indicating regions of internal production. But the existence of large pool of low eddy kinetic energy in the ocean interior suggests other eddy generation mechanisms. Recent results by Gould and Cutler (1980) and by Dickson, Gould, Gurbutt, and Killworth (1982) on the eastern North Atlantic suggest that direct time-dependent wind forcings could generate variable currents that compose a quasi-

uniform eddy background in the interior of the sub-tropical gyre.

The mechanism of generation of variable currents by variable wind-forcings has been widely studied. The early analytic and deterministic study of Phillips (1966), the more recent analytic and stochastic study of Frankignoul and Muller (1979), and the numerical study of Willebrand, Philander, and Pacanowski (1980) illustrate the variety of methods used to investigate this problem.

Phillips' study investigated the quasigeotrophic response of a flat-bottom ocean to a deterministic, time-dependent wind stress. The study attempted to explain the low-frequency variability observed near Bermuda during the period 1959-60. Though his model underestimated the response compared to observations, it pointed out important features of the zonal partition of kinetic energy in the ocean. For instance, the maximum variability occurs at its longest periods near the western boundary and at progressively shorter periods away from the boundary.

Frankignoul and Muller (1979) used an analytic, stochastic model to evaluate the rate at which a homogeneous and stationary wind forcing transfers energy into the mesoscale, quasigeostrophic linear motions of a flat-bottom ocean. They found that this rate is smaller but of a comparable order with the rate at which energy is transferred from the mean circulation to the eddies by means of baroclinic and barotropic instabilities. They concluded that, far enough from the internal production regions, direct wind forcing

might be an important mechanism of eddy generation.

Willebrand et al. (1980) studied the ocean response to the excitation of large-scale wind fluctuations using a numerical stochastic model. They found that the variability is more intense in the western part of the basin and near major topographic features (such as the mid-Atlantic ridge). At periods ranging from a week to a month, the ocean response is dominated by (topographic) Rossby waves, and it appears that high-frequency topographic waves can be resonantly generated and trapped near special topographic features (as the Azores' rise).

However, these studies appeared to be handicapped by the lack of knowledge of the wind field over the ocean. One might say that the wind forcing process of eddy generation is understood less well than the internal production process.

A phenomenon that might compete with (and perhaps dominate) direct wind forcing is the radiation of eddy energy from regions of high internal production into the interior ocean (Wunsch, 1981). The Price and Rossby's (1982) observation, at site LDE (70°W, 30°N), of a planetary wave radiating energy eastward is strong evidence of the reality of this radiative phenomenon.

Except for the work of Willebrand et al. (1980), the papers cited do not explicitly consider the large-scale bottom topography. This latest study showed that the bottom topography may have an important influence on eddy generation by direct wind forcing. More

recently, in a survey on mid-latitude mesoscale variability, Schimtz et al. (1983) insist that the seasonal variability observed in the eastern North Atlantic by Gould and Culter (1980) and by Dickson et al. (1982) can be interpreted as a "modulation of wind forced topographic waves". Besides, according to Barnier (1984a), it seems evident that the radiation of eddy energy from regions of high internal production may be strongly influenced by large topographic features like the mid-Atlantic ridge.

Another source of eddy variability that is certainly influenced by large-scale mid-ocean topographic features (and on which this dissertation focuses) is the energy radiation by barotropic and baroclinic Rossby waves generated at the eastern boundary. The process involved in the generation of free Rossby waves at a meridional eastern boundary was discussed by Anderson and Gill (1975). If the forced flow at the boundary does not fulfill the boundary conditions by itself, which is generally the case in the ocean, we expect generation of free Rossby waves to balance out the forced flow normal to the coastline. The waves propagate westward out of the forced region. This process has gained interest lately, since observational evidence of baroclinic Rossby waves has been found in the Pacific Ocean. Several analyses of the mesoscale variability of the thermocline of the mid-latitude North Pacific demonstrated the importance of the annual and interannual baroclinic Rossby waves (Bernstein & White, 1974; Emery & Magaard, 1976; White,

1977). Kang and Magaard (1980) presented convincing evidence for
annual period baroclinic Rossby waves in the central North Pacific.
These waves, as they appear in the temperature records of the upper
ocean, have a first baroclinic mode vertical structure. Their
typical phase speed is northwestward at 1 cm sec^{-1}, and their group
velocity is toward the southwest.

Several studies attempted to identify a generation mechanism for
these waves. Among the most successful ones was an eastern lateral
boundary, since an unbounded linear ocean model cannot excite motions
on a scale that is very different from those of the forcing. White
and Saur (1981) explained the generation of annual Rossby waves in
the central Pacific by the annual variations of the wind along the
coast of California. They modeled the first baroclinc mode Rossby
wave with a one-dimensional long wave equation.

Also involving the generating process discussed by Anderson and
Gill, Mysack (1983) proposed a mechanism for the generation of these
waves. He showed that annual north-south fluctuations in the eastern
boundary current off Vancouver Island can efficiently generate first
baroclinic mode Rossby waves throughout the central Pacific. He used
a two-dimensional, reduced-gravity, long wave equation model, and he
was able to favorably compare the far field wave solution with
observations.

Recently, Cummins, Mysak, and Hamilton (1986) simulated the
generation of the annual Rossby wave field over a large part of the

North Pacific off California. Their model is based on the linear, reduced-gravity, two-dimensional Rossby wave equations in spherical coordinates. It includes a realistic representation of the geometry of the eastern boundary, and it is driven by a wind-stress curl of annual period derived from real data. They identified sources for Rossby waves at three different locations. Two are adjacent to the eastern coast of Oregon and California-Baja, and a third one is in the mid-ocean off the Oregon coast. The sources near the boundary involve the indirect generation mechanism we already mentioned, while the mid-ocean source involves direct resonant wind forcing. From this study it seems that the geometry of the coast does not play a fundamental role in the locations of the sources, while the wind pattern appears to be important.

Compared to the Pacific Ocean, similar studies are rather scarce in the North Atlantic. A reason may be the lack of observational evidence of annual-period baroclinic Rossby waves, except for that of Bray (1980) in the Gulf of Biscay. However, there are many hints of a strong wind-correlated seasonal variability in the eastern North Atlantic (Gould & Culter, 1980; Dickson et al., 1982). It is possible that the mid-Atlantic ridge has a very important role in modifying the signal of Rossby waves. Also, unlike the Pacific Ocean, the Atlantic may not be wide enough for a far field of Rossby waves to exist. In Lippert and Kase's study (1985), it appeared that the Rossby wave energy-spectrum in its low-frequency band (less than

.5 cpy) is not free from the influence of an eastern boundary, even in the vicinity of a western boundary.

Despite the lack of observational evidence, a few studies attempt to investigate the generation of annual-period Rossby waves in the North Atlantic. Krauss and Wubber (1982) used numerical methods to solve the dispersive linear Rossby wave equations, taking into account all the vertical modes. They forced the model with a wind field of annual period produced by the Bunker's data set over the eastern north Atlantic. The β-plan model extends from 0°N to 50°N. They found that the wind field produces a forced response to the eastern boundary which is dominated by the barotropic and the first baroclinic modes. Away from the boundary the energy radiates westward in the form of long, first-mode baroclinic Rossby waves of wavelength of about 1800 km.

Lippert and Kase (1985) investigated the influence of different wind-stress curl wavenumber-spectra on the direct forcing of baroclinic Rossby waves and modifications due to the presence of an eastern boundary. They confirmed the results of similar studies that a forcing having a band-limited, white-noise frequency and wavenumber spectrum forces a response having an equivalent white-noise kinetic energy spectrum in the frequency range of baroclinic Rossby waves. When they included an eastern boundary in the model, they found a monotonic increase in Rossby wave energy towards the interior ocean due to free waves emanating from the boundary. They noted that, in

the vicinity of the boundary, the structure of the response given by
a stochastic model was not much different from that obtained with a
deterministic model. They concluded that the eastern boundary plays
a dominant role for the dynamics in the mid-ocean and eastern basins.

However, none of these studies includes the effects of the
large-scale bottom topography. The contribution of the mid-Atlantic
ridge to the mesoscale variability in the North Atlantic is still
unclear. Wunsch (1983) concludes that the main effect of the ridge
is a damping of the deep circulation, leaving the upper ocean
untouched. This idea seems to be strengthened by recent
observational results from Krauss and Kase (1984). From satellite-
tracked surface buoys released in the north central Atlantic, they
showed that the North Atlantic current appears as the main source of
eddy energy, while the mid-Atlantic ridge is not a source of eddy
energy.

Many questions remain to be answered. Do the directly wind-
forced topographic waves that are suspected to exist due to the
presence of the ridge have a noticeable signature in the mid-ocean?
How efficiently does the ridge block the energy radiating from the
western basin (a high eddy energy production region) and from the
eastern boundary (through westward propagating Rossby waves generated
at the coast). In the present work we try to answer, in part, these
questions.

The aim of the present study is to investigate, in a numerical

model simulation, the propagation across the North Atlantic of the barotropic and first mode baroclinic Rossby waves generated at the eastern boundary by a wind forcing obtained from real wind data. Special attention is given to the effects of the mid-ocean ridge on both the propagation and generation of Rossby waves in the open ocean. Non-linear effects are included.

The second section of the study presents the ocean model including the model geometry, the governing equations, and the wind forcing. The third section presents the results of a flat bottom experiment, also called the reference experiment. It describes the general features of the model response in the case of a flat bottom ocean. The barotropic and baroclinic circulations are analyzed, focusing on the generation by the wind of barotropic and first mode baroclinic Rossby waves. The forth section presents the results of an experiment similar to the reference experiment except for the inclusion of a mid-ocean ridge. The analysis of the model response follows the same procedure as in the flat bottom case, but, in addition, the results of both experiments are compared. Section five is a conclusion which discusses the effects of the mid-ocean ridge on the generation and propagation of Rossby waves in the North Atlantic. Appendix A details the pointwise energy budgets that are used in sections 3 and 4 to analyze the model results. Appendix B shows how to design and test a sponge layer which damps the waves that enter it. Such layers are used in the model at the zonal and

western boundaries to prevent the reflexion of Rossby waves. Also,
these boundaries act somewhat like open boundaries.

II. DESCRIPTION OF THE MODEL AND THE EXPERIMENTS

The purpose of this study is to investigate the radiation of energy from wind-driven Rossby waves generated at the eastern boundary of an ocean that simulates the North Atlantic. A model resolving the barotropic and first baroclinic mode seems adequate. Indeed, one expects most of the wind input energy to be found in these two modes, as in the study of Krauss and Wubber (1982). Therefore, this work is driven by a two-layer, quasi-geostrophic model similar to Holland's (1978). In fact, the basic numerical code was provided by Dr. Holland. The governing equations relative to this model are given in the next sub-section.

Some modifications were required to adapt the original model (a square box ocean model) to this problem. A variable bottom topography and a variable wind-stress curl were added. A damping layer was introduced at the western limit of the ocean model in order to prevent wave reflexion at the western boundary and the build up of the western boundary current. The introduction of such a western damping layer assumes that the short reflected Rossby waves do not travel back to the east but contribute to the build up of the western boundary current (Pedlosky, 1965). This assumption also leaves the solutions free of perturbations coming from the west.

The bottom topography is ridge-like and crosses the basin from

south to north. Intersection of the f/h contours with the solid boundaries of the square box basin is avoided by progressively reducing the ridge height to zero before it reaches the boundaries. The southern and northern boundaries are also designed as damping layers. The damping neutralizes the turning around of the topographic waves where the ridge disappears. The model geometry and the design of the damping layers are described in following sub-sections.

The forcing that drives the model is derived from real wind data. Barnier (1986) performed an EOF analysis of one year of wind-stress curl data obtained from the FGGE winds. It was found that 44% of the variance is contained in four significant eigenvectors, the higher order eigenvectors becoming noise quickly. These four EOFs, after projection on the model basin, are combined to construct the driving forcing. Thus, the large-scale spatial patterns of the actual forcing are conserved, while the amount of data needed during the integration is reduced considerably. The geographical distribution of the forcing with respect to the geographical distribution of the bottom topography and the eastern boundary is maintained. An important attribute of a forcing characterized by a few (but well-identified) spatial patterns, which are representative of important climatic features, is the possibility of relating some features of the ocean response to some characteristic features of the wind forcing. The ocean variability which is related to that portion

of the wind data that is contained in the lower order EOFs (56%) will
not be investigated. Details on the wind-forcing are given in a
following sub-section.

A. The Governing Equations of the Two Layer Model

Basically, the model is the one presented by Holland (1978).
The vertical structure of the model is schematically shown in Fig.
1. It is a two-layer ocean with a rigid top and a variable bottom
topography on the usual β-plane in a closed basin. The governing
equations are the non-linear potential vorticity equations for the
two layers, coupled by the continuity equation applied at the
interface.

$$\partial/\partial t(\nabla^2 \psi_1) = J(f + \nabla^2 \psi_1, \psi_1) - f_0 w_2/H_1 + F_1 + \text{Curl } \tau/H_1 \qquad (1)$$

$$\partial/\partial t(\nabla^2 \psi_3) = J(f + f_0 h/H_3 + \nabla^2 \psi_3, \psi_3) + f_0 w_2/H_3 + F_3 + B_3 \qquad (2)$$

$$\partial/\partial t(\psi_1 - \psi_3) = J(\psi_1 - \psi_3, \psi_2) - g' w_2/f_0 \qquad (3)$$

The notations are as follows. $H_{1,3}$ are the constant thickness of
layers 1, 3, respectively. The total depth is $H = H_1 + H_3$, $h(x,y)$
is the height of the bottom topography (Fig. 1), $\psi_{1,3}$ are the stream-
functions at the various levels shown in Fig. 1. The horizontal
velocity components are $u_{1,3} = -\partial \psi_{1,3}/\partial y$ and $v_{1,3} = \partial \psi_{1,3}/\partial x$. At
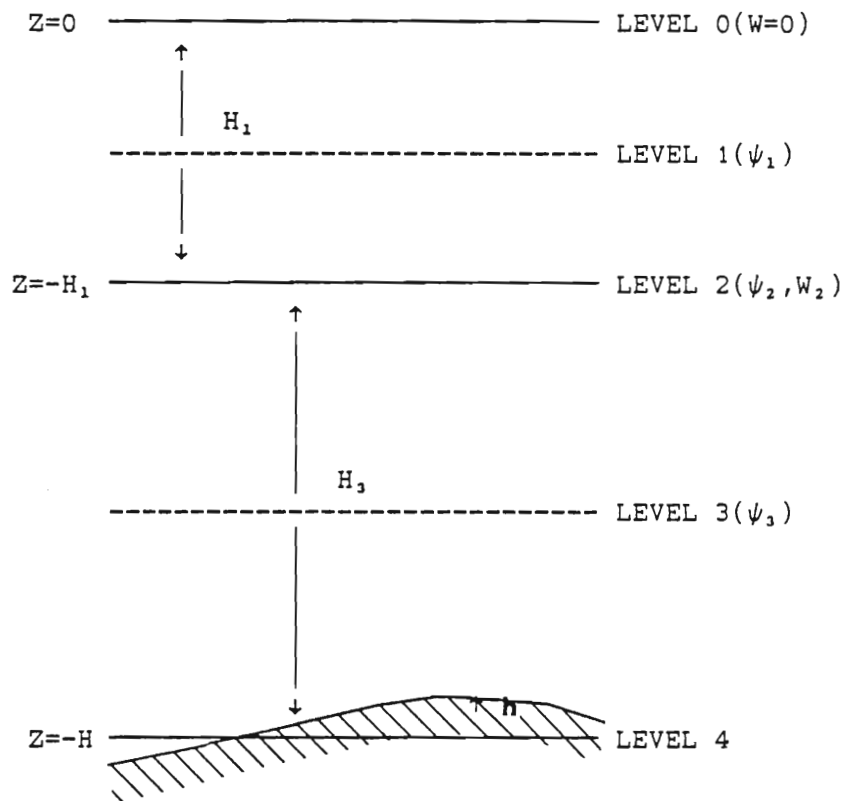
Fig.1 . Diagram for the vertical structure of the
two-layer quasi-geostrophic model.

the interface, the vertical velocity is w_2, the streamfunction is given by $\psi_2 = (H_3\psi_1 + H_1\psi_3)/H$, and the deviation of the interface height, positive upward, is $h_2 = f_0(\psi_3 - \psi_1)/g'$. In the upper layer equation (1) the variable wind-stress curl, curl $\tau(x,y,t)$, is the vorticity input that drives the model. The dissipation of vorticity by lateral friction is represented by the biharmonic friction with constant eddy viscosity, $F_1 = - A_m\nabla^6\psi_1$. This type of friction damps the gird-scale waves very rapidly while it leaves the longer waves untouched.

In the lower layer equation (2), vorticity is dissipated by biharmonic friction $F_3 = - A_m\nabla^6\psi_3$ and energy by bottom friction simply represented by linear dissipation $B_3 = -\varepsilon_3\nabla^2\psi_3$.

J is the Jacobian operator. $f = f_0 + \beta(y - y_0)$ is the variable Coriolis parameter (y_0 refers to the mid-latitude of the basin where f_0 and β are calculated). $g' = g\Delta\rho/\rho_0$ is the reduced gravity (ρ_0 = lower layer density and $\Delta\rho$ = density difference between the two layers). The boundary conditions are no flow across the solid boundaries that define the ocean basin (slip boundary conditions).

A rigorous derivation of these equations can be found in Pedlosky (1964). Discussion of the finite difference intergration of this model can be found in Holland (1978).

B.   The Model Geometry and the Damping Layers

The physical ocean basin where the governing equations apply is represented by a basin of 4400 km by 4000 km (the unshaded region in Fig. 2).   The center point of this basin is the point $(x_o = 35°W, y_o = 37.5°N)$ outlined in Fig. 3.   The finite-difference grid-space is 40 km, which is fine enough to allow the numerical scheme to behave correctly in simulating the phase speed and group velocity of the planetary waves (Wajsowicz, 1986).   Thus the basin extends meridionally from 20°N to 56°N and, at mid-latitude (37.5°N), it extends zonally from 10°W to 60°W.   The corresponding values of the Coriolis parameter are $f_o = 0.8854 \times 10^{-4} \ sec^{-1}$ and $\beta = 1.8 \times 10^{-11} \ m^{-1} sec^{-1}$.

This particular geometry puts the mid-Atlantic ridge in a central position in the model.   (The average position of the mid-Atlantic ridge is about 35°W).   The bottom topography is simply represented by two abyssal plains of constant depth H = 5000 m on each side of a mid-ocean ridge (Fig. 2).   The model ridge compromises a realistic representation of the mid-Atlantic ridge and the quasigeostrophic approximation.   Its crest is obtained from the lat-long position of the ridge crest, which is projected on the model grid through a length-conserving projection with respect to the center point of the physical basin.   The quasigeostrophy imposes weak topography gradients.   Thus the height of the crest is largely underestimated and is taken to be 500 m at all latitudes except in
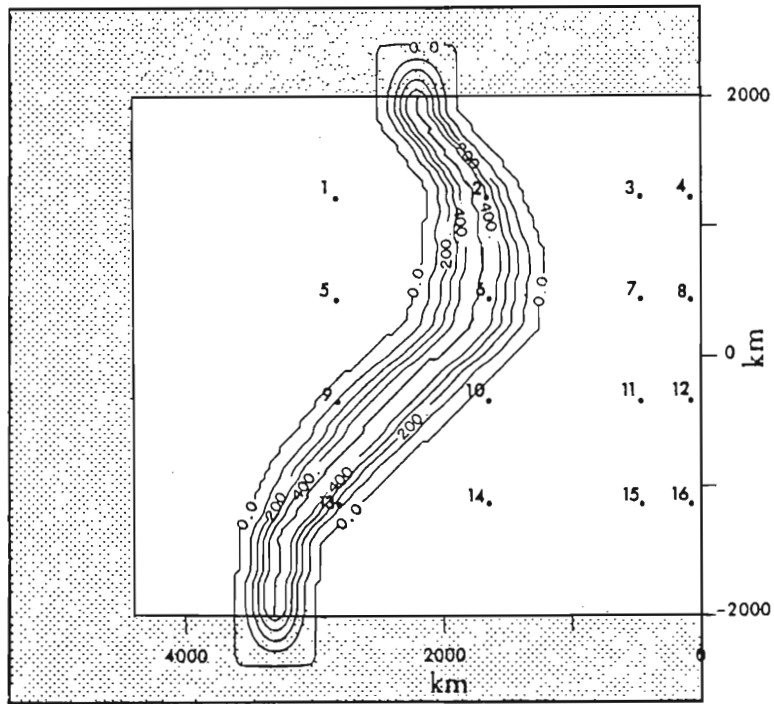
Figure 2. The model geometry. The depth contours (CI is 100m). The shaded region shows the extent of the damping layers. The unshaded region is the physical basin where the governing equations apply. The 16 outlined points indicate the locations where spectral analysis of the oceanic variables is performed.

the meridional damping layers where it goes progressively to zero to avoid discontinuities in the f/h contours. The zonal extension of the ridge is Gaussian-shaped, but at all latitudes the width of the Gaussian is conformed to the realistic width of the ridge. The depth contours are drawn in Fig. 2.

The eastern limit of the physical ocean basin is supposed to represent the eastern coast of the North Atlantic. It is approximated by a solid meridional boundary. The western damping layer begins at the western meridional limit, and the northern and southern damping layers, respectively, are at the zonal northern and southern limits (shaded regions in Fig. 2).

The role of a damping layer (also called sponge layer) is to prevent energy from being reflected or radiating away from the solid boundary it adjoins. The height of the ridge unrealistically goes to zero before it reaches the zonal boundaries of the model in order to avoid discontinuities in the f/h contours. The regions over which the ridge decreases are designed like sponge-layers in order to neutralize the dynamics that occur there. These sponge layers also prevent wave reflexion at the boundaries they protect and thus behave as a kind of open boundary.

The western boundary is an important source of vorticity, because it reflects incoming energy at shorter lengthscales and because it is the location of the western boundary current. For the present study the aim is to concentrate on the eastern boundary and

the mid-ocean ridge as potential sources of vorticity when the flow in these regions is forced by the wind. The western sponge layer is thus introduced to damp the dynamics of the western boundary and therefore, let the processes in the eastern ocean be free of perturbations coming from the western region.

A sponge layer is designed with an enhanced barotropic friction that rapidly damps the fluid motions independently of their lengthscales. As it appears in the governing equations (1) and (2), the process of dissipation of energy is baroclinic in character; bottom friction directly acts only on the lower layer dynamics (term $-\varepsilon_3 \nabla^2 \psi_3$ in (2)). To ensure a barotropic damping in the sponge layer, the upper layer equation (1) is modified by the addition to the right hand side of a friction term ($B_1 = -\varepsilon_1 \nabla^2 \psi_1$) similar to the bottom friction term of (2). To achieve an enhanced damping, the friction coefficients ε_1 and ε_3 have larger values inside the sponge layer than in the interior ocean (where $\varepsilon_1 = 0$ always). Also, to prevent energy reflexion at the limit between the interior ocean and the sponge, the friction coefficients gradually increase (like a Gaussian) over a transition region from their interior (minimum) value to a maximum sponge value and they are then constant to that maximum value over the rest of the damping layer. Table 1 shows the values and variations of ε_1 and ε_3 which are used in the present

Table 1

Variations of the friction coefficients ϵ_1 and ϵ_3 in the sponge layers. x is the distance to the western boundary of the model and y is the distance to the southern boundary. The lines of constant friction coefficient are plotted in Fig. 3.

Western Sponge Layer

$x_0 = 0$ km	$x_1 = 200$ km	$x_2 = 480$ km	$x_3 = 680$ km	$x_4 = 960$ km → Interior Ocean
$\epsilon_1(x)=\epsilon_{max}$	$\epsilon_1(x)=\epsilon_{max}\,\mathrm{Exp}\left(\frac{(x-x_1)}{r}\right)^2$	$\epsilon_1(x)=\epsilon_{mid}$	$\epsilon_1(x)=\epsilon_{mid}\,\mathrm{Exp}\left(\frac{(x-x_3)}{r}\right)^2$	$\epsilon_1(x) = 0$
$\epsilon_3(x) = \epsilon_{max}$	$\epsilon_3(x) = \epsilon_1(x)$	$\epsilon_3(x) = \epsilon_{mid}$	$\epsilon_3(x) = \epsilon_1(x)$	$\epsilon_3(x) = \epsilon_{min}$
$\epsilon_{max}=5\times10^{-6}\ \mathrm{sec}^{-1}$	$r=2(x_2-x_1)/\ln\left(\frac{\epsilon_{max}}{\epsilon_{mid}}\right)$	$\epsilon_{mid}=10^{-6}\ \mathrm{sec}^{-1}$	$r=2(x_4-x_3)/\ln\left(\frac{\epsilon_{mid}}{\epsilon_{min}}\right)$	$\epsilon_{min}=10^{-7}\ \mathrm{sec}^{-1}$

Northern Sponge Layer

$y_0 = 5360$ km	$y_1 = 4960$ km	$y_2 = 4680$ km → Interior Ocean
$\epsilon_1(y) = \epsilon_{mid}$	$\epsilon_1(y) = \epsilon_{mid}\,\mathrm{Exp}\left[\left((y-y_1)/r\right)^2\right]$	$\epsilon_1(y) = 0$
$\epsilon_3(y) = \epsilon_{mid}$	$\epsilon_3(y) = \epsilon_1(y)$	$\epsilon_3(y) = \epsilon_{min}$
$\epsilon_{mid} = 10^{-6}\ \mathrm{sec}^{-1}$	$r = 2(y_2-y_1)/\ln(\epsilon_{mid}/\epsilon_{min})$	$\epsilon_{min} = 10^{-7}\ \mathrm{sec}^{-1}$

Southern Sponge Layer

$y_0 = 0$ km $y_1 = 400$ km $y_2 = 680$ km → Interior Ocean
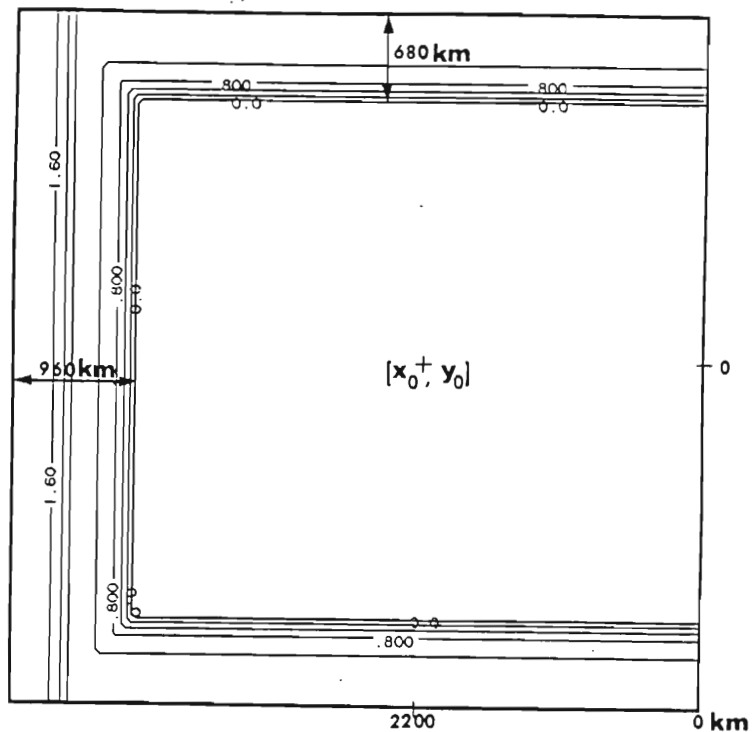
Figure 3. The damping layers. The lines of constant friction coefficient ε are displayed for the upper layer like $\log(\varepsilon_1 \times 10^7) = Cte$. A contour interval of 0.2 indicates a relative increase $\Delta\varepsilon/\varepsilon = 0.585$. The maximum value is $\varepsilon_1 = 5 \times 10^{-6}$ sec^{-1}. The minimum (interior) value is $\varepsilon_1 = 0$. The lower layer coefficient ε_3 varies identically except for an interior value $\varepsilon_3 = 10^{-7}$ sec^{-1}. The point $(x_0 = 2200km, y_0 = 0km)$ is the center point of the physical basin and represents the point whose lat-long position is 35°W, 37.5°N. The mathematical expression of $\varepsilon_{1,3}$ is shown in table 1.

study. They have been determined after a series of tests presented in Appendix B. Figure 3 displays the lines of constant friction coefficients. The northern and southern damping layers are each 680 km wide. The western damping layer has a 960 km width and is a two step sponge layer. The damping layers are limited by solid boundaries on the outside where the condition of no flow across the boundary is applied (slip boundary condition).

Consequently, the total basin over which the finite difference version of the governing equations are integrated (including the physical basin and the sponge layers) is a 5360 km square basin with a 40 km grid resolution, which yields a grid of 135 by 135 points in each layer. The ocean response is studied only in the physical ocean model; the presentation of the results is limited to this model.

C. The Forcing

The driving forcing is constructed after the results of an EOF analysis performed on one year of FGGE wind data (Barnier 1986). The analysis was done on the fluctuations, and therefore the resulting EOFs have a zero time average. The first four EOFs (spatial patterns and time series) have been retained to build the forcing function. The spatial patterns are represented on a 1.875° lat-long grid. They are projected on the model grid in the same length-conserving projection used to represent the ridge. The center point of the physical model is (x_o = 35°W, y_o = 37.5°N). A set of lat-long

coordinates is associated to each point of the grid. The value of any EOF spatial pattern at that point is then calculated by bilinear interpolation with the values of that EOF at the four lat-long closest points. As the model is designed, the projected EOF patterns fit on the physical domain. But the forcing is not defined on the sponge layers. It is more logical to set the forcing to zero in these layers since they are introduced to damp the solution. The act of setting the forcing to zero at the sponge layer introduces discontinuities which need to be smoothed. A consequence of this smoothing is the lowering of the forcing amplitude in the regions adjacent to the sponge layers.

The time series are unchanged and only interpolated (least-square parabolic interpolation) at the integration time step. The resulting forcing patterns are drawn in Fig. 4 and the time-series in Fig. 5. The total wind-forcing is obtained as follows. At every time step the total forcing is the sum of each EOF spatial pattern multiplied by the coefficient of its associated time-series that corresponds to the time-step;

$$\text{Curl } \tau(x,y,t) = \sum_n \text{EOF}_n(x,y) F_n(t), \quad n = 1, 4$$

where $\text{EOF}_n(x,y)$ is the spatial pattern of the nth EOF and $F_n(t)$ its associated time series.
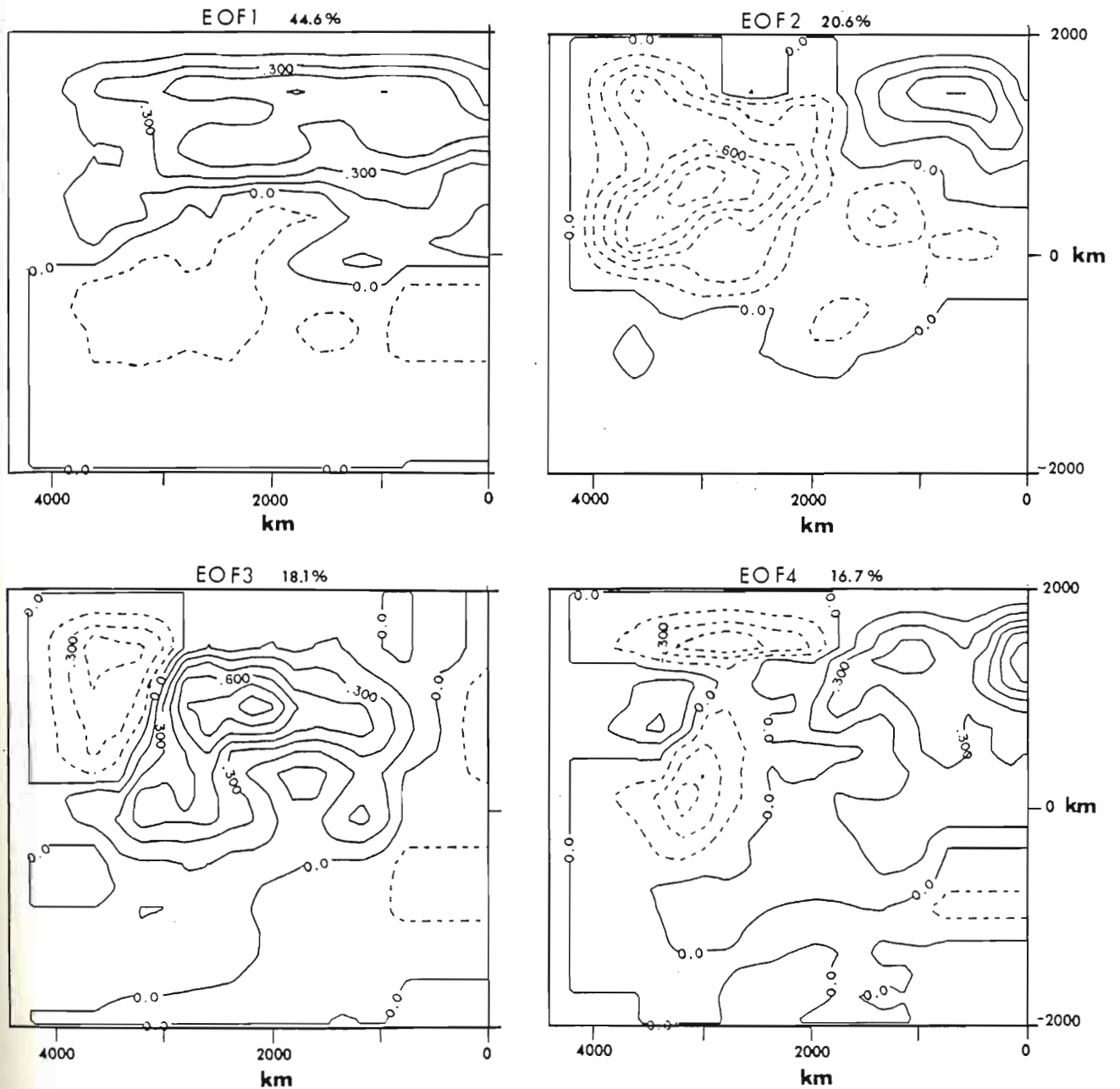
Figure 4. The spatial distribution of the forcing wind-stress
curl. Are displayed the projections on the model basin of the
spatial patterns of the four EOF's that compose the forcing. The
percentage of variance each EOF accounts for in the forcing is
indicated. The EOF's are normalized to unity. Contour interval is
0.15.
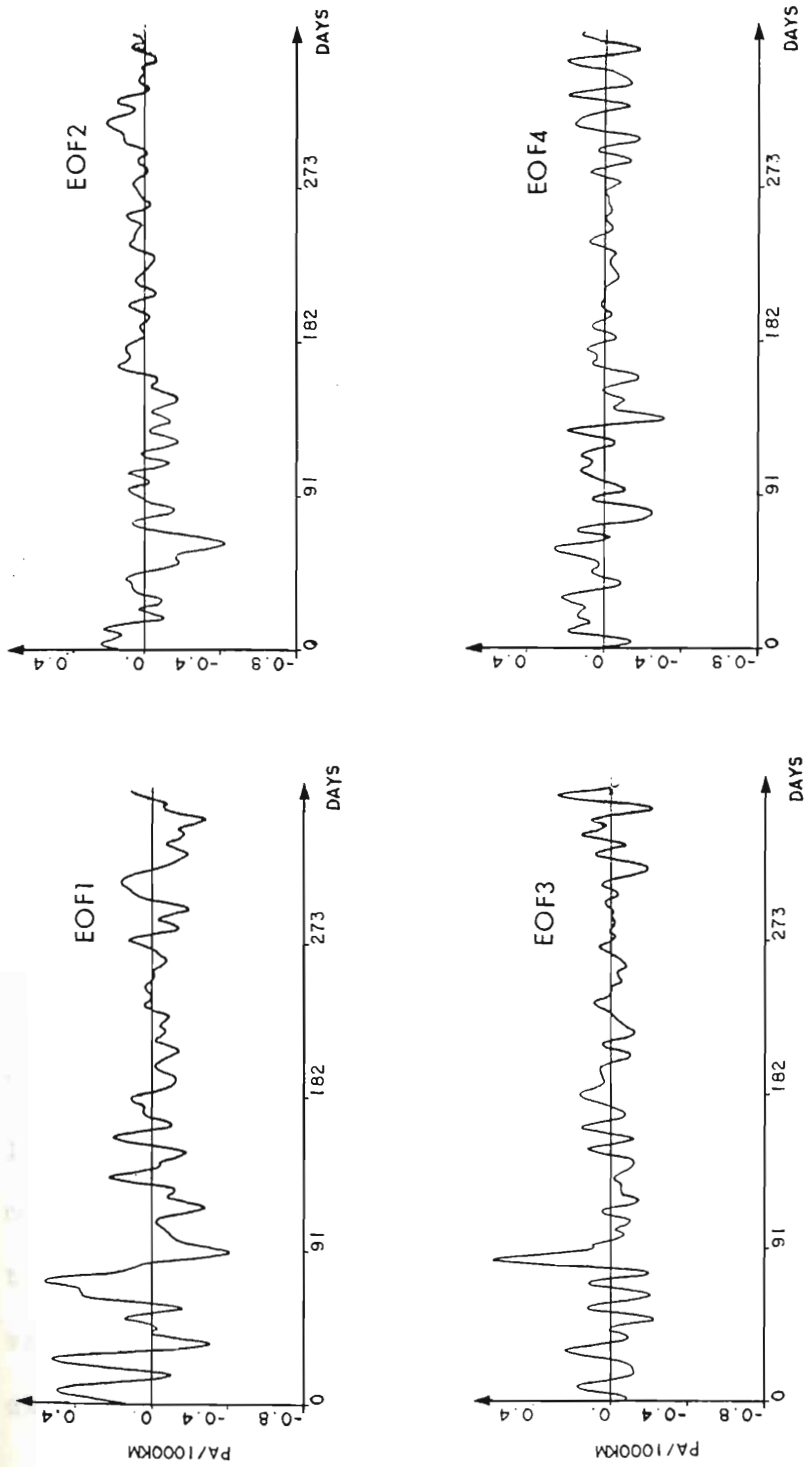
Figure 5. The time modulation of the EOF's that compose the forcing. Units are in Pa/1000km. Time-series start December 1st and are one year long.

The forcing covers only one year. It is presumed to repeat itself every year so a several years experiment can be run.

Barnier's (1986) study details the space and time variability of the EOFs that compose the forcing. The spatial pattern of the first EOF is described as a basin-sized meridional oscillation with a mode line across the middle and an amplitude larger to the north. Its time variability is best characterized by bi-monthly and monthly oscillations having a large amplitude in winter and a small amplitude in summer. Since this EOF accounts for 19.78% of the variability of the original data, it represents 45% of the present forcing and must be considered as the most important component. The higher order EOFs are also characterized by basin-sized oscillations and large amplitudes in winter. Each represents from 20 to 16% of the composed forcing. Therefore, the forcing should be considered as a purely fluctuating wind stress curl (zero mean) having basin-sized lengthscales. Fig. 6 displays 5 year period time-series of the repeated forcing in two different points of the physical basin. (The location of these points is shown in Fig. 2). The series start in December and show an alternation of winter high amplitude and summer low amplitude. This alternation results in an annual variability noticeable in the spectra of Fig. 6 which never exceeds 20% of the total variance (16% in series A and 10% in Series B). Most of the variability is contained in the seasonal variability (90 to 30 days). There is little variance for periods smaller than 15 days
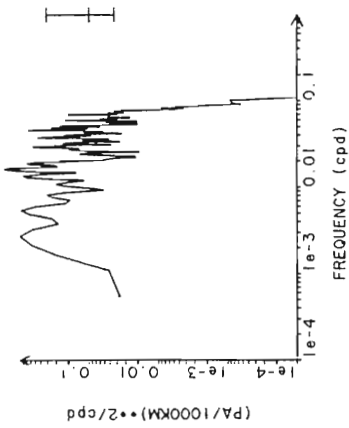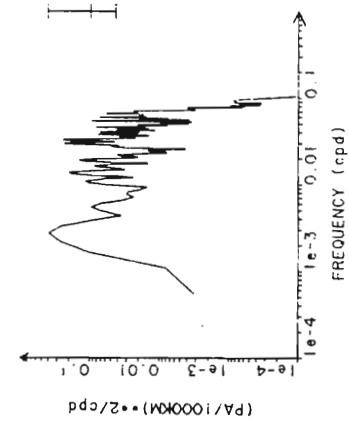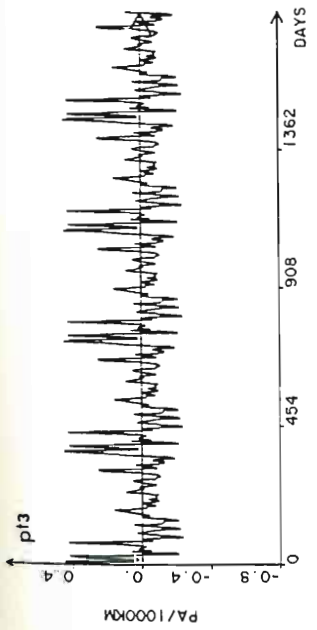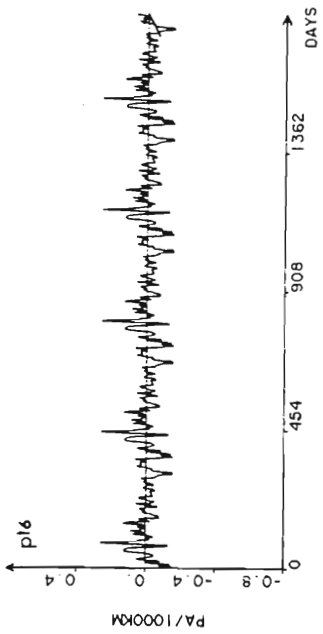
Figure 6. Five year long time-series of the wind-stress curl obtained by repetition of the one year long record of the forcing composed of the four EOF's. Series are located at point 3 (left) and point 6 (right) of Fig. 2. They start December 1st. Both series present an alternance of high winter and low summer amplitude. Spectra look rather white. Annual variability accounts for 10% of the total variance in series 3 and 16% in series 6. Seasonal variability is dominant at 60 days in series 3 (20% of total variance) and at 30 days in series 6 (18% of total variance). Variance sharply decreases at frequencies larger than 1/15 cpd and is zero at 1/7 cpd. Error bars are in the 95% confidence interval.
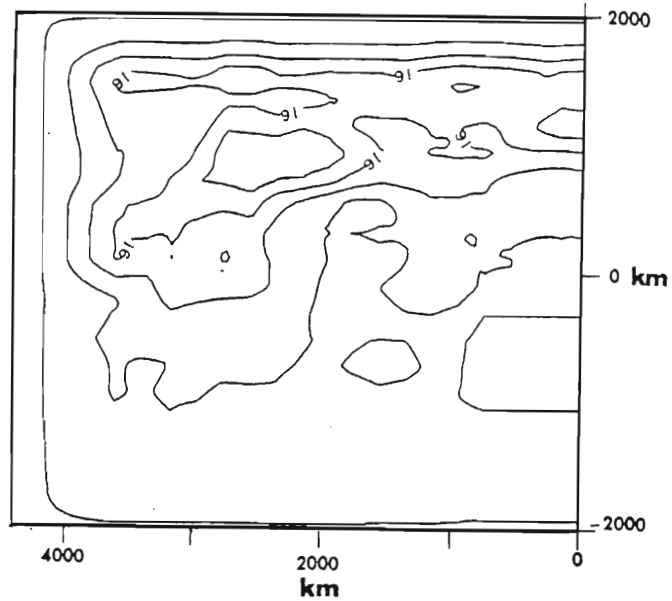
Figure 7. The rms wind-stress curl obtained with the four EOF's combined. The distribution is rather zonal with maxima in the northern part of the domain. Units are in Pa/1000km. Contour interval is 0.03. Labels are scaled by 1000.

due to filtering done for the purpose of the EOF analysis. There is
no signal at periods shorter than 7 days. The rms of the
reconstituted wind stress curl is shown in Fig. 7. The southern
basin appears to be weakly forced. Most of the wind energy is in the
northern basin with a maximum rms of the order of 0.12 Pa/1000 km at
central longitude.

D. The Numerical Experiments

Two experiments are run: a "flat-bottom" experiment where the
topography is set to zero and a "ridge experiment" with the ridge-
like topography previously described. In both cases the model is
integrated in exactly the same conditions and for the same period of
time in order to produce directly comparable data sets. Therefore,
except for the topography, all the features which are characteristic
of the model (sponge layers, forcing, etc.) are identical in both
cases and are just as they have been defined previously. The values
of the numerical and physical parameters are summarized in Table 2.

The numerical integration of the model is performed as
follows. The initial state is the state of rest. The model is
integrated over 15 years. The first 10 years are necessary for the
model to reach a state of statistical equilibrium. After this time
the total energy contained in the basin is stabilized, and the
influence of the initial conditions has vanished. The last 5 years

Table 2

Parameters in both the flat bottom and the ridge experiments

Model grid Δx = 40 km	Upper layer depth H_1 = 1000 m
Time step Δt = 8 hours	Lower layer depth H_3 = 4000 m
Biharmonic friction A = $5 \times 10^{10} m^4 sec^{-1}$	Coriolis parameter f_o = $8.85 \times 10^{-5} sec^{-1}$
Bottom friction ε_3 = 10^{-7} sec^{-1}	Beta parameter β = $1.8 \times 10^{-11} m^{-1} sec^{-1}$
Ridge mean slope* $\dfrac{\Delta h_B}{h_B}$ = 6.25×10^{-4}	Reduced gravity g' = $2 \times 10^{-2} m\ sec^{-2}$

*For the ridge experiment only.

of integration produce the data set which describes the model

response. A 5 year period is necessary to obtain significant mean

and eddy statistics. (Five years is the time needed by the

baroclinic Rossby waves generated at the eastern boundary to cross

the basin and vanish into the western sponge layer. It is also the

minimum period over which the ocean variables need to be averaged in

order to obtain convergent mean values). The time-dependent response

is analyzed using instantaneous plots of the oceanic fields, phase

diagrams, and by means of spectral and cross-spectral analysis

performed on time-series of the oceanic variables at the 16 points

outlined in Fig. 2. The statistical characteristics of the model

response are investigated using the pointwise energy diagnostics

developed in Appendix A.

III.   THE FLAT BOTTOM EXPERIMENT

A.   The Gross Features of the Time-dependent Response

The most striking features of the model time-dependent response
can be drawn from maps that represent the instantaneous
streamfunction and vorticity field in each layer.   The
streamfunctions displayed in Fig. 8 show that the response is
barotropic at large lengthscales, whereas baroclinic wavelike
patterns of smaller amplitude appear at lengthscales of about 500
km.   In each layer the streamfunction repeats itself (at more than
95%) every year.   This indicates that the response of the model is
very linear (the Rossby number is $0(10^{-3})$) and is mainly constituted
of planetary waves resonantly forced by the wind forcing and of long
barotropic and annual-period baroclinic Rossby waves.   Maps of the
vorticity field (Fig. 9) show that the eastern boundary is the most
important source of vorticity.   The maximum vorticity occurs in the
upper layer at the eastern boundary when the forcing reaches its high
winter amplitude and sharply falls to its low summer amplitude in
early spring.   This suggests that the eastern boundary is the most
significant source of baroclinic Rossby waves.   In addition, the
first EOF is mainly responsible for their generation, since it is the
forcing pattern that is the best characterized by a change in

33
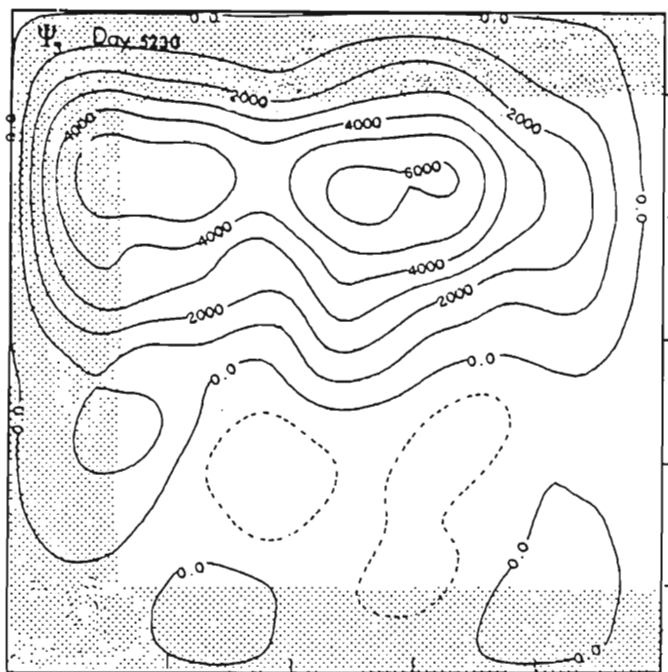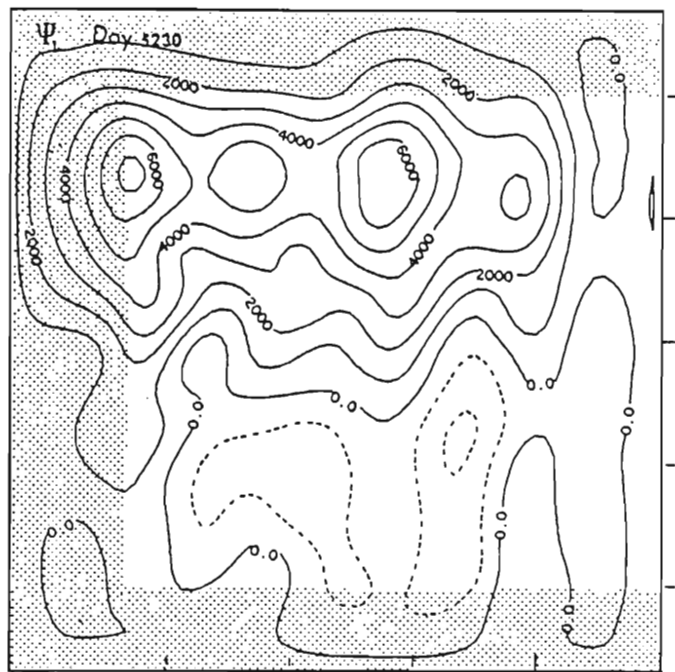
Figure 8. Flat bottom case. Instantaneous maps of the upper layer (top) and lower layer (bottom) streamfunctions. The picture is taken on March 30 in the 15th year of simulation (Day 5230). The sponge regions are shaded. The patterns are barotropic at large scales whereas baroclinic features appear at lengthscales of about 500km. Contour interval is 1000m^{2}sec^{-1}.
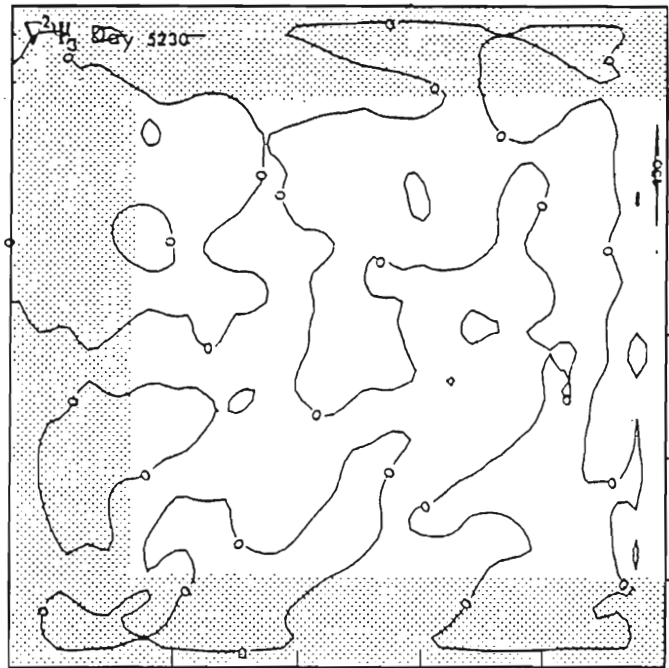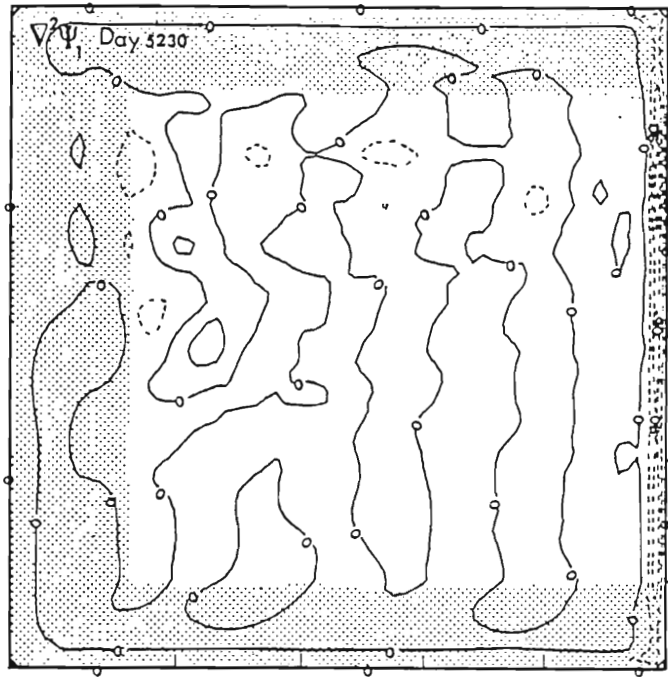
Figure 9.   Flat bottom case.   Instantaneous maps of the upper (top)
and lower (bottom) vorticity field.   The picture is taken on March 30
in year 15 (Day 5230).   The sponge regions are shaded.   The eastern
boundary appears as the main source of vorticity for the upper
layer.   Contour interval is 0.45×10^{-7} sec^{-1}.

amplitude in the spring.

Figure 10 displays frequency spectra for the upper and lower layer velocities at 4 different locations. The general spectral level is low compared to observations or to recent results from a stochastic model; e.g., Lippert and Kase (1985). In addition to the simplicity of the model, several reasons are given for the small amplitude of the spectra. A relatively high value of the friction coefficient is used in the simulation ($\varepsilon_3 = 10^{-7} \sec^{-1}$ yields a e-folding damping time of 115 days). The relatively important thickness of the upper layer ($H_1 = 1000$ m) implies that the spectra are to be considered as average spectra for the first 1000 m depth. Also, the forcing function only represents the deterministic part of the seasonal fluctuations of the real wind stress curl accounting for only 44.3% of the total variance of the FGGE wind data. Nevertheless, the amplitude of the model response is comparable with similar studies, e.g., those of Willebrand et al. (1980) and Krauss and Wubber (1982). Velocities range from 1-2 cm $\sec^{-1}$ in the interior ocean.

The spectra are barotropic at frequencies larger than 0.015 cpd (66 days). In that range of frequency the response is expected to be dominated by forced barotropic planetary waves and by long barotropic Rossby waves generated at the eastern boundary. The long waves have short period ($\omega > 0.05$ cpd) and would be basin modes if there were no
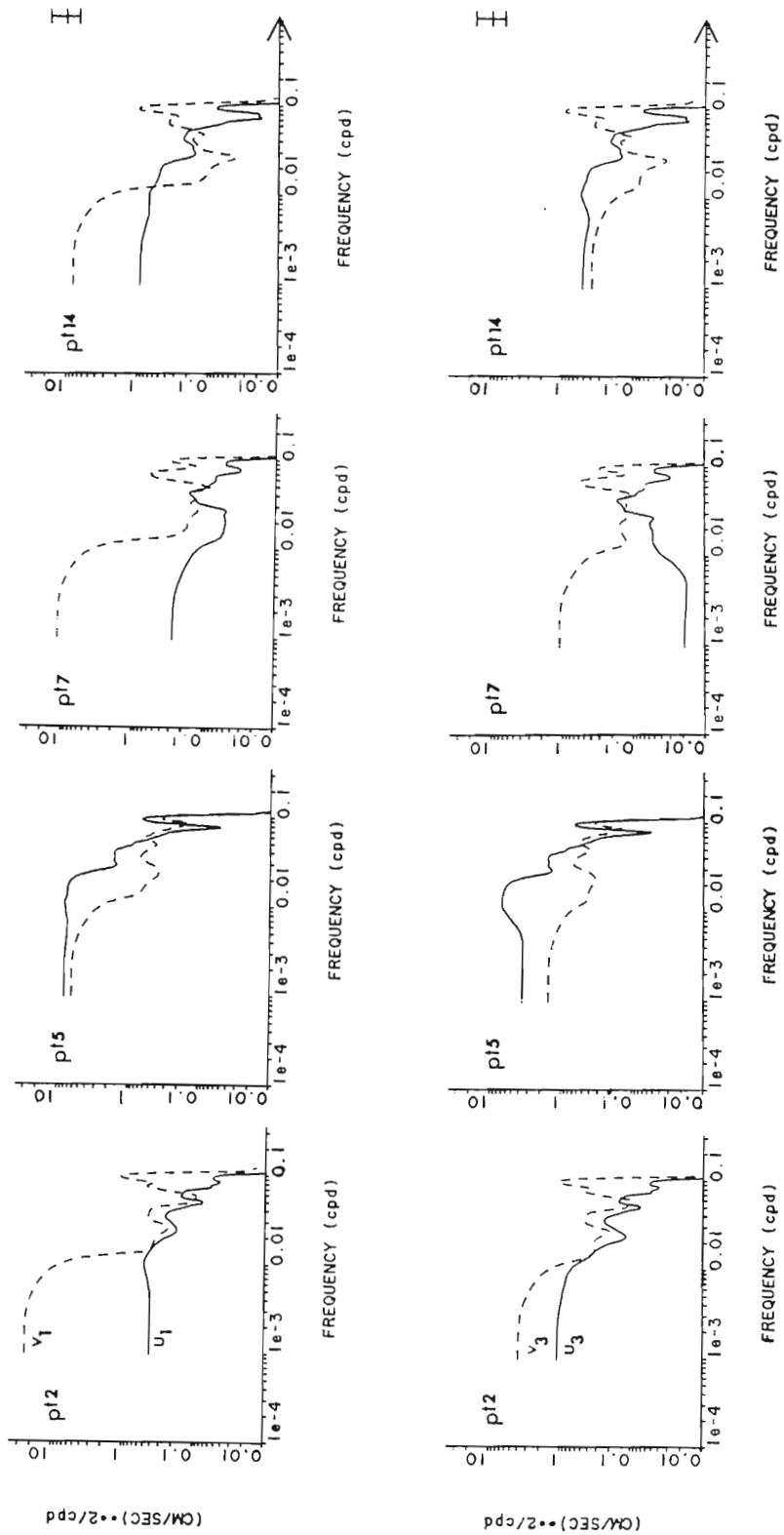
Figure 10. Flat bottom case. Frequency spectra for the upper layer
velocities (top) and the lower layer velocities (bottom) at points 2,
5, 7, 14 of Fig. 2. Upper and lower layer spectra are identical at
frequencies larger than 0.02 cpd indicating a barotropic time-
dependent response. At lower frequencies spectra are characteristic
of a barotropic Sverdrup's balance. No obvious baroclinic response
is apparent.

western sponge layer. At lower frequencies ($\omega <$ 0.015 cpd) differences appear in the spectra depending on which velocity component or which layer they represent. The zonal spectra often follow the meridional spectra but with a lower level. This is ascribed to the Sverdrup balance since the meridional gradients of the forcing patterns create similar gradients in the barotropic Sverdrup transport. This induces, by continuity, a zonal geostrophic transport that can be important. Indeed, in the regions of strong meridional gradients in the forcing (point 5), the zonal spectra reach and even pass the level of the meridional spectra. In these regions of strong gradients in the forcing, one expects short-wave length Rossby waves to be generated. These waves certainly account for the high energy level found in spectra 5, 14 at intermediate frequency. The upper layer meridional spectra always exceed the lower layer spectra. This is ascribed to the baroclinic part of the Sverdrup balance and to the annual-period baroclinic Rossby waves. (The peak at the annual frequency in the spectra which is associated to those waves is spread over a larger frequency band because of the smoothing performed to increase the statistical stability). No other baroclinic features appear in these energy spectra. Strong isolated baroclinic features, like eddies, are not likely to be generated by large scale wind fluctuations in the abscence of strong mean currents. In a two layer model the minimum velocity shear necessary to an inviscid flow to be baroclinically unstable is

$U_c = U_1 - U_3 = O(\beta g'H_1/f_0^2)$ (Pedlosky 1979). For viscous flow that limit is even larger. In the present model $U_c = 5$ cmsec^{-1}, and since the velocities do not exceed 2 cmsec^{-1} in the open ocean, baroclinic instability is not likely to develop.

The mean fields (time-averaged over the 5 years of statistical equilibrium) are not presented since they do not show many interesting features. The non-linearities are weak, and the currents are weakly rectifying. The maximum mean transport in the upper and lower layer does not exceed 0.12 Sv. The kinetic energies associated to the mean fields are insignificant.

B. The Barotropic Response

The time-dependent barotropic response assembles many of the features of the study of Willebrand et al. (1980). The velocities in the interior ocean have maximum values of about 2 cm sec^{-1}. They increase simultaneously with the amplitude of the forcing fluctuations. They are maximum in winter, decrease sharply in the spring, and gradually increase during the fall. At low frequencies ($\omega < 0.02$ cpd) the response is primarily the barotropic Sverdrup balance. At high frequencies (0.02 cpd $< \omega$) forced dispersive barotropic Rossby-waves dominate the ocean response. These waves are locally generated by the wind forcing and propagate the input energy away from the source regions, mainly to the west and the east, but with a noticeable southward component.

The spectra displayed in Fig. 10 show maxima in the kinetic energy at period near 10 and 15 days. The same peaks appear in Willebrand et al.'s study. They are ascribed to resonant basin modes. But in the present study the sponge layers prevent such modes from existing since no wave reflexion is possible at the western boundary. Since the forcing has little variance at frequencies larger than 1/15 cpd, the 10-day period signal has to be generated by the low wavenumbers of the forcing. The 10 day waves are noticeable in the y-t plot of Fig. 13. No meridional phase velocity appears in the signal, which suggests that the waves may have a meridional modelike structure. That particular organization is attributed to the fact that all the EOF's which compose the forcing have a zero value over the northern and southern sponge layers and are likely to force first meridional modelike waves. However they also have a larger amplitude in the northern basin and are likely to generate the second meridional modelike waves. The 10-day period signal is investigated by cross-spectral analysis of the barotropic streamfunction (Fig. 11). The zonal phase spectrum identifies westward phase propagation at 4.9 m sec^{-1}. The dispersion relation for barotropic Rossby waves having a meridional modal structure and the definition of the phase velocity

$$\omega_m = -\beta k/(k^2 + n^2\pi^2/Ly^2) \quad , \qquad C_x = \omega/k \quad , \qquad (4)$$

allow the calculation of the other characteristics of the waves. The zonal wavenumber is $k = 2\pi/4900\text{km}$. A second-mode n=2 is suggested
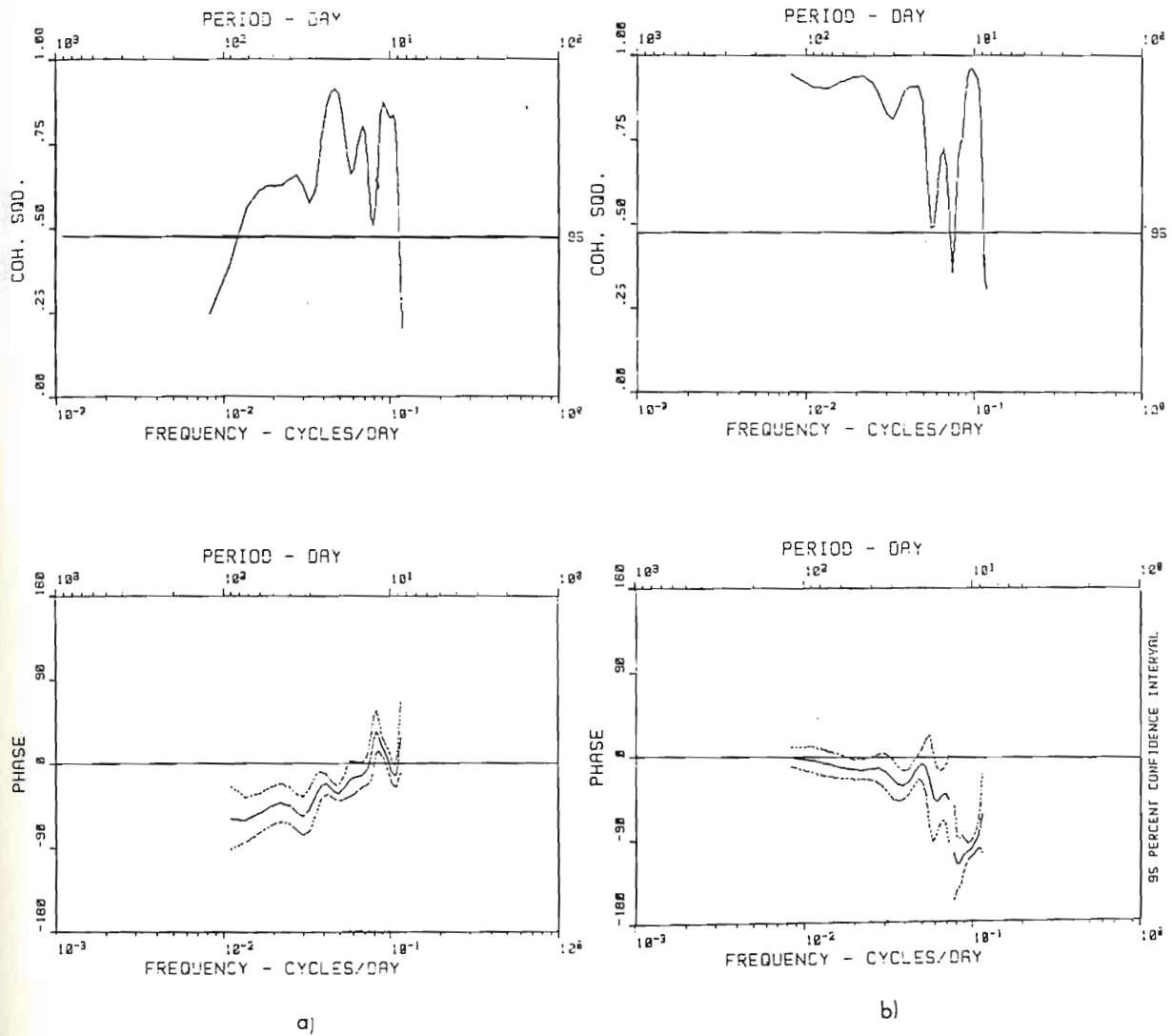
Figure 11. Flat bottom case. Cross-spectra of the barotropic
streamfunction. a) Meridional cross-spectra between points 2 and
6. b) Zonal cross-spectra between points 2 and 3. Negative phase
indicates that the signal propagates northward in (a) and westward in
(b).

and yields to $L_y=4900$km, a consistent value that fits between the size of the basin (5360km) and the distance separating the zonal sponge layers (4000km). The group velocity is eastward at 0.52 cm sec^{-1}. The first mode waves (n=1) may also exist, but the spatial pattern of the first EOF (45% of the forcing), which shows an opposition in phase between the northern and southern basin, suggests that the second-mode waves should be dominant.

Analysis of the 15-day period signal is more complex because the forcing has some variance in this frequency range and therefore locally forced waves can exist. Also, the range of wavenumber in the forcing that can generate a 15 day period signal is larger than for the 10 day period. Thus, more waves are generated, and the resulting signal does not give much information when cross-spectral analysis is performed. The plot of Fig. 13 does suggest that an important part of the barotropic response presents a meridional structure similar to a second mode forced by the high amplitude of the forcing in the northern basin and by the zero value of the forcing over the sponge layer. Therefore, the 15 day signal is certain to contain Rossby waves having a second mode meridional structure. Assuming that the second mode has a wavenumber $l = n\pi/Ly$ with n=2 and Ly=4900 km as in the 10 day signal, the dispersion relation (4) yields the following characteristics for the 15 day waves. The longest waves have a zonal wavenumber $k = 2\pi/12220$km. They propagate energy westward at 6.8 m sec^{-1}. The phase speed is westward at 9.6 m sec^{-1}. These waves are

more likely to be generated at the eastern boundary by the 15-day period oscillations of the forcing. The shorter waves have a zonal wavenumber $k = 2\pi/1960$ km. The phase speed is 1.5 m sec^{-1}, and the group velocity is eastward at 1.1 m sec^{-1}. These waves may be generated anywhere in the basin but certainly in the vicinity of the western sponge layer which is a node region for the forcing. Also, the 3rd and 4th EOFs which both present significant variability at the 15 day period can generate these waves in the middle of the ocean. The eastward group velocities observed in Fig. 12 are of the order of 1 m sec^{-1} and may be attributed to those waves.

As shown by the tilt of the lines of constant streamfunction in the time-longitude plots of Fig. 12, the barotropic response features important westward phase propagation everywhere. Phase velocities range from 1 to 6 m sec^{-1}. This signal is associated with barotropic Rossby waves and accounts for most of the variability of the ocean response. It is contained in the high frequency band ($\omega > 0.01$ cpd). Futhermore no coherency is found at these frequencies between the oceanic variables and the wind forcing, which confirms that this signal may be attributed to propagative waves. These waves include the high-frequency waves (10 and 15 day period) and Rossby waves of lower frequency locally generated by the wind forcing. The partition of the barotropic eddy kinetic energy displayed in Fig. 14 differs from the rms distribution of the wind forcing (Fig. 7) and from the distribution of the transfer-rate of

BAROTROPIC HEIGHT (METERS)
ZONAL SECTION AT Y= -640KM
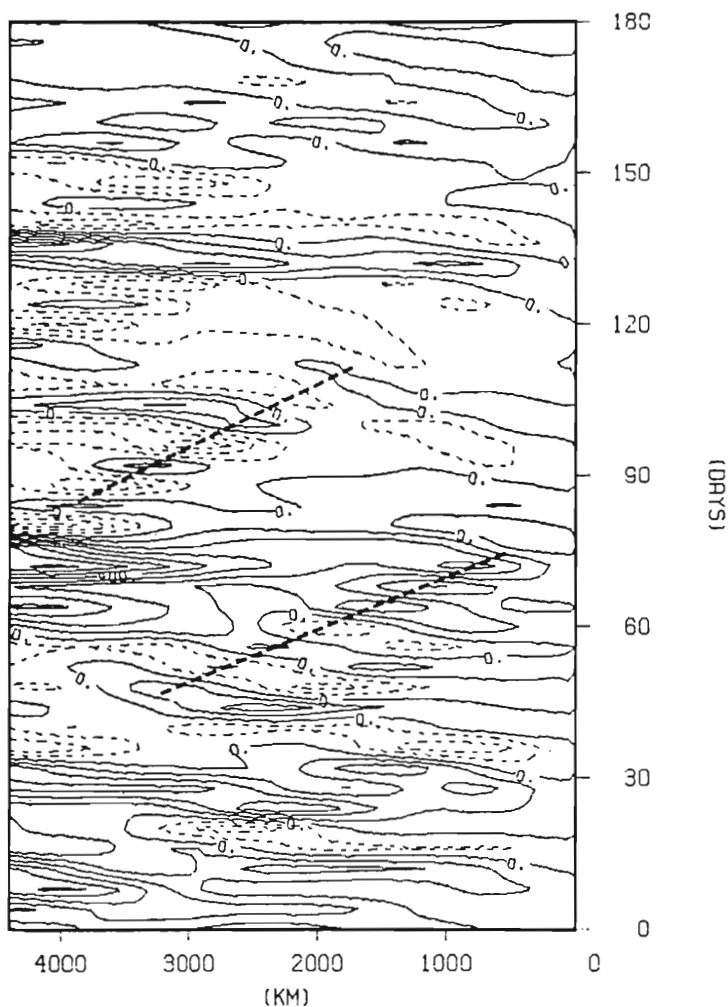
Figure 12. Flat bottom case. x-t plot of the equivalent barotropic height. The tilt of the contour lines indicates westward phase propagation with velocities ranging from 1. to 10. $m\,sec^{-1}$. The heavy dashed lines show eastward group velocities of about 1. $m\,sec^{-1}$. Time extents from December 1st to May 30th in the 15th year of the experiment. Units are in meters. CI is 0.01.

BARØTRØPIC HEIGHT (METERS)
MERIDIØNAL SECTIØN AT X=1640KM
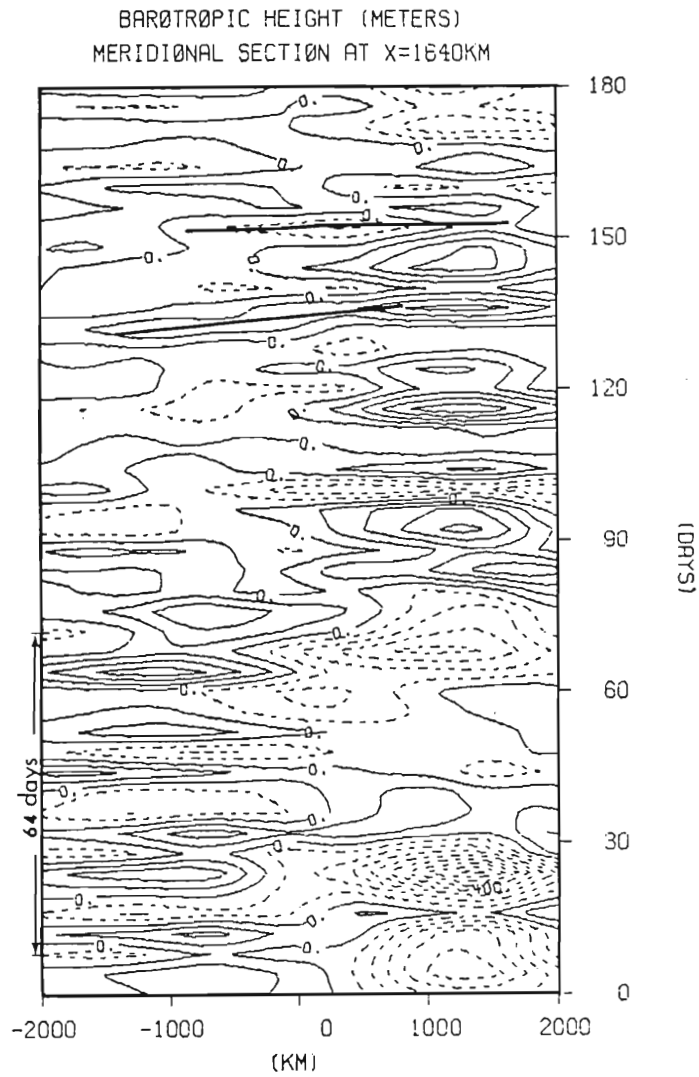
Figure 13. Flat bottom case. y-t plot of the equivalent barotropic
height. Northward phase propagation is outlined at mid-
latitude (y≈0km) by the heavy dashed lines which show phase speed of
$10 \, m \, sec^{-1}$ and $4.6 \, m \, sec^{-1}$. The 10 day period waves are noticeable
at low latitudes (y<-1000km) where the local forcing is weak. Time
and CI are like in Fig. 12.

the wind energy into the ocean which is shown in Fig. 15. The differences are credited to the planetary waves which propagate energy away from the regions of maximum input. The regions of Fig. 14 where the barotropic kinetic energy is maximum are identified as the most energetic source regions (where short waves are generated). Most are located in the northwestern basin. The isoplots show that waves radiate energy away from the sources mainly to the west and, at a lower speed, to the east (eastward group velocities are noticeable on the x-t plots of Fig. 12). In the northernmost part of the basin the propagation of energy seems purely zonal. But in the center and southern parts energy seems to radiate southward also. Meridional cross-spectral analysis of the barotropic streamfunction exhibits negative phases if the first time-series is the northernmost, indicating northward propagation of signals. Also, time-latitude plots of the barotropic streamfunction (Fig. 13) feature northward phase velocities at latitudes y < 1000 km, which suppose that at these latitudes waves propagating energy southward are more numerous. Similar to Willebrand et al. (1980) who noticed this in their study, the excess of waves with southward group velocity is a consequence of the spatial distribution of the wind forcing, which has its largest amplitude in the northern part of the basin.

At low frequencies (ω < 0.02 cpd) the ocean response is mainly the Sverdrup balance. Spectral and cross-spectral analysis of time-
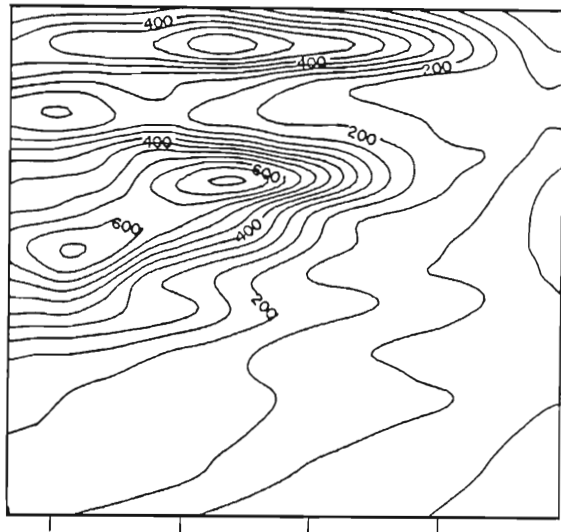
BARØTRØPIC EDDY KINETIC ENERGY

Figure 14. Flat bottom case. Spatial distribution of the vertically integrated, mean barotropic eddy kinetic energy. Maxima indicate sources of short-wavelength Rossby waves. The patterns show energy radiating westward as well as eastward. Units are in $m(m^2 sec^{-2})$. CI is 5×10^{-3}. Labels are scaled by 10^4.

TRANSFER   WIND ⟶ EKE1

TRANSFER   EKE1 ⟶ EKE3

Figure 15.   Flat bottom case.   Vertically integrated, mean eddy
kinetic energy transfert rates.   (a)   From the wind into the upper
layer and (b) from the upper layer to the lower layer.   Their
definitions are in Appendix A, table 2.   Units are in $m(m^2 sec^{-2})/sec$.   CI is 4×10^{-8}.   Labels are scaled by 10^{10}.

series of the barotropic meridional transport $V = H_1 v_1 + H_3 v_3$ and the theoretical Sverdrup transport β^{-1} curl(τ/ρ) have been performed at the 16 locations outlined in Fig. 1. In the low frequency band the two quantities have similar spectra, are strongly correlated, and are in phase, which confirms that the barotropic Sverdrup balance

$$\beta(H_1 v_1 + H_3 v_3) = \text{curl}(\tau/\rho)$$

dominates the low frequency response. It must be noted that, at some locations, the presence of short Rossby waves destroys the coherency. Also, at some locations, high coherency may be found between those two variables in the Rossby-wave range due to local wave-generation by direct wind forcing.

As mentioned before, the currents are weakly rectifying, and the mean fields do not present many interesting features. The mean barotropic transport is less than 0.12 Sv. The mean barotropic kinetic energy is 3 orders of magnitude smaller than the eddy kinetic energy and is not significant.

C.   The Baroclinic Response

The baroclinic response consists of coastally forced and free annual period baroclinic Rossby waves. The fact that the annual cycle strongly dominates the response is a direct consequence of the forcing space and time scales. Lippert and Kase (1985) showed that,

in the open ocean, the spectrum of baroclinic waves forced by a frequency-white forcing is essentially dependent on the cut-off wavenumbers of the forcing spectrum. For wavenumbers ranging from $2\pi/5000$km to $2\pi/500$km the ocean response is centered around the annual frequency. In the present study a baroclinic cut-off frequency is defined as the highest frequency possibly excited by the forcing and is evaluated as

$$\omega_c = -\beta k_{max}/(k_{max}^2 + l_{min}^2 + R_d^2)$$

where k_{max} and l_{min} are, respectively, the largest zonal and smallest meridional wavenumbers of the forcing. R_d is the internal radius of deformation. The EOF forcing has $k_{max} \approx 2\pi/500$km and $l_{min} \approx 2\pi/4000$km which results in a cut-off frequency $\omega_c \approx 1.75$ cpy. The forcing spectrum is not white at frequencies $\omega < \omega_c$ but has a peak at the annual cycle (Fig. 6). Therefore the annual period baroclinic Rossby waves are most likely to be excited in the open ocean.

What happens at the eastern boundary is somewhat different. Free waves are generated so the baroclinic streamfunction matches the boundary conditions. Therefore the directly forced baroclinic response is likely to determine which waves will be generated. The forcing is a combinatin of four EOFs with spatial patterns that can be described as basin-sized oscillations (Fig. 4). Their time variability at low frequencies ($\omega < \omega_c$) is best characterized by an

amplitude high in winter and low in summer. Therefore the directly
forced baroclinic response is expected to have a large zonal
lengthscale (or zero zonal wavenumber) and be dominated by the annual
cycle. As a consequence, the waves generated at the eastern boundary
are likely to have an annual period.

In the present study the time dependent baroclinic response is
investigated from the sequence of Fig. 16, which shows the
instantaneous baroclinic height every 120 days during the 14th and
15th years of simulation. Annual period baroclinic Rossby waves
obviously dominate the model response. Their amplitude is about 6 to
8 meters with maxima up to 12 meters in the northeastern quarter
basin. In the southern basin the waves have smaller amplitude. They
are generated at the eastern boundary and apparently propagate
westward.

The waves issued from the northern part of the eastern boundary
have the largest amplitude and appear distorted by the locally forced
response. The phase speed is mainly westward. No significant
meridional phase propagation is noticeable. In the western-central
part of the basin the contour lines are distorted, indicating a
northwestward phase propagation. Free waves with significant
northward phase speed are certainly generated there and superpose to
the wave field issuing from the eastern boundary.

Maps of the baroclinic eddy kinetic energy and eddy potential
energy (Fig. 17) identify more precisely three sources of waves: the
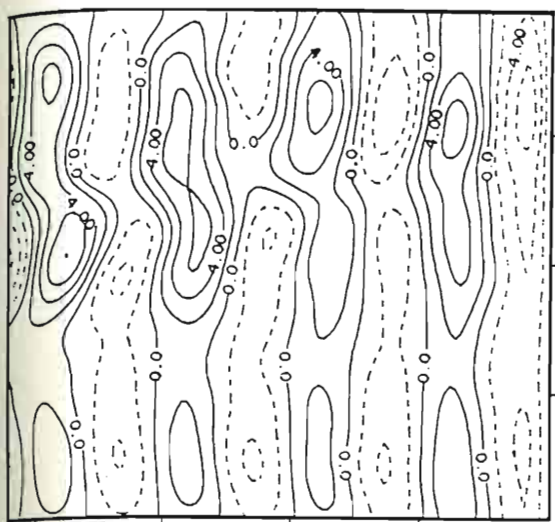
TIME= 4571
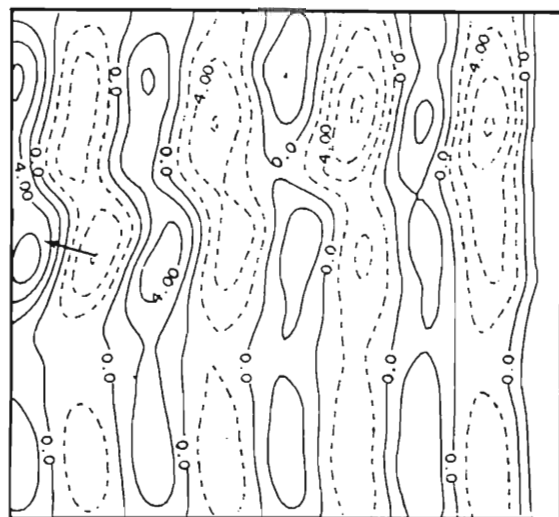
TIME= 4691
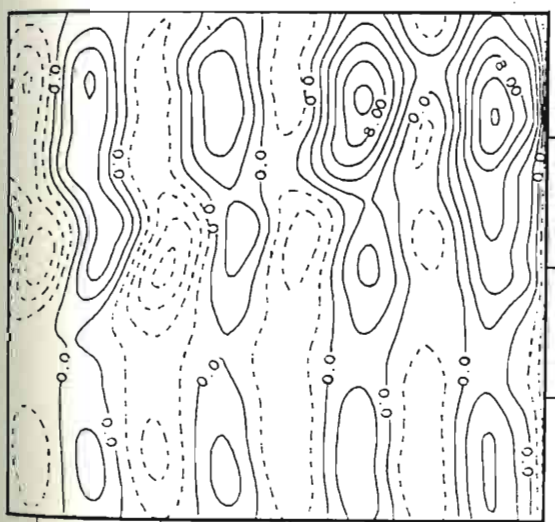
TIME= 4821
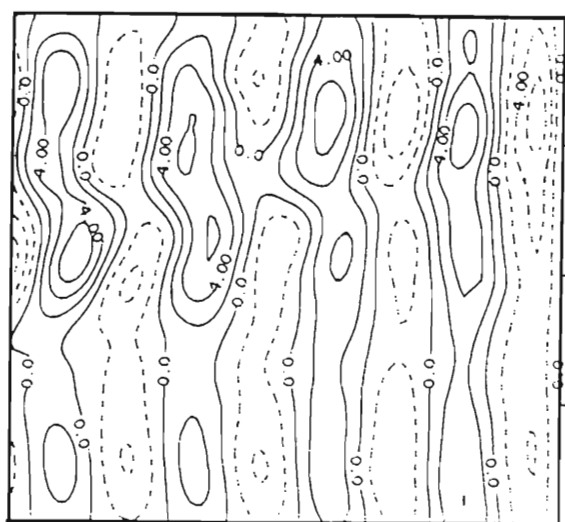
TIME= 4941

Figure 16. Flat bottom case. Instantaneous maps of the interface height (positive upward) at four different times separated by 120 days. The first plot is day 4571 (June 9 in year 13). The similarity of the first and last plots illustrates the annual periodicity of the wave field. The arrow in the second plot indicates a northwestward phase propagation 17° to the north of the zonal direction. Notice the large amplitude of the signal in the northeastern basin in February (third plot). Units are in meters. CI is 2.

northern and the southernmost parts of the eastern boundary and the center of the basin. The distribution of the potential energy is characteristic of waves coastally forced by a zero-wavenumber forcing. Because the amplitude and phase of the free waves are basically determined by the local response at the coast, the combination of the free waves with the zero-wavenumber forced response yields a total signal having an amplitude which presents a spatial modulation in the open ocean. It is noticeable on the x-t plots of Fig. 18 and is responsible for the series of maxima in the distribution of the potential energy, whereas the kinetic energy is distributed rather homogeneously. The simplest model describing this type of coastally-forced waves is the model of White's (1977). White's solution of forced baroclinic waves is applicable for the long-wave approximation in a two-layer ocean. The coastally-forced waves are the combination of the local response to a zero-wavenumber forcing with free westward propagating Rossby waves. The free waves are necessary to keep the baroclinic streamfunction constant at the boundary. The resulting waves show an off-coast sine modulation in amplitude with a wavelength twice that of the free waves. In consequence, the potential energy shows a sine-square zonal dependence, and minima and maxima alternate off coast with the wavelength of the free waves. White's solution appears as a special case in the study of Lippert and Kase (1985). They emphasize that characteristic distribution of the potential energy can be used to
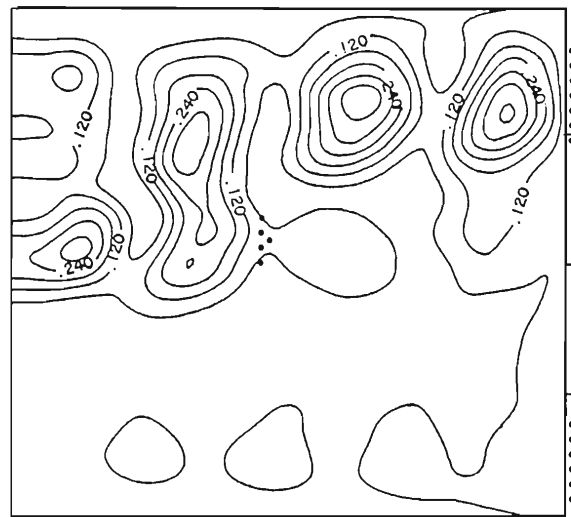
EDDY POTENTIAL ENERGY
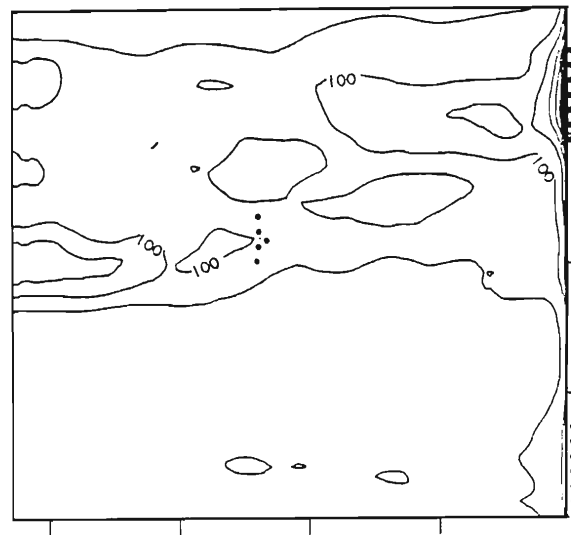
BAROCLINIC EDDY KINETIC ENERGY

Figure 17. Flat bottom case. Spatial distribution of the vertically integrated, mean eddy potential energy and mean baroclinic eddy kinetic energy. The heavy dots indicate sources of annual period baroclinic Rossby waves. The succession of maxima off the coast in the eddy potential energy is characteristic of coastally generated waves. Units are in $m(m^2 sec^{-2})$. CI is 0.06 for the potential energy and 5×10^{-3} for the kinetic energy where labels are scaled by 10^4.

distinguish between free and coastally-forced waves. Although
White's solution does not exactly apply for different boundary
conditions, the alternating minima and maxima in the potential energy
still characterize a combination of free waves with large-scale
directly forced oscillations.

In the present study we assume from the distribution of the eddy
energy that the waves radiating off the eastern boundary are
coastally-forced, in the sense that they are necessary for the ocean
response to the large scale (zero wavenumber) forcing to match the
boundary condition at the coast. The first EOF with its large-scale
zonal structure is certainly most responsible for their generation.
x-t plots of the baroclinic height, like the one presented in Fig.
18, suggest that the free waves have a zonal phase speed of the order
of $C_x=3.4$ cm sec^{-1}. The theoretical phase speed of the purely
westward propagating waves, calculated from the dispersion relation
for the first mode baroclinic waves (Pedlosky, 1979)

$$\omega = -\beta k/(k^2 + l^2 + R_d^{-2}) \qquad \text{with } l = 0,$$

is $C_x=\omega/k=3.44$ cmsec^{-1}, which is matched by observed signal within
2%. Therefore the free waves are assimilated to the theoretical
waves, and the dispersion relation is used to determine the other
characteristics of the waves. Their wavelength is 1060 km, and their
group velocity is westward at 3 cm sec^{-1}. Fig. 19 displays a y-t

plot of the baroclinic height. The section is done in the western basin. In the southernmost part of the basin, (y $\leq$ -1000 km) where the forcing has a small amplitude, it is not unrealistic to point out a southward phase speed of the order of 6 cm sec^{-1}, as shown by the heavy dashed line drawn in Fig. 19. This southward propagation of the signal is attributed to the sponge layers which slows down the wave in its southern part and produces the tilting of the wave patterns which is observed in Fig. 16. The northern waves should also feel the sponge effect, but it is more difficult to observe since the local response has a large amplitude there. In any case the change in group velocity is insignificant.

The waves generated in the middle basin radiate energy to the west with a small southward component. Indeed, the observed baroclinic height is a combination of the waves issued from the eastern boundary with the waves generated locally. It shows a non-zero northward phase velocity as indicated by the tilting of the contour lines in Fig. 16. The plots of Fig. 18 and Fig. 19 allow an evaluation of the phase speed of that signal. Its westward phase speed, calculated from the heavy dashed line on Fig. 18, is C_x = 3.25 cm sec^{-1} to the west. The heavy line of Fig. 19 yields the northward phase velocity C_y = 4 cm sec^{-1}. Under the hypothesis that this signal is the result of a linear combination of sine-like waves having the characteristics of the waves coming from the eastern boundary with locally generated sine-like Rossby waves, it is

BARØCLINIC HEIGHT (METERS)
ZØNAL SECTIØN AT Y= 160KM
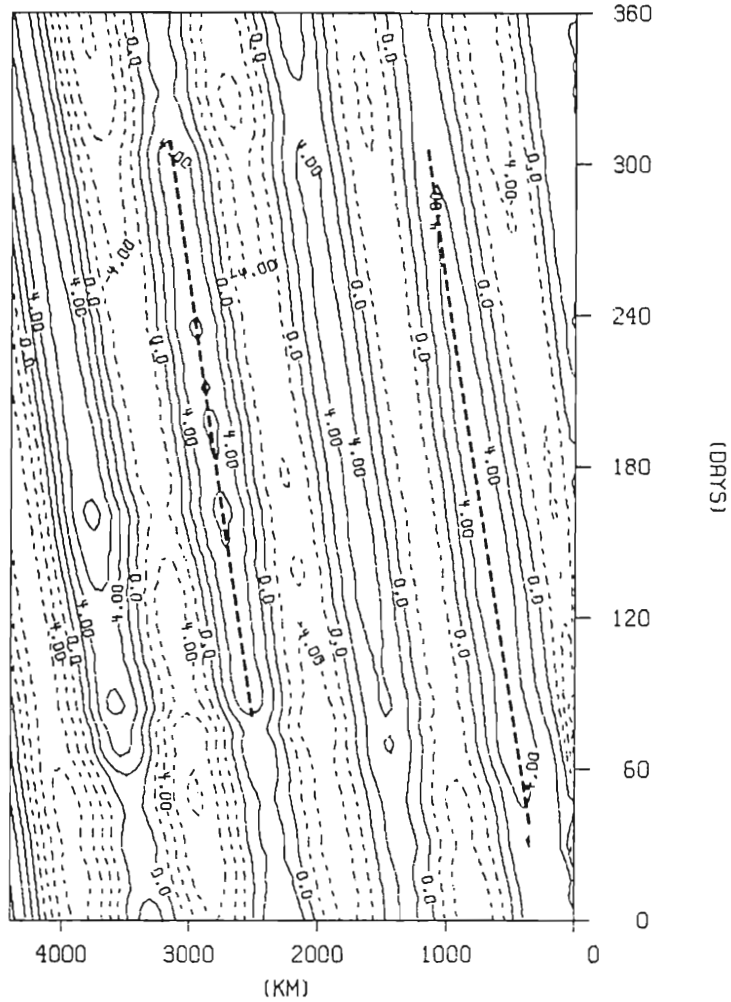
Figure 18. Flat bottom case. Mid latitude x-t plot of the interface height. The heavy dashed lines indicate westward phase propagation of 3.4 cm sec^{-1} (right) and 3.25 cm sec^{-1} (left). Units are in meters. CI is 2.

BARØCLINIC HEIGHT (METERS)
MERIDIØNAL SECTIØN AT X=3640KM
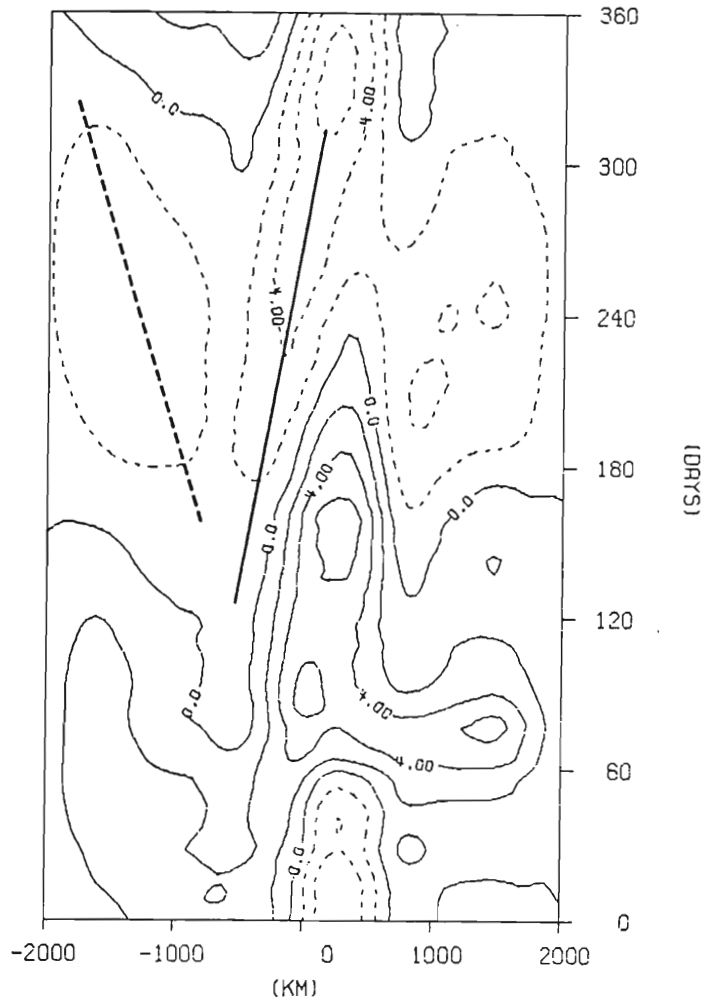
Figure 19. Flat bottom case. Western y-t plot of the interface height. The full heavy line indicates that northward phase propagation occurs at mid latitude; phase speed is $4 \, cm \, sec^{-1}$. The heavy dashed line shows a phase velocity of 6.6 $cm \, sec^{-1}$ to the south. Units are in meters. CI is 2.

possible to evaluate the characteristics of the latest waves by

observing the zonal phase speed of the composed signal. Such

calculation yields zonal and meridional wavenumbers which are

k = 2π/990km and l = 2π/960km respectively. Therefore the

wavelength is λ = 690 km, and the phase propagates north-westward

with an angle of 46° to the north of the east-west direction. Zonal

and meridional phase speeds are 3.14.cm sec^{-1} to the west and 3.04 cm

sec^{-1} to the north respectively. The group velocity is mainly

westward at 2.70 cm sec^{-1} but has a small southward component of 0.45

cm sec^{-1}. It is worthy to note that these calculations are based

only on the knowledge of the waves coming from the eastern boundary

and the zonal phase speed of the observed signal. Once the locally

generated waves are determined, it is possible to calculate

additional details of the composed signal. Its calculated meridional

phase speed is to the north at 3.94 cm sec^{-1}, which is in good

agreement with the phase speed of 4 cm sec^{-1} outlined by the heavy

line in Fig. 19. The calculated wavenumber vector makes an angle of

17° to the north of the east-west direction, which is still in good

agreement with the patterns observed in Fig. 16.

The generation of the waves in the mid-ocean is due to the lower

order EOFs. The source region is essentially located on the mode

line of the first EOF which should not account for much of the local

forcing. But the second and third EOFs show high amplitude and large

gradients in the source region. They also have shorter meridional

and zonal lengthscales and are certainly quite capable of generating

first mode baroclinic Rossby waves.

IV. THE RIDGE EXPERIMENT

In this section the results of the ridge experiment are analyzed
and compared with the results of the flat bottom case (also referred
as the reference experiment), in order to emphasize the influence of
the mid-ocean ridge on the model response. We recall that this work
focuses on the influence of the mid-ocean ridge on the propagation of
the planetary waves generated at the eastern boundary and on the role
of that topography as a source of waves able to radiate energy away
from their region of generation. Therefore the dynamics which occur
over the topography are investigated only if they relate to those
phenomena. Features such as trapped topographic waves which vanish
outside the topography are not considered.

In a two-layer model, the presence of bottom topography results
in a coupling of the barotropic and baroclinic modes. The equation
for the barotropic mode is obtained by adding equation (1) multiplied
by H_1/H with equation (2) multiplied by H_3/H. The equation for the
baroclinic mode is obtained by substracting (2) from (1). The
frictionless linear version of these equations is,

$$\frac{\partial}{\partial t}\nabla^2\phi + \beta\frac{\partial\phi}{\partial x} - J(\frac{f_o}{H}h,\phi) = \frac{\text{curl}\tau}{\rho H} - \frac{H_1}{H}J(\frac{f_o}{H}h,\psi) \tag{5}$$

$$\frac{\partial}{\partial t}(\nabla^2\psi - \frac{1}{R^2}\psi) + \beta\frac{\partial\psi}{\partial x} - \frac{H_1}{H_3}J(\frac{f_o}{H}h,\psi) = \frac{H}{H_1}\frac{\text{curl}\tau}{\rho H} - \frac{H}{H_3}J(\frac{f_o}{H}h,\phi) \tag{6}$$

61

where $\phi = \dfrac{H_1}{H} \psi_1 + \dfrac{H_3}{H} \psi_3$ is the barotropic streamfunction,

$\psi = \psi_1 - \psi_3$ is the baroclinic streamfunction and R is the internal

radius of deformation. The last term on the RHS of these equations

describes the coupling between the two modes. It is interesting to

note that the barotropic mode feels the full effect of the

topography, whereas in the baroclinic equation those effects are

reduced by a ratio H_1/H_3. On the contrary, the wind forcing is more

important in the baroclinic mode. Therefore the coupling terms in

(5) and (6) may be as large as the wind forcing. These equations

will be recalled when the processes of wave generation or wave

reflection by the ridge are investigated. The analysis follows the

same order as in the flat bottom case.

A.   The Gross Features of the Time-Dependent Response

Figure 20 and 21 display maps of the instantaneous

streamfunction and vorticity field in each layer. As in the

reference experiment, the streamfunction is barotropic at large

lengthscales (basin size), whereas baroclinic features only appear at

shorter scales of about 500 km. But, in the ridge case, short-scale

barotropic features are also noticed over the topography and in the

eastern basin. A comparison between the lower layer streamfunctions

of the flat (Fig. 8) and the ridge (Fig. 20) case shows that the

ridge does not greatly affect the lower layer circulation in the

western basin. On the contrary, drastic changes occur on the ridge
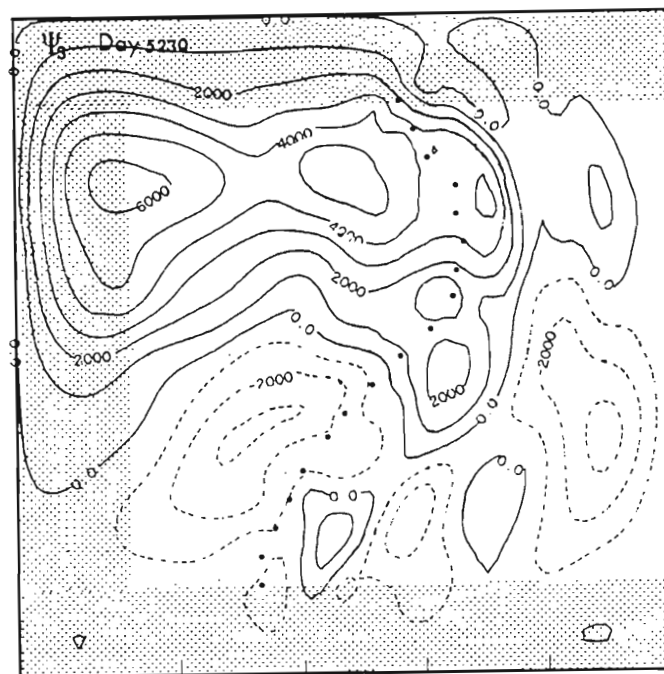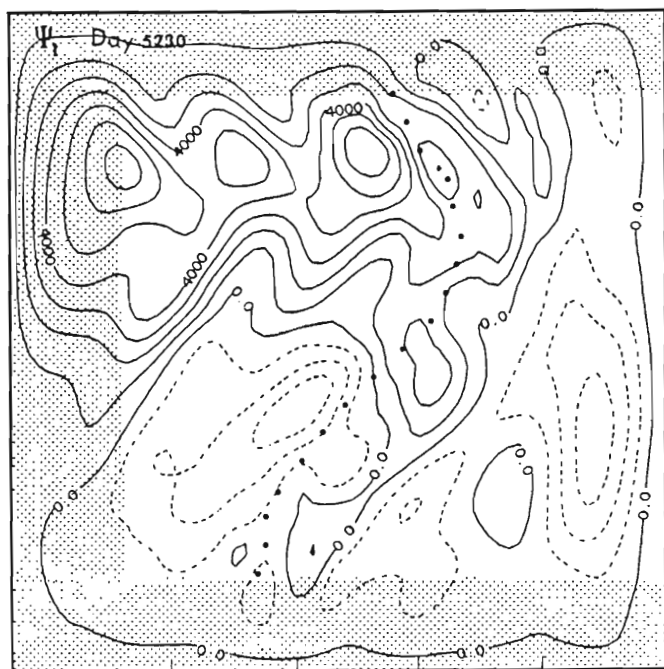
Figure 20. Ridge case. Instantaneous maps of the upper (top) and lower (bottom) streamfunctions. Sponge regions are shaded. The heavy dotted line is the ridge crest. Notice the mesoscale barotropic patterns over the ridge and the barotropic mode-like waves in the southeastern basin. The baroclinic features of the upper layer seems oriented relatively to the topography. Units are m^2 sec^{-1}. CI is 1000.
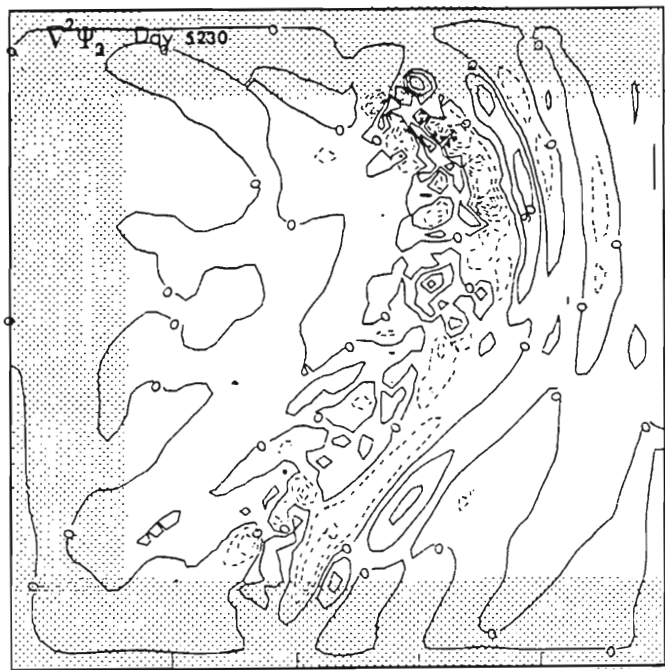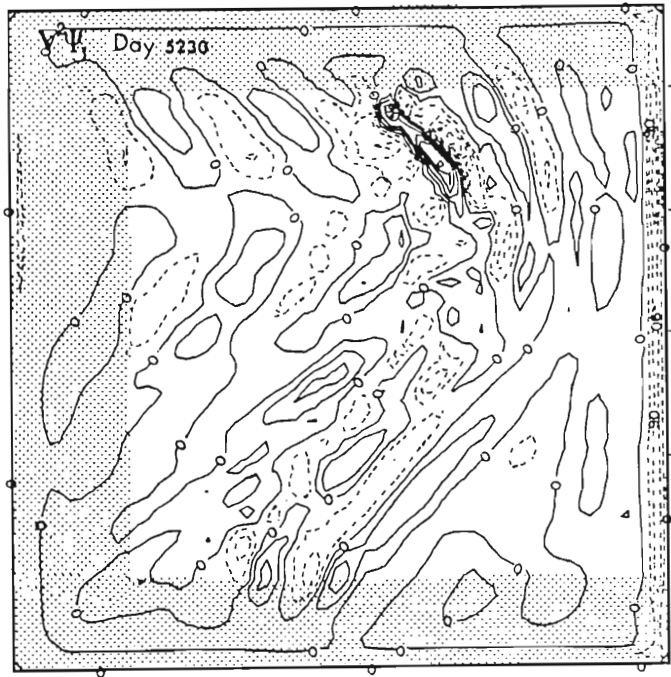
Figure 21. Ridge case. Instantaneous maps of the upper (top) and lower (bottom) vorticity field at day 5230. (March 30, year 15). Sponge layers are shaded. The ridge is a source of vorticity in both layers. Notice the baroclinic planetary waves in the western basin and the barotropic one in the eastern basin. Contour interval is 0.45×10^{-7} sec^{-1}.

where the streamlines tend to follow the topography and where closed-streamline patterns having a lengthscale of a few hundred kilometers indicate that topographically forced waves are important in that region. This fact is emphasized by the series of small-scale vorticity cells spread along the ridge in the maps of relative vorticity in Fig. 21.

Off the ridge in the eastern basin both upper and lower vorticity maps (Fig. 21) show cells of relative vorticity stretched in the long-slope direction. These features correspond to the wave-like pattern observed in the streamfunction in Fig. 20. They are attributed to barotropic Rossby waves generated on the topography which propagate energy eastward.

Figure 22 displays the frequency spectra for the upper and lower layer velocities at four different locations. Again the spectra are barotropic at frequencies larger than 0.02 cpd which correspond to the frequency band where propagative waves dominate the model response. At lower frequencies the spectra are characteristic of the barotropic Sverdrup balance and indicates significant annual-period baroclinic waves.

A brief comparison of these spectra with those of the flat bottom case (Fig. 10) confirms what has already been discussed. West of the ridge spectra are not very different, which indicates that the western barotropic circulation is not significantly affected by the ridge. On the topography the ridge-spectra show a broad peak at
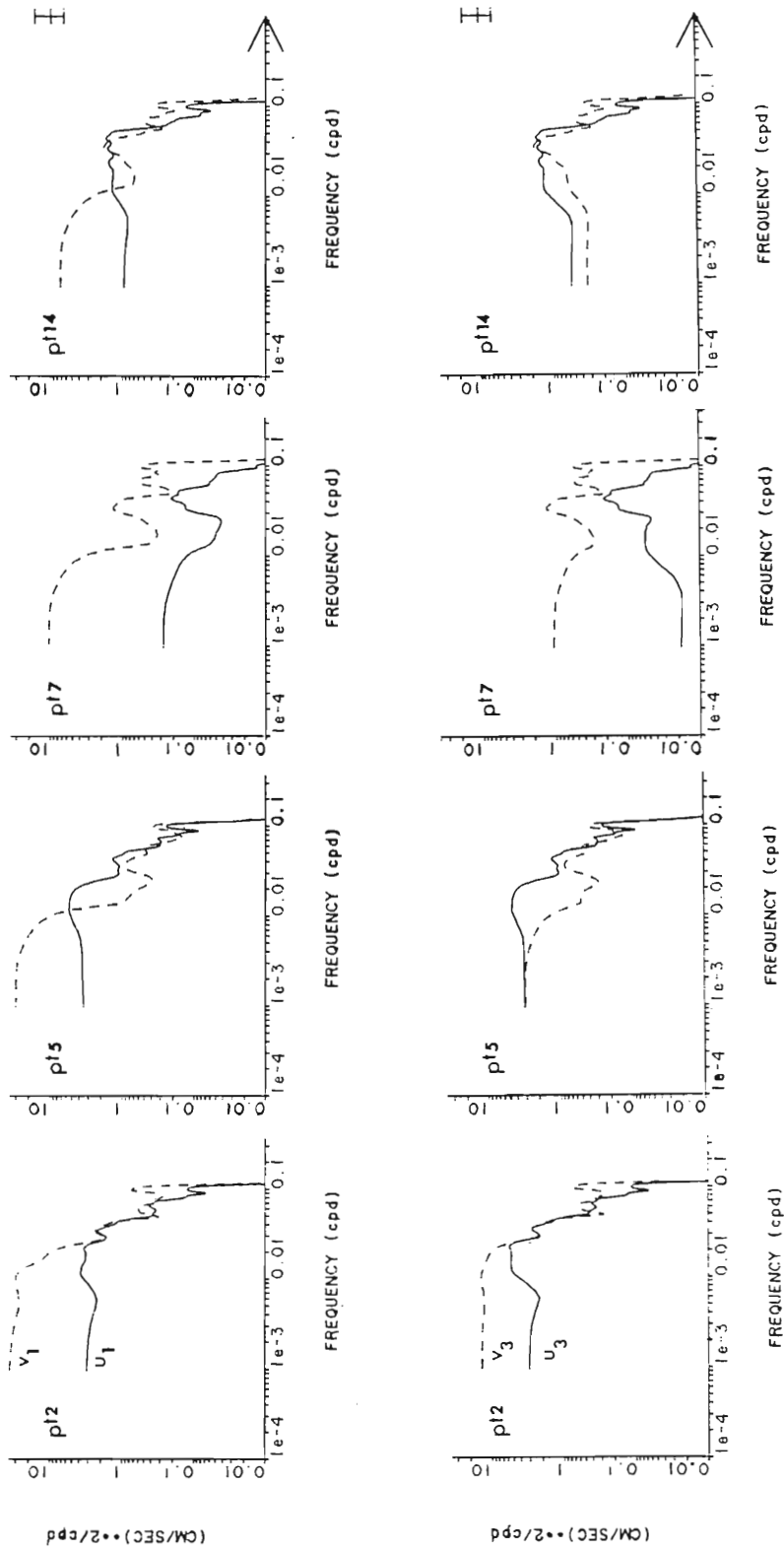
Figure 22. Ridge case. Frequency spectra for the upper layer velocities (top) and the lower layer velocities (bottom) at points 2, 5, 7, 14 of Fig. 2. The same comments as for the flat bottom case hold.

frequencies ranging from 0.01 cpd to 0.05 cpd, while the flat-bottom spectra show gaps in that band. This peak can be attributed to barotropic topographic waves. In the eastern basin the ridge case is differentiated from the flat bottom case by a peak centered around 0.03 cpd. Topographically generated barotropic Rossby waves propagating energy eastward are certainly responsible for that peak. But if these waves travel fast enough to be significantly reflected at the eastern boundary, it will be more appropriate to discuss modes of the half-basin.

It is more appropriate to comment on the baroclinic response using maps of the upper layer streamfunction and relative vorticity. As in the flat bottom case, the eastern boundary appears as a major source of annual period baroclinic Rossby waves. But, in the ridge case, the topography also is a continuous source of annual period baroclinic waves. Their phase propagation seems to be determined by the orientation of the ridge. The amplitudes seem to be larger than for those waves issued from the eastern boundary.

The time-mean streamfunctions show few interesting features. The currents are very weakly rectifying, even on the topography. Although plots of the time-mean quantities are not shown, a few comments are worth making. The upper layer mean transport is somewhat larger in the ridge case (0.16 Sv instead of 0.12 Sv in the flat bottom case). This is because the baroclinic waves generated by the topography have larger amplitudes and therefore are more

68

rectifying than the waves generated at the eastern boundary. In the
lower layer, topographic waves generate mean currents which may yield
to local mean transports of about 0.28 Sv on the slopes of the
ridge. But these transports do not extend for more than a few
hundred kilometers and have no incidence on the large scale mean
transport, which remains insignificant.

B. The Barotropic Response

The previous section described important features of the
barotropic response. The western basin circulation is not very
different from that of the flat-bottom experiment. Barnier's (1986b)
analytical model of the mid-ocean ridge showed that the effect of the
topography on the high frequency mode-like waves is to increase their
frequency, which is exactly what happens to the 10 and 15 day peaks
that have been observed in the flat-bottom experiment. A detailed
analysis of the spectra of Fig. 22 shows that in the ridge experiment
the peaks occur around day 9.5 and 13. As illustrated in Fig. 23
which displays the instantaneous equivalent barotropic height for
both experiments, significant changes due to the ridge concern mostly
the eastern basin and the ridge region itself.

The topography generates wind-forced long planetary waves which
radiate energy westward, but those waves have a low energy density
and do not modify significantly the variability of the western
basin. Short energetic Rossby waves with eastward group velocity are
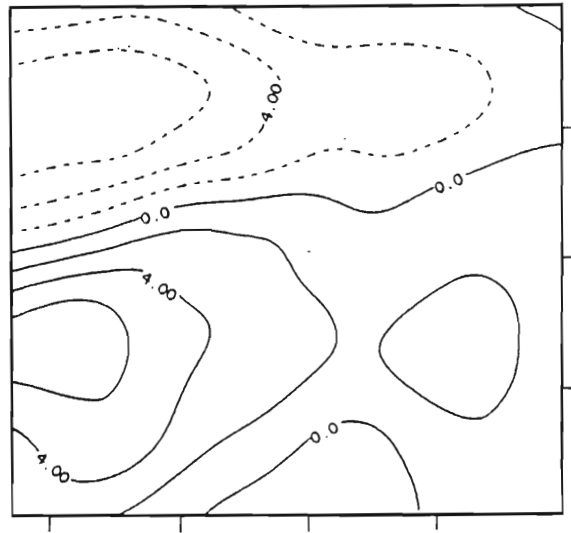
TIME= 4821
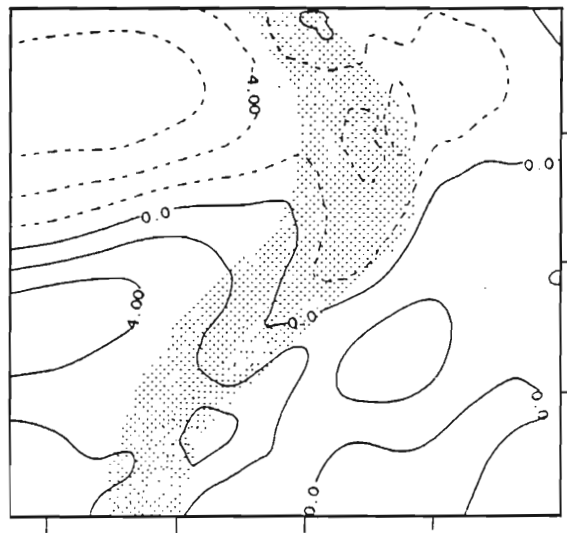
TIME= 4821

Figure 23. Instantaneous maps of the barotropic streamfunction at day 4821 (February 24, year 14). (a) Flat-bottom case and (b) ridge case. Significant differences concern the ridge region and the eastern basin. The ridge region is shaded. Units are in centimeters. CI is 2.

also generated in the ridge region, or by direct wind forcing, or by wave reflection. Fig. 24 displays the partition of the barotropic eddy kinetic energy. It shows that those short waves radiate energy off the ridge in a direction which is mainly eastward but somewhat normal to the ridge crest. Consequently, the energy in the eastern basin is increased (more than 2 times larger than in the flat bottom case). The spectra of Fig. 22 show that this additional variance is concentrated at frequencies ranging from $\omega = 0.01$ cpd to 0.06 cpd with a maximum around $\omega = 0.035$ cpd, which is interpreted as the signature of normal modes of the eastern basin. Such modes, having a frequency of the order of 0.04 cpd, are important features in Barnier's (1986b) study. Their generation is attributed to the low wavenumbers of the forcing. Fig. 25 displays an x-t plot of the barotropic streamfunction. The section is located at $y = -640$ km and is directly comparable with the section of Fig. 12 for the flat-bottom experiment. The eastern basin shows more variability and smaller phase speeds, indicating that short waves are generated by the ridge. Indeed, eastward group velocities are a dominant feature in the eastern basin.

The existence of smaller-scale barotropic patterns over the topography is common to most of the plots presented in the subsection. This fact, already mentioned in the vorticity maps of Fig. 21, is a striking feature in Fig. 24 where the partition of the eddy barotropic kinetic energy presents many pools of high energy
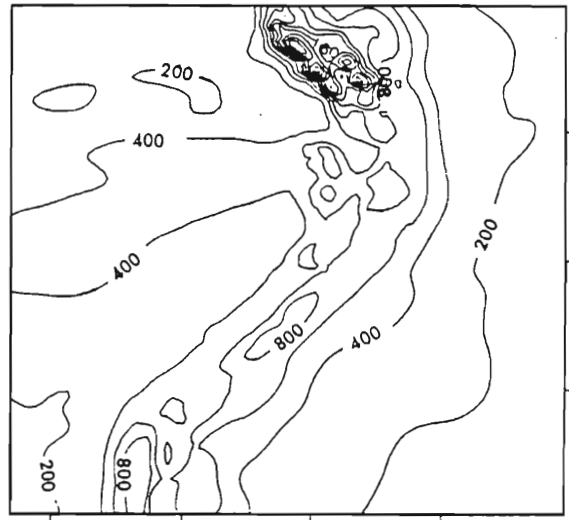
BARØTRØPIC EDDY KINETIC ENERGY

Figure 24. Ridge case. Vertically integrated, mean barotropic eddy kinetic energy. The energy seems to be trapped over the ridge or to radiate eastward off the topography. Units are in $m(m^2sec^{-1})$. CI is 0.02. Labels are scaled by 10^4.

BARØTRØPIC HEIGHT (METERS)
ZØNAL SECTIØN AT Y= -640KM

Figure 25. Ridge case. Mid latitude x-t plot of the equivalent barotropic height. The ridge region is shaded and the ridge crest is the heavy dotted line. Heavy dashed lines indicate eastward group velocity of about 1 m sec^{-1}. Heavy full lines show phase speed of about 1.1 m sec^{-1}. Units are in meters. CI is 0.01.

level scattered along the ridge. They are interpreted as the

signature of forced topographic waves. These waves are

topographically trapped in the sense that they do not propagate

energy outside the ridge region. Nevertheless, they are responsible

for the high energy levels found in that region. It must be said

that these waves may also be seen in the baroclinic signal since the

topography couples the barotropic and baroclinic modes. That

coupling is quite noticeable in the partition of the baroclinic

energy displayed in Fig. 30 where the cells of high energy that are

observed on the northwestern flank of the ridge are very similar to

those seen in the same region in the barotropic energy (Fig. 24).

C.   The Baroclinic Response

Fig. 26 shows the instantaneous baroclinic height during the

spin-up of the ridge experiment, and Fig. 27 displays maps of the

same variable during the 14th and 15th years of the model integration

when the flow is in statistical equilibrium. Both the eastern

boundary and the mid-ocean ridge appear as significant sources of

annual-period baroclinic Rossby waves.

The waves generated at the coast are identical to those of the

flat-bottom case. The behavior of these waves when they reach the

ridge is illustrated in the x-t plots of Fig. 28. The pictures show

that the signal from the east slows down when it enters the ridge

region, reduces its amplitude, and disappears over the topography.
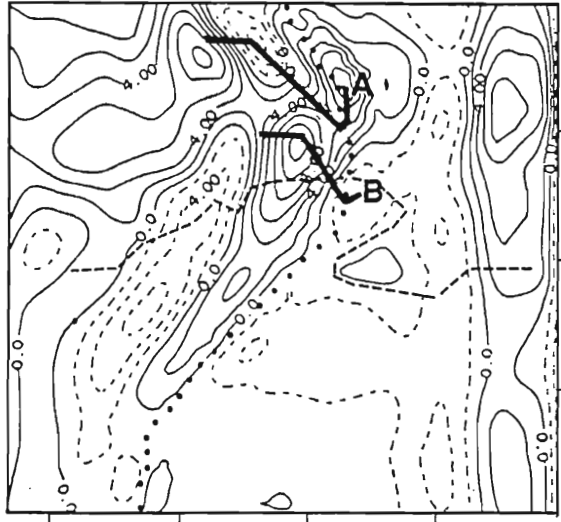
TIME=   436

Figure 26. Ridge case. Instantaneous map of the interface height at
day 436 of the spin-up. The eastern boundary and the ridge are
sources of baroclinic waves. The ridge crest is the heavy dotted
line. The forcing has opposite sign on each side of the heavy dashed
line which show the node line of the first EOF. The signals
generated by the wind in A and B have opposite sign and propagate
along the f/h contours (heavy full line). This explains the phase
opposition that exists between the northern and the central waves.
Units are in meters. CI is 2.
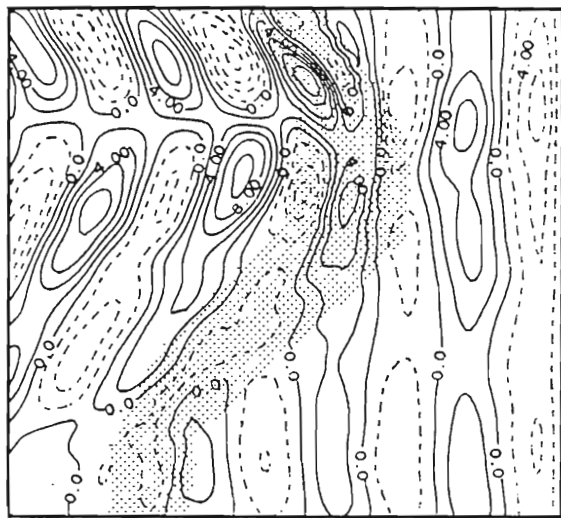
TIME= 4571
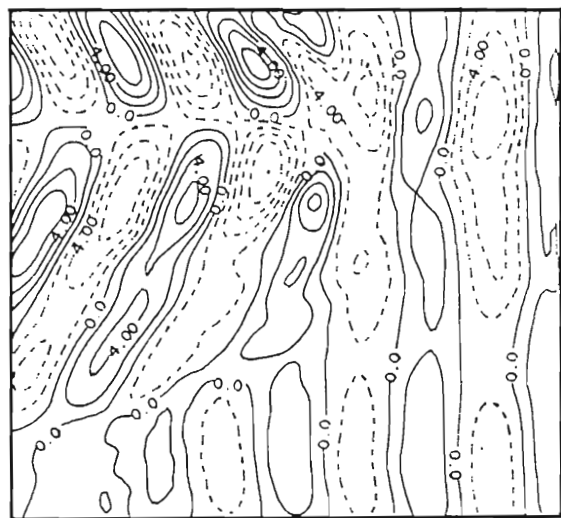
TIME= 4691
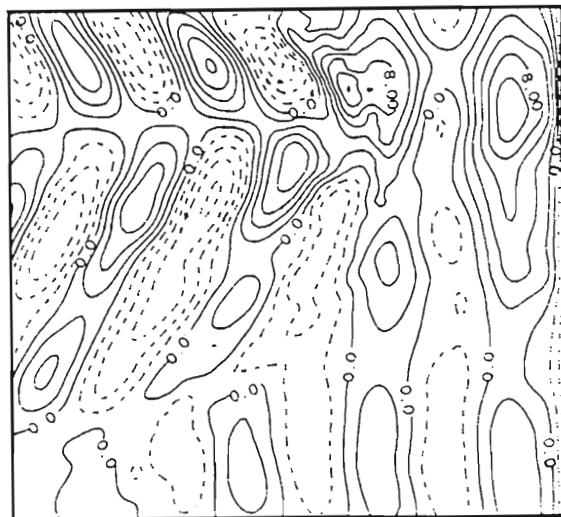
TIME= 4821
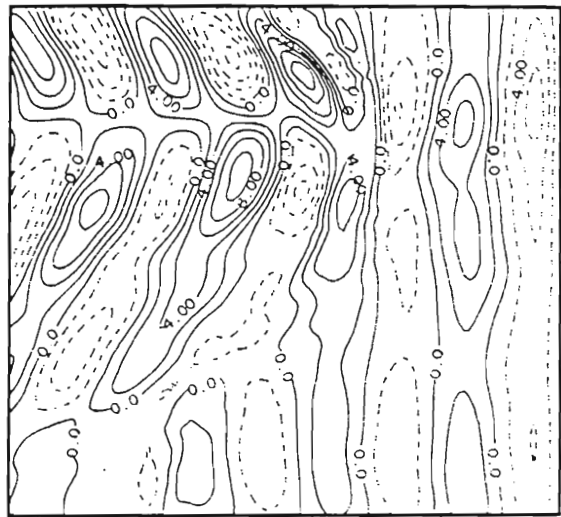
TIME= 4941

Figure 27. Ridge case. Maps of the interface height at four
different times separated by 120 days. The first plot is June 9 in
year 13 (day 4571) and has the ridge region shaded. The similarity
of the first and last plots illustrates the annual period of the
field. The wave patterns in the western basin are oriented like the
ridge crest. They present a phase opposition on each side of
y=1000km. The wave field coming from the eastern boundary does not
seem to pass the ridge. Units are in meters. CI is 2.

This means that the incident baroclinic waves are blocked and damped by the topography. The process can be understood from equations (5) and (6). Part of the incident energy is reflected into short waves whose characteristic lengthscale is the internal radius of deformation. Those waves are dissipated by the biharmonic lateral friction over a few time steps. The part of the incident signal which is not reflected verifies the following equations:

$$J(f + f_0 \frac{h}{H}, \phi) = \frac{H_1}{H} J(\frac{f_0}{H} h, \psi) \qquad (7)$$

$$\frac{1}{R^2} \frac{\partial \psi}{\partial t} + J(f + \frac{H_1}{H_3} f_0 \frac{h}{H}, \psi) = \frac{H}{H_3} J(f_0 \frac{h}{H}, \phi) \qquad (8)$$

These equations are obtained from the unforced version of (5) and (6) under the hypothesis of low-frequency motions ($\omega = 1$ cpy $= \beta R^2/L$) and the long wave approximation ($L^2 \gg R^2$), L is a lengthscale characteristic of the wave motion. The barotropic motion over the ridge takes its energy from the incident baroclinic waves through the coupling term of (7). That motion is across the f/h contours. In the model it is dissipated by bottom friction, with a damping time scale of 115 days. Therefore over the topography the baroclinic waves (which are the continuity of the incident waves) loose their energy in building up a barotropic motion trapped over the topography, the latest being dissipated by bottom friction. That process has a signature on the maps of the eddy energies in Fig.

BARØCLINIC HEIGHT (METERS)
ZØNAL SECTIØN AT Y= 1360KM
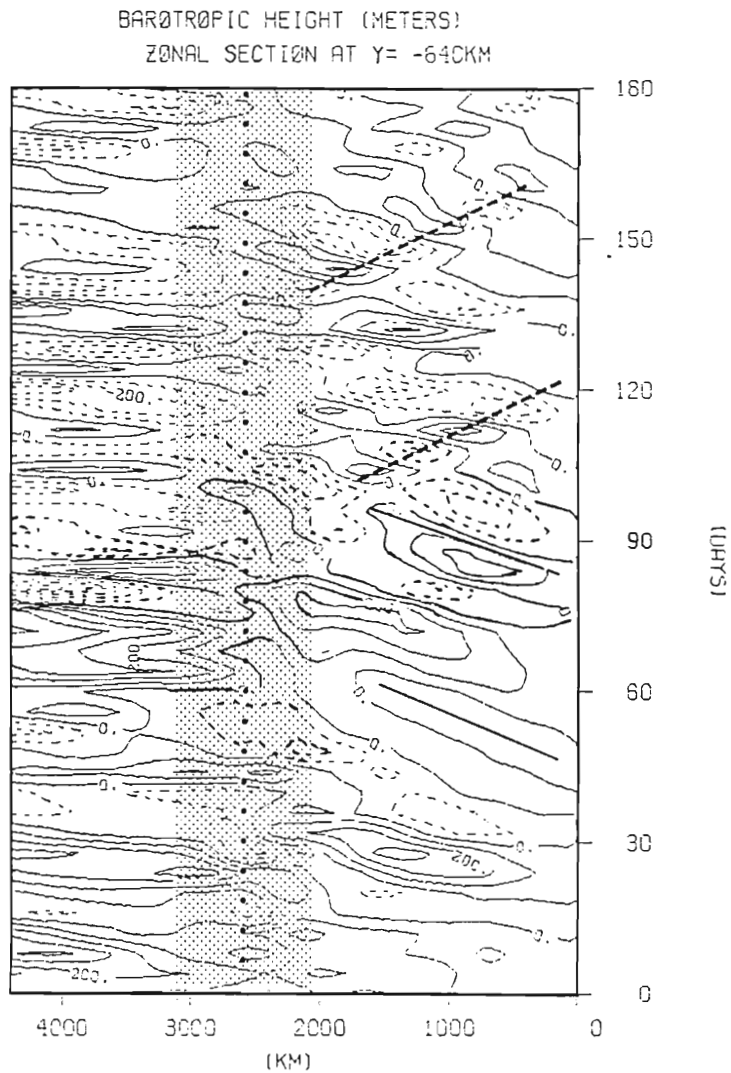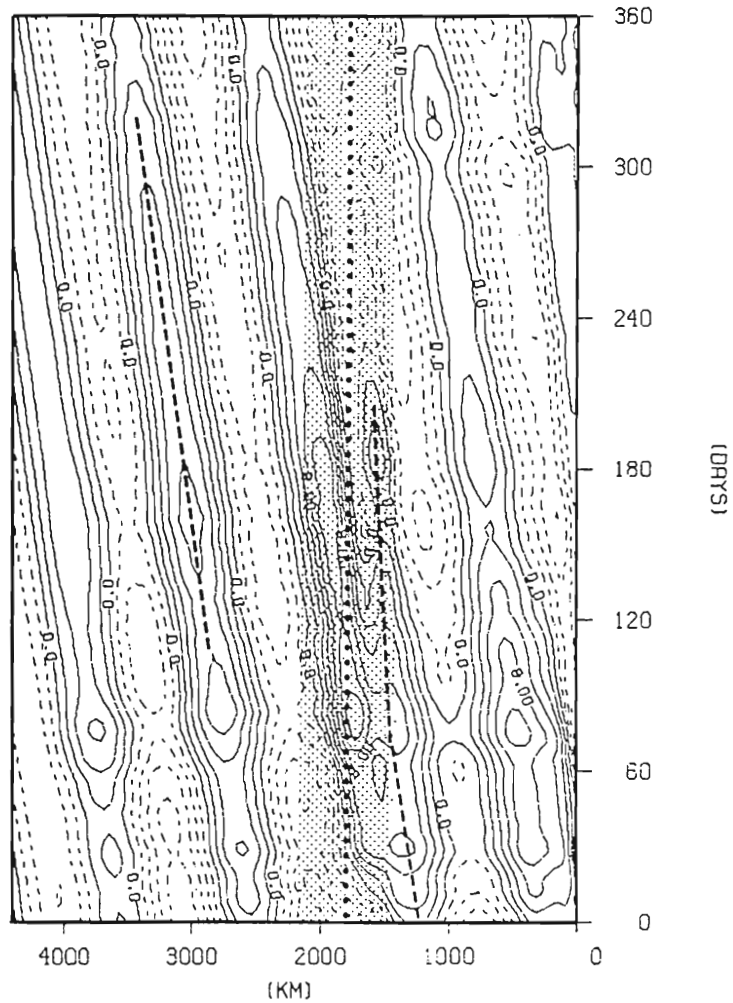
Figure 28. Ridge case. Northern x-t plot of the baroclinic
height. The ridge region is shaded and the ridge crest is the heavy
dotted line. The heavy dashed line west of the ridge indicates a
westward phase speed of $3.22 \, \mathrm{cm\,sec^{-1}}$. The heavy dashed line east of
the ridge illustrates the damping of the signal coming from the
eastern coast. Units are in meters. CI is 2.

30.   It certainly contributes to the cell of high kinetic energy on the eastern flank of the ridge that faces the intense wave source of the eastern boundary.

The waves generated over the topography have an amplitude similar to that of the waves issued from the eastern boundary.   The tilting of the wave patterns in Fig. 27 indcates a significant meridional propagation of the signal.   The orientation of the bottom topography certainly plays a dominant role in the determination of the meridional wavenumber.   In the northernmost part of the basin (y > 1000 km) the signal is out of phase with the signal to the south and propagates toward the southwest, indicating that the waves have north-westward group velocities.   In the central basin (-1000 km < y < 1000 km) the phase speed is to the northwest, and therefore the waves radiate energy southwestward.   The quantities that characterize those waves are drawn from the dispersion relation and x-t and y-t plots of the baroclinic height as displayed in Fig. 28 and Fig. 29 and summarized in Table 3.   The corresponding meridional phase speeds are outlined in Fig. 29.   The zonal phase speed at the latitude y = 1400 km is shown in Fig. 28.   The general orientation of the energy patterns in Fig. 30 is quite consistent with the group velocities of Table 3.   In every case the meridional component of the group velocity is small.

The process of generation of these waves can be understood with the long-period ($\omega = 1$ cpy $\approx \beta R^2/L$), long-wave ($L^2 \gg R^2$)   version of

Table 3

Characteristics of the topographically generated annual period baroclinic Rossby waves calculated at three different latitudes. x means zonal and y means meridional. Negative sign means to the east for the x-quantities and toward the south for the y-quantities.

Latitude y =	1400 km	600 km	-600 km
x - phase velocity	+ 3.22 cm sec^{-1}	3.30 cm sec^{-1}	3.26 cm sec^{-1}
y - phase velocity	*-3.65 cm sec^{-1}	*4.56 cm sec^{-1}	*4.03 cm sec^{-1}
x - group velocity	2.79 cm sec^{-1}	2.86 cm sec^{-1}	2.83 cm sec^{-1}
y - group velocity	0.34 cm sec^{-1}	-0.32 cm sec^{-1}	-0.36 cm sec^{-1}
x - wavenumber	2π/1020km	2π/1040km	2π/1030km
y - wavenumber	-2π/1150km	2π/1430km	2π/1270km

+ = outlined in Fig. 28.   * = outlined in Fig. 29

BAROCLINIC HEIGHT (METERS)
MERIDIONAL SECTION AT X=3640KM
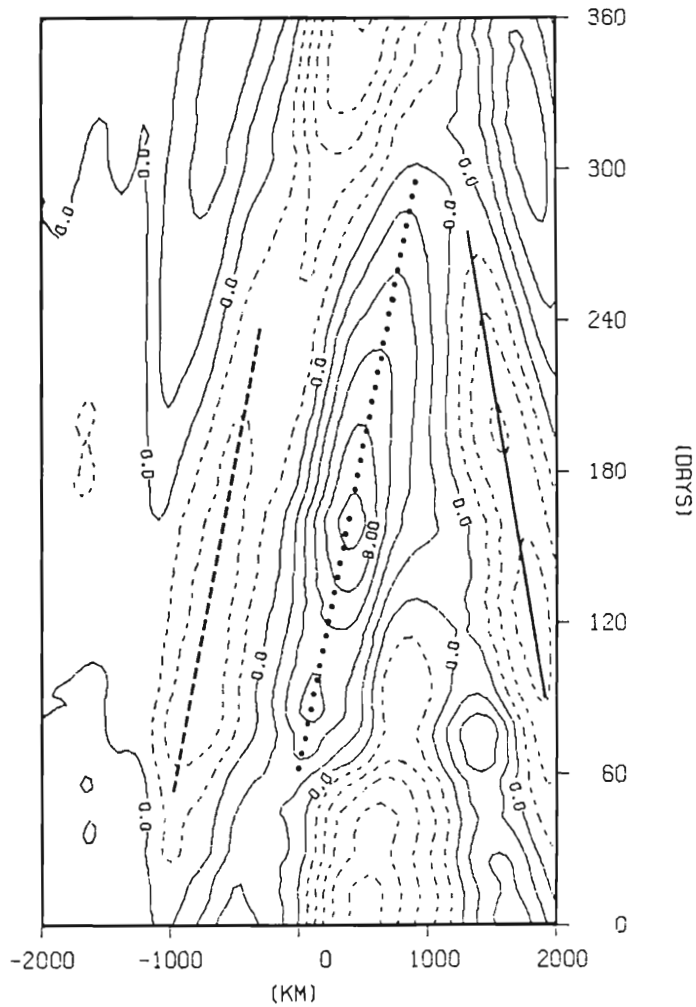
Figure 29.   Ridge case.   Western y-t plot of the interface height.
The section is completely west of the ridge.   The heavy lines show
phase speeds southward at 3.65 cm sec^{-1} (full line), northward at 4.56
cm sec^{-1} (dotted line) and 4.03 cm sec^{-1} (dashed line).   Units are in
meters.   CI is 2.

equations (5) and (6);

$$\beta \frac{\partial \phi}{\partial x} - J(\frac{f_o}{H} h, \phi) = \frac{Curl\tau}{\rho H} - \frac{H_1}{H} \frac{f_o}{H} J(\frac{f_o}{H} h, \psi) \tag{9}$$

$$-\frac{1}{R^2} \frac{\partial \psi}{\partial t} + \beta \frac{\partial \psi}{\partial x} - \frac{H_1}{H_3} J(\frac{f_o}{H} h, \psi) = \frac{H}{H_1} \frac{Curl\tau}{\rho H} - \frac{H}{H_3} J(\frac{f_o}{H} h, \phi) \tag{10}$$

These equations do not allow any signal to propagate eastward, because the ridge has a global meridional orientation. Therefore the meridional topography gradients are not large enough to overcome the β-effect. Considering that the β-effect and the topographic effects have an equivalent strength, a simple scaling of these equations shows that in (9) the coupling term is as important as the wind forcing, whereas in (10) it is smaller in a ratio H_1/H_3. As a result, a discontinuity in the barotropic streamfunction can be removed by generation of a baroclinic signal which will propagate westward. This is how the generation of the baroclinic Rossby waves is explained. Equation (9) shows that the annual-period fluctuations of the wind stress curl drive a barotropic motion of identical period that obeys a topographic Sverdrup balance in which the direction of the zonal velocity depends on the zonal gradients of the topography. Therefore the barotropic zonal velocity is in the opposite direction on each side of the ridge and is discontinuous at the ridge-crest. The discontinuity is removed by the generation of an annual-period baroclinic signal which will match the velocities at

the crest through the coupling term. The baroclinic signal obeys (10) in which the coupling term and the forcing are in phase. Resonant amplification of the signal may occur and yields wave amplitudes as large as those of coastally generated waves. They propagate westward as annual-period baroclinic Rossby waves. Their phase is characterized by the long-slope wavenumber of their generation, which explains why the tilting of the wave-patterns in Fig. 27 is oriented like the ridge crest. It can be said more physically that at the annual cycle the wind-driven lower-layer transport in the cross-slope direction has an opposite sign on each flank of the ridge. That creates an alternation in time of convergence and divergence of the fluid masses in the region of the ridge crest and results in up and down oscillations of the interface height over the ridge. That baroclinic signal is in phase with the wind forcing and that may result in its amplification. It then propagates westward in the form of baroclinic Rossby waves having their crests somewhat parallel to the ridge crest.

The phase shift of π between the waves generated north of y = 1000 km and those generated south of y = 1000 km is due to the similar phase difference that exists in the forcing in the ridge region. Over the ridge the mode line of the first EOF which separates its northern cell of large amplitude from its southern cell of smaller amplitude and opposite sign is located around y = 1000 km and is plotted in Fig. 26. Therefore the waves are generated in a
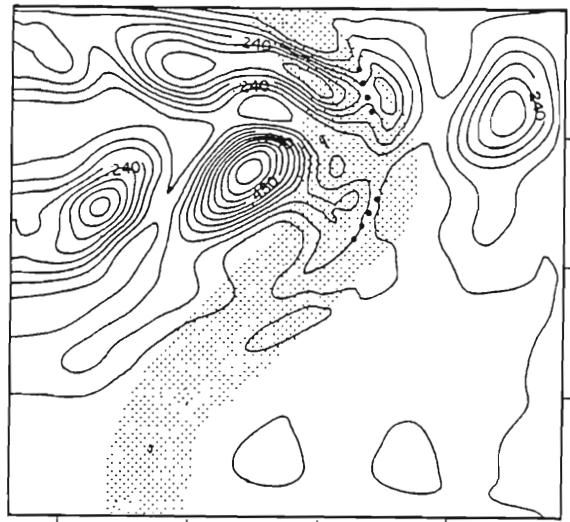
EDDY POTENTIAL ENERGY
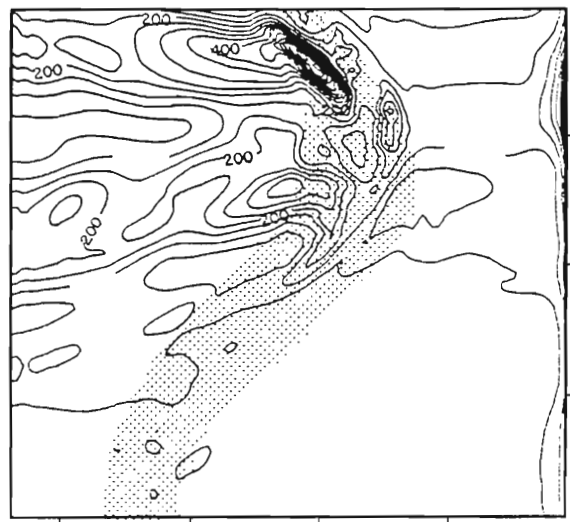
BAROCLINIC EDDY KINETIC ENERGY

Figure 30. Ridge case. Vertically integrated, mean eddy kinetic
energy. The heavy dots indicate sources of annual-period baroclinic
Rossby waves. The potential energy presents a succession of maxima
characteristic of coastally and topographically generated waves.
Some intense features over the ridge are also noticed in the
barotropic kinetic energy of Fig. 24. They are attributed to bottom
trapped topographic waves. The ridge region is shaded. Units are
$m(m^2 sec^{-2})$. CI is 0.06 for the potential energy and 5×10^{-3} for the
kinetic energy where labels are scaled by 10^4.

region where the forcing has an opposite sign on each side of y =
1000 km. The signal propagates along the f/h contours as indicated
in Fig. 26. It results in the phase opposition observed in the wave-
patterns.

When the waves propagate in the western basin, they combine with
the locally forced response just like the coastally generated waves
described in the flat-bottom experiment. Therefore the
topographically generated waves also have a spatial modulation in
amplitude, which is quite observable on the x-t plot in Fig. 28 and
is responsible for the series of maxima that are observed in the maps
of eddy potential energy in Fig. 30.

V. CONCLUSION

The study presented in the previous sections investigated, in a numerical model simulation, the influence of the mid-Atlantic ridge on the propagation of non-linear barotropic and first-mode baroclinic Rossby waves generated by seasonal wind-fluctuations. The North Atlantic is simulated by a square-box, wind-driven, two-layer quasi-geostrophic ocean model. The bottom topography is ridge-like and compromises the quasi-geostrophic approximation and the realistic shape of the mid ocean ridge. Sponge layers are introduced at the western and zonal boundaries of the model in order to prevent wave reflection. The model is forced by a purely fluctuating wind (of zero mean) derived from the FGGE data (FGGE = First Global GARP Experiment). The four most significant EOF's of the perturbation wind-stress curl obtained from these data compose the forcing function, which thus realistically represents the large-scale seasonal fluctuations of the wind-stress curl over the North Atlantic. The first EOF which can be related to the seasonal oscillations of the intensity of the subpolar low and subtropical high is the most important component of the forcing. It accounts for 45% of the forcing function, its oscilations in the northern basin have the largest amplitude and are out of phase with those of the southern basin, and it contains significant variance at the annual

85

cycle. Two experiments were run, one with a flat-bottom and the other with the ridge-like topography. The results were analyzed and compared from the barotropic and baroclinic response.

The barotropic response of the flat bottom experiment reproduces many features of the study of Willebrand et al. (1980). The effects of the ridge on the variability of the eastern basin agree with the results pointed out by the analytical model of the mid-ocean ridge of Barnier (1986b). High frequency mode-like Rossby waves (ω = 1/10 cpd and ω = 1/15 cpd) are generated by the particular large scale structure of the first EOF. The topographic effects on these waves result in an increase of their frequency. At frequencies $\omega \gtrsim 0.02$ cpd, the flat-bottom barotropic response is dominated by directly wind-forced Rossby waves. The most energetic sources of waves are located in the northwestern part of the basin. The waves radiate energy to the west and to the east with a significant southward component due to the higher amplitude of the forcing in the northern basin. At low frequencies ($\omega < 0.02$ cpd) a barotropic Sverdrup's type circulation is dominant. The introduction of the ridge-like topography mostly influences the eastern basin ciruclation. Topographically generated barotropic Rossby waves radiate energy off the ridge region. The long waves have a low energy density and westward group velocities. They disappear in the western sponge layer without modifying significantly the variability of the western basin. However, they would generate a significant

western boundary current if the sponge was removed. The short, highly energetic waves which propagate energy eastward off the ridge do increase the variability of the eastern basin. The lower frequency waves do not travel as fast as the higher frequency waves, and therefore the frequency band for which significant variance is found in the barotropic signal narrows and shifts towards the high-frequencies when we move off the ridge towards the eastern boundary. Normal modes of the eastern half-basin with frequency around 1/25 cpd are also observed.

The flat-bottom baroclinic response is characterized by annual-period baroclinic Rossby waves. Free waves with an amplitude of about 6 meters are generated at the eastern boundary. They propagate energy westward at about 3 cm sec^{-1}. Their wavelength is about 1060 km, and the westward phase speed is 3.4 cm sec^{-1}. The observed signal is a composition of these waves with the local response to the forcing. Since the amplitude and phase of the free waves is somehow determined by the local response at the coast, the combination of those two signals yields an observed signal which has a significant spatial modulation of its amplitude. Indeed, the amplitude locally reaches 10 meters, and its spatial modulation yields a particular distribution of the eddy potential energy: maxima and minima in potential energy alternate off the coast with a wavelength of the order of that of the free waves. As suggested by Lippert and Kase (1985), that partition of the potential energy is considered

characteristic of coastally generated waves similar to White's (1977)

solution. Free waves of smaller amplitude are also generated in the

middle of the basin. They combine with the waves issued from the

eastern boundary to give an observed signal which propagates westward

at 3.25 cm sec^{-1} and northward at 4 cm sec^{-1}. Therefore the group

velocity of the waves generated in the mid-ocean is southwestward,

the southward component (0.45 cm sec^{-1}) being only 16% of the

westward component (2.70 cm sec^{-1}). Their wavelength is about 690

km, and the phase propagates at 46° to the northwest. The topography

has two important effects on the baroclinic response: it damps the

waves coming from the eastern boundary, and it generates new trains

of baroclinic Rossby waves which propagate westward but have a phase

that is strongly influenced by the orientation of the topography.

The wave pattern propagates in a direction almost normal to the ridge

crest. The group velocity is mainly westward at about 2.9 cm

sec^{-1}. The meridional component of the group velocity has a sign

which depends on the orientation of the wave pattern, but its

amplitude is always small (less than 15% of the westward

component). The waves combine with the local response, so the

observed signal also presents a spatial modulation of its amplitude

which yields to an off-ridge alternating of maxima and minima

patterns in the eddy potential energy. It is suggested that the

coupling introduced by the topography between the barotropic and

baroclinic mode is responsible for the damping and the generation

processes. The purely baroclinic waves coming from the eastern boundary loose their energy over the ridge in building-up, because of the coupling, a barotropic motion which is trapped over the topography and is dissipated by bottom friction. Over the ridge the baroclinic waves are generated to insure the continuity of the up-slope velocity on the ridge crest.

The study shows that, when the ocean is driven by seasonal winds, the mid-ocean ridge is a source of baroclinic low-frequency variability. However the baroclinic energy is radiated only to the west, so that the significant source of wind-driven baroclinic variability for the eastern basin is the eastern boundary. Since the ridge tends to block the baroclinic waves coming from the eastern basin, it can be considered as the main source of annual period baroclinic Rossby waves for the western basin. Therefore, if ocean data allow identification of an annual-period signal in the western North Atlantic, a ridge-influenced phase propagation should be sought. On the other hand, the meridional wavenumber content of the wind spectra and the shape of the coastline should determine the phase propagation of the baroclinic signal in the eastern basin. However the ridge is an important source of wind-driven barotropic variability at all frequencies for the eastern basin.

The model has been driven with a forcing that accounts for less than 50% of the wind variability over the north Atlantic. The part of the forcing that has not been considered is stochastic in

nature. It would certainly amplify the response that has been observed, but with more random phases, so the flow would resemble more a wind-driven quasi-geostrophic turbulent flow. It is not clear that a realistic bottom-topography would render that turbulence more baroclinic and thus explain the actual baroclinic aspect of the variability that is observed in the eastern north Atlantic. In any case the present work indicates that the mid-ocean ridge is as important as the eastern boundary to understand the variability of the eastern north Atlantic related to seasonal winds. For that ocean the eastern boundary is a source of baroclinic variability, whereas the ridge generates barotropic variability and is a blocking barrier for the westward traveling energy.

However, the role of the ridge on the eastern ocean variabilty is yet to be resolved. In particular, a recent study of Verron, LeProvost and Holland (1987) indicates that the mean wind forcing may drive a small boundary current on the eastern flank of the ridge which may be favorable to internal instability processes. A step forward in modeling the eastern north Atlantic would be to construct a forcing which includes both a mean and a stochastic part. The model grid should be small enough (less than 20 km) to allow the quasi-geostrophic turbulence to develop. A recent study of Mac Veigh, Barnier and LeProvost (personal communication) suggests that the wind data processed by the European Center for Medium Range Weather forecasts could provide the realistic wind forcing. However

the spectral content of the forcing at scales of the internal radius
of deformation can only be speculated until satellite wind data are
available.

REFERENCES

Anderson, D. L. T., and A. E. Gill, Spin-up of a stratified ocean
with applications to upwelling, Deep-Sea Res., 22, 683-696,
1975.

Barnier, B., Energy transmission by barotropic Rossby waves across
large-scale topography, J. Phys. Oceanogr., 14, 438-447, 1984a.

Barnier, B., Influence of a mid-ocean ridge on wind-driven barotropic
Rossby waves, J. Phys. Oceanogr., 14, 1930-1936, 1984b.

Barnier, B., Investigation of the seasonal variability of the wind
stress curl over the north Atlantic Ocean by means of E.O.F.
analysis, J.G.R. Oceans, 91, 863-868, 1986.

Bernstein, R. L., and W. B. White, Time and length scales of
baroclinic eddies in the central north Pacific Ocean, J. Phys.
Oceanogr., 7, 123-126, 1974.

Bray, N. A., Seasonal variability in the intermediate waters of the
eastern north Atlantic. Doctoral dissertation, 165 pp., MIT,
Woods Hole, Massachusetts, 1980.

Cummins, P. F., L. A. Mysak, and K. Hamilton, Wind-stress curl
generation of annual Rossby waves in the north Pacific, J. Phys.
Oceanogr., 16, 1179-1189, 1986.

Dantzler, R. R., Potential energy maxima in the tropical and
    subtropical north Atlantic, J. Phys. Oceanogr., 7, 512-519,
    1977.

Dickson, R. R., W. J. Gould, P. A. Gurbutt, and P. D. Killworth, A
    seasonal signal in ocean currents to abyssal depths, Nature,
    295, 193-198, 1982.

Emery, W. J., and L. Magaard, Baroclinic Rossby waves as inferred
    from temperature fluctuations in the eastern Pacific, J. Mar.
    Res., 34, 365-385, 1976.

Frankignoul, C., and P. Muller, Quasi-geostrophic response of an
    infinite β-plane ocean to stochastic forcing by the atmosphere,
    J. Phys. Oceanogr., 9, 104-127, 1979.

Gould, W. J., and A. N. Cutler, Long period variability of currents
    in the Rockall Trough, Document No. CM1980/C: 30, ICES
    Hydrography Committee, 1980.

Holland, R. H., The role of mesoscale eddies in the general
    cirulcation of the ocean - Numerical experiment using a wind-
    driven quasi-geostrophic model, J. Phys. Oceanogr., 8, 363-392,
    1978.

Kang, Y. Q., and L. Magaard, Annual baroclinic Rossby waves in the
    central north Pacific, J. Phys. Oceanogr., 10, 1159-1167, 1980.

Krauss, W., and R. H. Kase, Mean circulation and eddy kinetic energy
    in the eastern north Atlantic, J.G.R. Ocean, 89, 3907-3415,
    1984.

Krauss, W., and C. Wuebber, Response of the North Atlantic to annual
    wind variations along the eastern coast, Deep-Sea Res., 29, 851-
    868, 1982.

Lippert, A., and R. H. Kase, Stochastic wind forcing of baroclinic
    Rossby waves in the presence of a meridional boundary, J. Phys.
    Oceanogr., 15, 185-194, 1985.

Munk, W. H., On the wind driven ocean circulation, J. Meteorology, 7,
    79-93, 1950.

Mysak, L. A., Generation of annual Rossby waves in the north Pacific,
    J. Phys. Oceanogr., 13, 1910-1923, 1983.

Pedlosky, J., The stability of current in the atmosphere and the
    ocean: Part I, J. Atmos. Sci., 21, 201-219, 1964.

Pedlosky, J., A note on the western intensification of the oceanic
    circulation, J. Mar. Res., 23, 207-209, 1965.

Pedlosky, J., Geophysical Fluid Dynamics, 624 pp., Springer-Verlag,
    New York, 1979.

Phillips, N., Large scale eddy motion in the western Atlantic, J.
    Geophys. Res., 71, 3883-3891, 1966.

Price, J. F., and H. T. Rossby, Observation of a planetary wave in
    the western north Atlantic, J. Mar. Res., 40, 543-558, 1982.

Robinson, A. R., Dynamics of ocean currents and circulation results
    of POLYMODE and related investigations, Soc. Italiana di Fisica,
    Bologna. (Elsevier, New York), 1982.

Robinson, A. R., Eddies in Marine Science, 609 pp., Springer-Verlag,
New York, 1983.

Schmitz, W. J., W. R. Holland, and J. F. Price, Mid latitude
mesoscale variability, Rev. Geophys. Space Phys., 21, 1101-1119,
1983.

Stommel, H., The westward intensification of wind-driven ocean
currents, Trans. Am. Geophys. Union, 29, 202-206, 1948.

Sverdrup, H. W., Wind-driven currents in a baroclinic ocean, with
application to the equatorial current of the eastern Pacific.
Proceedings of the National Academy of Sciences of the USA, 83,
318-326, 1947.

Swallow, J. C., Measuring deep currents in mid-ocean, New Scientist,
9, 740-743, 1961.

Verron, J., C. LeProvost, and W. Holland, On the effects of a mid-
ocean ridge on the general circulation - numerical simulations
with an eddy resolved ocean model. To appear in J. Phys.
Oceanogr., 1987.

Wajsowicz, R., C., Free planetary waves in finite-difference
numerical models, J. Phys. Oceanogr., 16, 773-789, 1986.

White, W. B., Annual forcing of baroclinic long waves in the tropical
north Pacific Ocean, J. Phys. Oceanogr., 7, 50-61, 1977.

White, W. B., and J. F. T. Saur, A source of annual baroclinic waves
in the eastern subtropical north Pacific, J. Phys. Oceanogr.,
11, 1452-1462, 1981.

Willebrand, J., S. G. Philander, and R. C. Pacanowski, The oceanic
   response to large-scale atmospheric disturbances, J. Phys.
   Oceanogr., 10, 411-429, 1980.

Wunsch, C., Low frequency variability of the sea, in Evol. Phys.
   Oceanogr., 623 pp., MIT Press, 1981.

Wunsch, C., Western north Atlantic interior, in Eddies in Marine
   Science, 609 pp., Robinson ed., Springer-Verlarg, New York,
   1983.

Wyrtki, K., L. Magaard, and J. Hager, Eddy energy in the oceans, J.
   Geophys. Res., 81, 2642-2646, 1976.

APPENDIX A

MEAN AND EDDY ENERGETICS OF A TWO-LAYER

QUASI-GEOSTROPHIC OCEAN MODEL

LIST OF FIGURES

Figure 4.   Total lower layer eddy kinetic energy flux

vector for the ridge experiment of the main

study. It represents the sum of all the flux

vectors of table 2b. The ridge crest is the

heavy dotted line. Maximum vector length is

$4.35 \text{ m}^2(\text{m}^2\text{sec}^{-2})/\text{sec}$.

Figure 5.   Divergence of the lower layer eddy kinetic

energy flux vector displayed in Fig. 4.

Positive values indicate that energy is

radiated into the region. Negative values

indicate that energy radiates out. Units

are in $\text{m}(\text{m}^2\text{sec}^{-2})/\text{sec}$. CI is 10^{-7}.

1. INTRODUCTION

EGCM experiments produce a huge amount of data to be analyzed. Performant diagnostic investigations must be performed in order to infer the physics of the processes that drive the large scale and mesoscale circulation from these data.

Holland (1978) presents horizontally integrated kinetic energy and potential energy equations for a two-layer, quasi-geostrophic, closed ocean basin. Thus he identifies and quantifies the conversion of kinetic energy between the layers and the conversion between kinetic and potential energy. Harrison and Robinson (1978) examine the energy budgets in open subregions of a turbulent flow produced by a primitive equation ocean model. Their purpose was to determine the processes responsible for the production, transfer, and dissipation of energy. Pedlosky (1979) derives a quasi-geostrophic equation of conservation for the total energy that holds at every point. Evans (1984) gives a Lagrangian pointwise formulation of the kinetic and potential energy equations for a two-layer, quasi-geostrophic EGC Model. Because this type of model allows conversion between kinetic and potential energy, the choice of a state of reference may have some consequences. Evans examines this problem and convincingly proposes that for pointwise energy equations the natural level of reference is the state of rest (zero streamfunction). More recently,

Pinardi and Robinson (1986) present a method for local energy and
vorticity analysis of open regions of quasi-geostrophic, continuously
stratified flows. The method aims to permit the description of the
physics of synoptic/mesoscale processes and to identify the signature
of such processes from real and/or simulated data sets.

The present work calculates the mean and eddy part of the
Eulerian kinetic and potential energy equations for a two-layer
quasi-geostrophic model. These equations, which hold at every point
of the ocean basin, give a complete pointwise mean energy budget of a
data set produced by the model (mean = time-averaged over the
duration of the experiment).

2. ENERGY EQUATIONS FOR THE MEAN AND EDDY FLOWS OF A 2-LAYER QG MODEL

When the results of a numerical experiment are analyzed, it is
useful to consider every physical variable that characterizes the
flow as constituted of a mean value (which is the time-averaged value
of that variable over the duration of the experiment) and a
perturbation (or eddy) part of zero mean (which is the difference
between the instantaneous value of the variable and its mean). For
instance, in the two-layer QG model of the main study, the
fundamental fields are the upper layer and lower layer
streamfunctions $(\psi_{1,3}(x,y,t))$ and the vertical velocity field at the
interface $(w_2(x,y,t))$. They are decomposed into their mean and eddy
part with the notations that follow:

$$\psi_1(x,y,t) = \overline{\psi_1}(x,y) + \psi_1{}'(x,y,t)$$

$$\psi_3(x,y,t) = \overline{\psi_3}(x,y) + \psi_3{}'(x,y,t)$$

$$w_2(x,y,t) = \overline{w_2}(x,y) + w_2{}'(x,y,t)$$

The forcing field which is also decomposed into a mean and eddy field is also important.

$$\text{Curl}\tau(x,y,t) = \text{Curl}\overline{\tau}(x,y) + \text{Curl}\tau{}'(x,y,t)$$

The overbar means time-averaged over the duration of the numerical experiment, and the prime designs the pertubation from the mean (or eddy part).

Therefore the pointwise energy equations, which Evans (1984) presented, can be written in their Eulerian form and split into their mean and eddy part. The following energy fields are defined:

$$\overline{K_1}(x,y) = \tfrac{1}{2}H_1(\vec{\nabla \overline{\psi_1}})^2 = \text{kinetic energy of the upper layer mean flow.}$$

$$\overline{K_3}(x,y) = \tfrac{1}{2}H_3(\vec{\nabla \overline{\psi_3}})^2 = \text{kinetic energy of the lower layer mean flow.}$$

$$\overline{P}(x,y) = \tfrac{1}{2}f_0^2/g'(\overline{\psi_1}-\overline{\psi_3})^2 = \text{potential energy of the mean flow.}$$

$$\overline{K}_1{}'(x,y) = \tfrac{1}{2}H_1\overline{(\vec{\nabla}\psi_1{}')^2} = \text{mean kinetic energy of the upper layer eddy flow.}$$

$$\overline{K}_3{}'(x,y) = \tfrac{1}{2}H_3\overline{(\vec{\nabla}\psi_3{}')^2} = \text{mean kinetic energy of the lower layer eddy flow.}$$

$$\overline{P}{}'(x,y) = \tfrac{1}{2}f_o^2/g'\overline{(\psi_1{}'-\psi_3{}')^2} = \text{mean potential energy of the eddy flow.}$$

The energy equations that involve these energy fields are presented in Tables 1, 2 and 3. These equations are obtained by the classical calculation described in the next subsections.

A. Equations for $\overline{K}_1$ and $\overline{K}_3$

The vorticity equations (1) and (2) are multiplied respectively by $-H_1\overline{\psi}_1$ and $-H_3\overline{\psi}_3$ and are then averaged in time over the period of the experiment. The resulting equations are integrated by part to separate their divergence part. After some calculations to make $\overline{K}_1$ and $\overline{K}_3$ appear on the left hand side, the equations for the kinetic energy of the mean flow in each layer have the form shown in Table 1. These equations say that the rate of change of the kinetic energy of the mean flow is the sum of terms that represents local energy transfers plus terms represented by the divergence of an energy flux vector. The energy flux vector is shown in Table 1 in a form somewhat different from that given by Pedlosky (1979) or Evans (1984). But in fact it is quite similar, since the QG approximation implies that the first order flow is nondivergent. For example, the

Coriolis term in Table 1 is equivalent to $\nabla(\frac{1}{2}\beta\psi^2 \mathbf{i})$, which is the form used by Pedlosky and Evans. Pinardi and Robinson (1986) give both forms.

B. Equations for $\overline{K}_1{'}$ and $\overline{K}_3{'}$

Vorticity equations (1) and (2) are multiplied by $-H_1\psi_1{'}$ and $-H_3\psi_3{'}$ and are then averaged in time. The same integration by part and the same calculations to obtain the equation for the mean flow are repeated and yield the kinetic energy equations for the eddy flow shown in Table 2.

C. Equations for $\overline{P}$ and $\overline{P}{'}$.

To obtain the equation for $\overline{P}$ (respectively $\overline{P}{'}$), the continuity equation (3) is multiplied by $\frac{1}{2}f_0^2/g'(\overline{\psi}_1-\overline{\psi}_3)$ (respectively by $\frac{1}{2}f_0^2/g'(\psi_1{'}-\psi_3{'})$) and is then time-averaged. The divergence part is again separated in the equations. The resulting equations for the potential energy are shown in Table 3.

3. DISCUSSION OF THE ENERGY EQUATIONS

When stationary statistics are assumed, the rate of change of the energy is zero, and the equations resume to a global balance between the local transfer and flux terms. The separation of the terms of the equations in those latest two categories is due to the

Table 1a. Equations of the kinetic energy of the upper layer mean flow.

Time rate of change of the kinetic energy of the upper layer mean flow $*\frac{\partial}{\partial t}\overline{K}_1 = \frac{\partial}{\partial t}\left(\frac{H_1}{2}(\vec{\nabla\psi}_1)^2\right)$ = sum of the following terms.

$f_o \frac{H_1}{H}(\overline{\psi}_1-\overline{\psi}_3)\overline{w}_2$	Work done by buoyancy forces. Conversion $\overline{P} \to \overline{K}_1$	Local energy transfers
$f_o \overline{\psi}_2\overline{w}_2$	Work done by pressure forces at the interface. Conversion $\overline{K}_3 \to \overline{K}_1$	
$-H_1\overline{\psi}_1\overline{J(\nabla^2\psi'_1,\psi'_1)}$	Work done by the Reynolds stresses. Conversion $\overline{K}'_1 \to \overline{K}_1$	
$-\overline{\psi}_1$ Curl $\overline{\tau}$	Energy transfer rate from mean surface wind to upper layer ocean.	
$-AH_1\vec{\overline{G}}_1\vec{\nabla\psi}_1$	Dissipation of $\overline{K}_1$ by lateral friction.	
$*\vec{\nabla}\left(H_1\overline{\psi}_1\vec{\nabla}(\overline{\partial\psi_1/\partial t})\right)$	Pressure working rate due to the mean acceleration of the flow.	Energy flux vector
$\vec{\nabla}(H_1\overline{\psi}_1f\vec{\overline{U}}_1)$	Pressure working rate due to the acceleration of the mean flow by the Coriolis force.	
$\vec{\nabla}(H_1\overline{\psi}_1\nabla^2\overline{\psi}_1\vec{\overline{U}}_1)$	Advection of $\overline{K}_1$ by the mean flow.	
$\vec{\nabla}(AH_1\overline{\psi}_1\vec{\overline{G}}_1)$	Pressure working rate due to the decceleration of the mean flow by friction.	

Vector $\vec{\overline{G}}_i$ is introduced after Evans (1980) to condense the notations.

$$\vec{\overline{G}}_i = \left(\frac{\partial^5\overline{\psi}_i}{\partial x^5} + \frac{\partial^5\overline{\psi}_i}{\partial x^3\partial y^1}; \frac{\partial^5\overline{\psi}_i}{\partial y^5} + \frac{\partial^5\overline{\psi}_i}{\partial y^3\partial x^2}\right) \quad i = 1,3$$

*In the case of stationary statistics, these terms have zero value.

Time rate of change of the kinetic energy of the lower layer mean flow $*\frac{\partial}{\partial t}\overline{K}_3 = \frac{\partial}{\partial t}\left(\frac{H_3}{2}(\nabla\overline{\psi}_3)^2\right)$ = sum of the following terms		
$f_o\frac{H_3}{H}(\overline{\psi}_1-\overline{\psi}_3)\overline{w}_2$	Work done by buoyancy forces. Conversion $\overline{P} \rightarrow \overline{K}_3$	Local energy transfers
$-f_o\overline{\psi}_2\overline{w}_2$	Work done by pressure forces at the interface. Conversion $\overline{K}_1 \rightarrow \overline{K}_3$	
$-H_3\overline{\psi}_3\overline{J(\nabla^2\psi_3',\psi_3')}$	Work done by the Reynolds stresses. Conversion $\overline{K}_3' \rightarrow \overline{K}_3$	
$-\varepsilon_3 H_3(\nabla\overline{\psi}_3)^2$	Dissipation of $\overline{K}_1$ by bottom friction.	
$-AH_3\overline{\vec{G}}_3\vec{\nabla\psi}_3$	Dissipation of $\overline{K}_1$ by lateral friction	
$*\vec{\nabla}\left(H_3\overline{\psi}_3\vec{\nabla}(\overline{\partial\psi_3/\partial t})\right)$	Pressure working rate due to the mean acceleration of the flow.	Energy flux vector
$\vec{\nabla}\left(H_3\overline{\psi}_3(f+f_o\frac{h_B}{H_3})\vec{\overline{U}}_3\right)$	Pressure work due to the acceleration of the mean flow by Coriolis force and topography.	
$\vec{\nabla}(H_3\overline{\psi}_3\nabla^2\overline{\psi}_3\vec{\overline{U}}_3)$	Advection of $\overline{K}_3$ by the mean flow.	
$\vec{\nabla}(AH_3\overline{\psi}_3\vec{\overline{G}}_3)$	Pressure working rate due to the decceleration of the mean flow by lateral friction.	
$\vec{\nabla}(\varepsilon_3 H_3\overline{\psi}_3\vec{\nabla\psi}_3)$	Pressure working rate due to the decceleration of the mean flow by bottom friction.	

*In the case of stationary statistics, these terms have zero value.

<div align="center">

Table 2a. Equations of the mean kinetic energy
of the upper layer eddy flow.

</div>

Time rate of change of the mean kinetic energy of the upper layer eddy flow $\dfrac{*\overline{\partial K_1}}{\partial t} = \dfrac{\partial}{\partial t}\left(\overline{\dfrac{H_1}{2}(\vec{\nabla}\psi_1')^2}\right)$ = sum of the following terms.		
$f_o\dfrac{H_1}{H}\overline{(\psi_1'-\psi_3')w_2'}$	Work done by buoyancy forces. Conversion $\overline{P}' \rightarrow \overline{K_1'}$	Local energy transfers
$f_o\overline{\psi_2'w_2'}$	Work done by pressure forces at the interface. Conversion $\overline{K_3'} \rightarrow \overline{K_1'}$	
$H_1\overline{\psi_1 J(\nabla^2\psi_1',\psi_1')}$	Work done by the Reynolds stresses. Conversion $\overline{K_1} \rightarrow \overline{K_1'}$	
$-\overline{\psi_1'\ \mathrm{Curl}\tau'}$	Energy transfer rate from perturbation wind to upper layer ocean.	
$-AH_1\overline{\vec{G}_1'\cdot\vec{\nabla}\psi_1'}$	Dissipation of $\overline{K_1'}$ by lateral friction.	
$^*\vec{\nabla}\left(H_1\overline{\psi_1'\vec{\nabla}(\partial\psi_1'/\partial t)}\right)$	Pressure working rate due to the acceleration of the eddy flow.	Energy flux vector
$\vec{\nabla}(H_1\overline{\psi_1'f\vec{U}_1'})$	Pressure working rate due to the acceleration of the eddy flow by the Coriolis force.	
$\vec{\nabla}(H_1\nabla^2\overline{\psi}_1\ \overline{\psi_1'\vec{U}_1'})$ $\vec{\nabla}(H_1\overline{\psi}_1\overline{\nabla^2\psi_1'\vec{U}_1'})$ $\Bigg\}$	Pressure working rate due to the acceleration of the eddy flow by the Reynolds stresses.	
$\vec{\nabla}(H_1\overline{\psi_1'\nabla^2\psi_1'}\vec{U}_1)$	Advection of $\overline{K_1'}$ by the mean flow.	
$\vec{\nabla}(H_1\overline{\psi_1'\nabla^2\psi_1'\vec{U}_1'})$	Advection of $\overline{K_1'}$ by the eddy flow.	
$\nabla(AH_1\overline{\psi_1'\vec{G}_1'})$	Presure working rate due to the decceleration of the eddy flow by lateral friction.	

Vector $\overline{\vec{G}}_i'$ is introduced to condense the notations.

$$\vec{G}'_i = \left(\frac{\partial^5\psi_i'}{\partial x^5} + \frac{\partial^5\psi_i'}{\partial x^3\partial y^2}, \frac{\partial^5\psi'_i}{\partial y^5} + \frac{\partial^5\psi'_i}{\partial y^3\partial x^2}\right)\ i = 1,3$$

*In the case of stationary statistics these terms have a zero value.

Table 2b. Equations of the mean kinetic energy of the
lower layer eddy flow.

Time rate of change of the mean kinetic energy of the lower layer eddy flow $\overset{*}{\dfrac{\partial K_3'}{\partial t}} = \dfrac{\partial}{\partial t}\left(\overline{\dfrac{H_3}{2}(\vec{\nabla}\psi_3')^2}\right)$ = sum of the following terms.		
$f_o\dfrac{H_3}{H}\overline{(\psi_1'-\psi_3')w_2'}$	Work done by buoyancy forces. Conversion $\overline{P}' \rightarrow \overline{K_3'}$	Local energy transfers
$-f_o\overline{\psi_2'w_2'}$	Work done by pressure forces at the interface. Conversion $\overline{K_1'} \rightarrow \overline{K_3'}$	
$H_3\overline{\psi_3}\overline{J(\nabla^2\psi_3',\psi_3')}$	Work done by the Reynolds stresses. Conversion $\overline{K_3} \rightarrow \overline{K_3'}$	
$-\varepsilon_3 H_3\overline{(\vec{\nabla}\psi_3)^2}$	Dissipation of $\overline{K_3'}$ by bottom friction	
$-AH_3\overline{\vec{G}_3'\cdot\vec{\nabla}\psi_3'}$	Dissipation of K_3' by lateral friction.	
$\overset{*}{\vec{\nabla}\left(H_3\psi_3'\vec{\nabla}(\partial\psi_3'/\partial t)\right)}$	Pressure working rate due to the acceleration of the eddy flow.	Energy flux vector
$\vec{\nabla}\left(H_3(f+f_o\dfrac{h_B}{H_3})\overline{\psi_3'\vec{U}_3'}\right)$	Pressure working rate due to the acceleration of the eddy flow by Coriolis force and topography.	
$\vec{\nabla}(H_3\nabla^2\overline{\psi_3}\ \overline{\psi_3'\vec{U}_3'})$ $\left.\vphantom{\begin{matrix}a\\b\\c\end{matrix}}\right\}$	Pressure working rate due to the acceleration of the eddy flow by the Reynolds stresses.	
$\vec{\nabla}(H_3\overline{\psi_3}\overline{\nabla^2\psi_3'\vec{U}_3'})$		
$\vec{\nabla}(H_3\overline{\psi_3'\nabla^2\psi_3'}\ \vec{U}_3$	Advection of $\overline{K_3'}$ by the mean flow.	
$\nabla(H_3\overline{\psi_3'\nabla^2\psi_3'\vec{U}_3'}$	Advection of $\overline{K_3'}$ by the eddy flow.	
$\nabla(AH_3\overline{\psi_3'\vec{G}_3'})$	Pressure working rate due to the decceleration of the eddy flow by lateral friction.	
$\vec{\nabla}(\varepsilon_3 H_3\overline{\psi_3'\vec{\nabla}\psi_3'})$	Pressure working rate due to the decceleration of the eddy flow by bottom friction.	

*In the case of stationary statistics these terms have a zero value.

Table 3a. Equations of the potential energy
of the mean flow.

Time rate of change of the potential energy of the mean

flow $\dfrac{\partial \overline{P}}{\partial t} = \dfrac{\partial}{\partial t}\left(\dfrac{f_o^2}{2g'}(\overline{\psi}_1 - \overline{\psi}_3)^2\right)$ = sum of the following terms

$-f_o(\overline{\psi}_1 - \overline{\psi}_3)\overline{w}_2$	Work done by buoyancy forces. Conversion $\overline{K}_1 + \overline{K}_3 \rightarrow \overline{P}$
$\dfrac{f_o^2}{g'}(\overline{\psi}_1 - \overline{\psi}_3)\ \overline{J(\psi_1', \psi_3')}$	Vertical pressure working rate (Baroclinic processes). Conversion $P' \rightarrow \overline{P}$
$-\vec{\nabla}\left(\dfrac{f_o^2}{2g'}(\overline{\psi}_1 - \overline{\psi}_3)^2 \overline{\vec{U}_2}\right)$	Advection of $\overline{P}$ by the mean flow.

Table 3b. Equations of the potential
energy of the eddy flow.

Time rate of change of the potential energy of the eddy flow $\dfrac{\partial \overline{P'}}{\partial t} = \dfrac{\partial}{\partial t}\left(\overline{\dfrac{f_o^2}{2g'}(\psi_1' - \psi_3')^2}\right)$ = sum of the following terms.	
$-\overline{f_o(\psi_1' - \psi_3')w_2'}$	Work done by byoyancy forces. Conversion $\overline{K}_1' + \overline{K}_3' \rightarrow \overline{P}'$
$-\dfrac{f_o^2}{g'}(\overline{\psi}_1 - \overline{\psi}_3)\;\overline{J(\psi_1', \psi_3')}$	Vertical pressure working rate. (Baroclinic processes). Conversion $\overline{P} \rightarrow \overline{P}'$
$-\vec{\nabla}\left(\overline{\dfrac{f_o^2}{2g'}(\psi_1' - \psi_1')^2 \vec{U}_2'}\right)$	Advection of $\overline{P}'$ by the eddy flow.
$-\vec{\nabla}\left(\dfrac{f_o^2}{2g'}\overline{(\psi_1' - \psi_3')^2} \vec{\overline{U}}_2\right)$	Advection of $\overline{P}'$ by the mean flow.
$-\vec{\nabla}\left(\dfrac{f_o^2}{2g'}(\overline{\psi}_1 - \overline{\psi}_3)\overline{(\psi_1' - \psi_3')\vec{U}_2'}\right)$	

different physics they represent. The local energy transfer terms describe the pointwise rate of change of the energy due to local interaction processes which convert the energy into a different form or dissipate it (sources and sinks). Conversely, the flux terms appear like the divergence of a global energy flux vector and represent an advective and radiative rate of change of the energy.

A. The Local Transfer Rates

When an interaction process is represented by some terms with opposite sign in two of the energy equations, it is regarded as a conversion between those two forms of energy. For example, the working rate of the pressure force acting at the interface (term $f_o\bar{\psi}_2\bar{w}_2$ in table 1) appears with a different sign in both the equations of the kinetic energy of the upper and lower layers. This term is thus regarded as a conversion term which represents a process that transfers kinetic energy from one layer to the other (conversion $\bar{K}_3 \longrightarrow \bar{K}_1$). All the conversion terms of Tables 1, 2 and 3 are so defined. Therefore all the local energy transfer rates of the tables represent a conversion process between two different forms of energy or a local dissipation of energy.

Plotting maps of the different energy transfer rates is useful to determine which dynamics drive the circulation of a given ocean region. The examples shown here are drawn from the ridge experiment described in section 4 of the main study. Fig. 1 presents the

TRANSFER WIND ⟶ EKE1
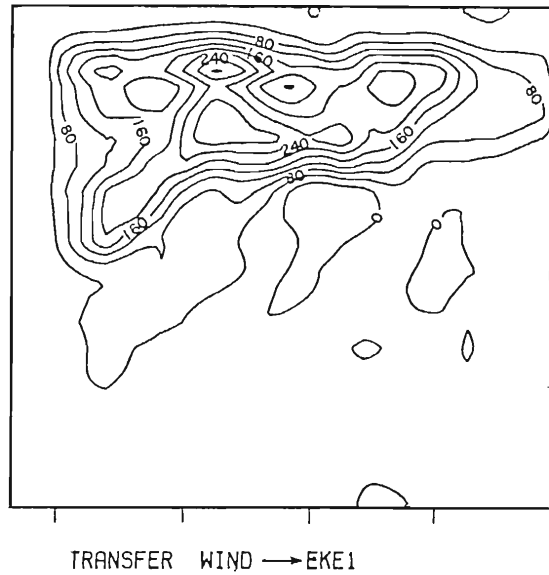
Figure 1. Energy transfer rate from the wind fluctuations into the upper layer eddy kinetic energy in the ridge experiment of the main study. It corresponds to the 4th term of table 2a. Units are $m(m^2sec^{-2})/sec$. CI is 0.4×10^{-7}. Labels are scaled by 10^{10}.

TRANSFER   EKE1 ⟶ EKE3
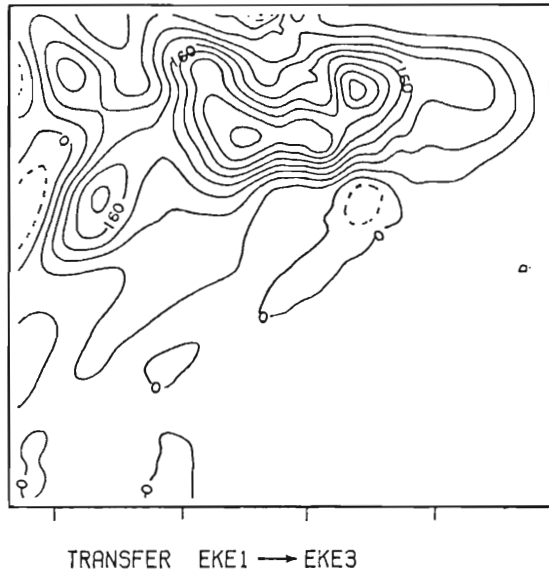
Figure 2.   Transfer rate of eddy kinetic energy from the upper layer
to the lower layer in the ridge experiment of the main study.   It
corresponds the second term of table 2b; $\overline{K'_1} \longrightarrow \overline{K'_3}$ (positive values
mean the transfer is like indicated by the arrow).   Units and CI like
are in Fig. 1.

TRANSFER   MKE3 → EKE3
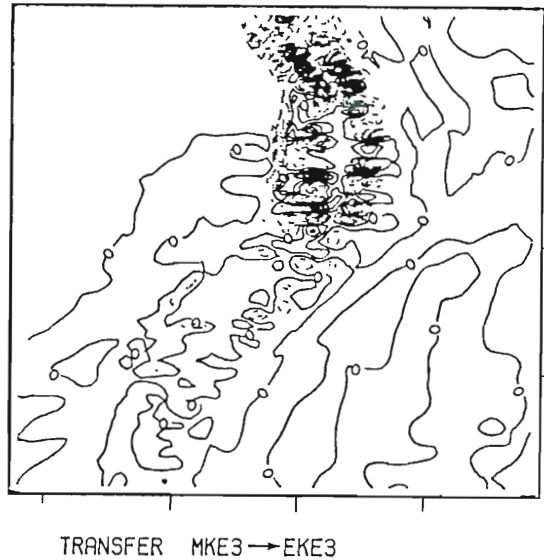
Figure 3.   Transfer rate from the mean kinetic energy to the eddy kinetic energy in the lower layer for the ridge experiment of the main study.   Positive values indicate shear instabilities $(\overline{K_3} \longrightarrow \overline{K_3^!})$ and negative values $(\overline{K_3^!} \longrightarrow \overline{K_3})$ eddy driven mean flow. It corresponds to the third term in table 1b.   Units are in $m(m^2 sec^{-2})/sec$.   CI is $2x10^{-11}$.

transfer rate of eddy energy from the fluctuating winds to the upper

layer (4th term in Table 2), and Fig. 2 shows the transfer rate of

eddy energy from the upper to the lower layer. Those maps say that

the circulation is wind driven, which means the energy is input from

the wind into the upper layer, then into the lower layer, by the

pressure forces at the interface. Nevertheless, the small negative

transfer that is noticeable over the ridge in Fig. 2 indicates that

the circulation is bottom driven in that region. Fig. 3 shows the

transfer rate between the mean and the eddy kinetic energy in the

lower layer. Positive contours mean occurrence of shear

instabilities, whereas negative contours indicate non-linear

rectification. The low values of the transfer rates of Fig. 3

compared to those of Fig. 1 and Fig. 2 indicate that those non-linear

phenomena play a small role in the experiment. The calculations can

be performed on low-pass (or high-pass) filtered data sets in order

to investigate the dynamics of low-frequency (or high frequency)

motions.

B.   The Energy Flux Vector

The rate of change of the energy which is not due to local

transfers can be written like the divergence of an energy flux

vector. Any nondivergent vector can be added to that vector without

changing the energy equations. It contains advective fluxes

(advection of mean and eddy energy by the mean/eddy flow) and
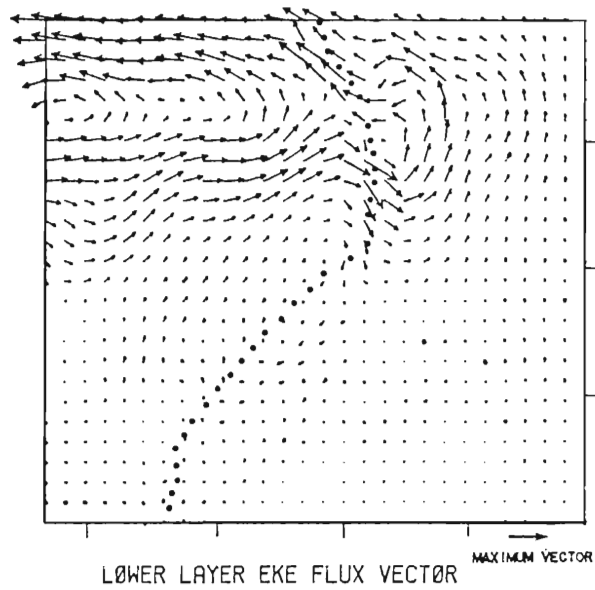
LØWER LAYER EKE FLUX VECTØR   MAXIMUM VECTOR

Figure 4. Total lower layer eddy kinetic energy flux vector for the ridge experiment of the main study. It represents the sum of all the flux vectors of table 2b. The ridge crest is the heavy dotted line. Maximum vector length is 4.35 $m^2(m^2sec^{-2})$/sec.

radiative fluxes in the form of pressure work done by the ageostrophic fields (acceleration and decceleration of the flow). The energy flux vector is seldom used except in simple cases like linear Rossby waves where it reduces to energy density multiplied by the group velocity. It may not be useful to plot the vector itself, since any nondivergent vector can be added to it. For example, Fig. 4 shows the lower layer total eddy kinetic energy flux vector (sum of all the terms in Table 2). The interesting feature is the circular pattern east of the ridge which indicates energy trapping or energy reflexion. The divergence of that vector is more useful. The regions of positive contours are regions where energy comes in; negative contours indicate that the energy is radiating out. Fig 5 shows the divergence of the energy vector of Fig. 4. The circular pattern mentioned in the vector plot is associated with a large negative region which indicates energy reflexion and dissipation. The northern and central part of the ridge present positive values which are attributed to trapped topographic waves.

DIVERGENCE ØF EKE3 FLUX VECTØR

Figure 5. Divergence of the lower layer eddy kinetic energy flux
vector displayed in Fig. 4. Positive values indicate that energy is
radiated into the region. Negative values indicate that energy
radiates out. Units are in $m(m^2 sec^{-2})/sec$. CI is 10^{-7}.

REFERENCES

Evans, J. C., On the interaction of cyclonic rings with the Gulf
Stream recirculation, Ph.D. dissertation, The Florida State
University, 1984.

Harrison, D. E., and A. R. Robinson, Energy analysis of open regions
of turbulent flows. Mean eddy energetics of a numerical ocean
circulation experiment, Dyn. Atm. Oceans, 2, 185-211, 1978.

Holland, R. H., The role of mesoscale eddies in the general
circulation of the ocean- Numerical experiment using a wind-
driven quasi-geostrophic model, J. Phys. Oceanogr., 8, 363-392,
1978.

Pedlosky, J., Geophysical Fluid Dynamics, 624 pp., Springer-Verlag,
New York, 1979.

Pinardi, N., and A. R. Robinson, 1986: Quasi-geostrophic energetics
of open ocean regions. Submitted for publication.

APPENDIX B

TESTING A SPONGE LAYER IN A TWO-LAYER
QUASI-GEOSTROPHIC MODEL

ABSTRACT

This paper shows how a sponge layer has been designed and tested
in a non-linear, two-layer, quasi-geostrophic numerical ocean
model. In the sponge layer the fluid motion is damped by an enhanced
barotropic friction similar to the linear bottom friction. The
parameters that define the sponge are its width, the values of the
friction coefficients inside the sponge, and the width of the domain
over which these coefficients increase from their small values
outside the sponge to their large values inside. A set of values for
these parameters is used to test the effects of a western sponge
layer on a westward fast propagating barotropic Rossby wave and a
non-linear, quasi-geostrophic eddy moving westward.

LIST OF FIGURES

Figure 1: Diagram for the vertical structure of the 2-layer, quasi-geostrophique model. Fig. 1b: The basin on which the governing equations are integrated. The box-size is 1760 km. The eastern (unshaded) region is the interior ocean where the governing equations hold. The western (shaded) region is the sponge layer where enhanced barotropic damping occurs. Fig. 1c: The zonal variation of the bottom-like friction coefficients. Top curve for the upper layer $(\epsilon_1(x)$ is plotted$)$. Bottom curve for the lower layer $(\epsilon_3(x)$ is plotted$)$. Units are in 10^{-6} sec^{-1}.

Figure 2: The damping of a 96 day period barotropic Rossby wave. At T=0 the wave, continuously forced near the eastern boundary, only fills in the eastern part of the basin. a(left): No sponge layer. The upper layer vorticity (top) and streamfunction (bottom) after 1 period (96 days) and 4 periods (384 days) are plotted. Reflexion is noticeable at the western boundary. b(right): Sponge

layer to the west. The same plotting than on the left.
No reflexion is noticeable at the western boundary.
The wave is damped before it crosses the sponge.
Contour interval are in 0.335×10^{-6} sec^{-1} for the
vorticity and 1000 m^2 sec^{-1} for the streamfunction.

Figure 3: The damping of a westward moving eddy.
The upper layer streamfunction is plotted. The
translation speed of the eddy is westward at 3.16 km/day.
Contour interval is 2500 m^2 sec^{-1}. a) The eddy pattern at
time T=0. b(top): No sponge layer. The evolution of
the eddy over 400 days. c(bottom): Sponge layer.
The damping of the eddy over 400 days.

I. INTRODUCTION

Square-box ocean models have been widely used to investigate the mid-latitude ocean circulation. The efficiency of the Poisson equation solvers in that type of geometry has permitted a considerable reduction of the basic integration time of the numerical models. With the increasing capacity of computers, high resolution models like the Eddy-resolving General Circulation Models (EGC Models) have been developed (Holland, 1978). These models, integrated over long periods (over tens of years), actually improved the understanding of the processes that drive the ocean circulation. But due to the square-box shape of the basin, this type of ocean model does not seem appropriate to perform numerical studies of regional ocean dynamics where the shape of the coast is important and open boundaries are often necessary.

Improvement by the introduction of realistic coasts does increase the computational cost. Also, advancing the square-box models towards more realism would require open boundaries associated with radiation (and not periodic or forced) boundary conditions. But for multi-layer, quasi-geostrophic EGC Models, open boundaries are not yet fully satisfactory and still computationally costly (Verron 1987). However, it is possible, in some special cases, to get around these difficulties by using damping (also called sponge) layers. A

sponge layer is a region of the basin adjoining to a solid boundary where the dynamic is numerically damped so the interior ocean does not feel back the coastal effects (such that wave reflexion). For example, Cummins, Mysak, and Hamilton (1986), in a study of the propagation in the interior Pacific of baroclinic Rossby waves generated at the California coast, used a sponge layer in place of the western boundary in order to integrate their numerical model over forty years without getting back any perturbation from the west.

This paper is to present a few tests that have been performed on sponge layers in a two-layer quasi-geostrophic model. These tests were worked out in the course of a numerical study which investigates the generation of non-linear barotropic and first mode baroclinic Rossby waves in the north-eastern Atlantic and emphasizes the influence of the mid-ocean ridge on the propagation of these waves. In that study, which is performed with a square-box, two-layer, quasi-geostrophic numerical model, sponge layers are used to avoid wave reflexion on the solid boundaries that define the ocean basin.

In an ocean model the western boundary acts like a source of vorticity, in part because it reflects incoming energy at shorter lengthscales. For the above study, the aim was to concentrate on the eastern boundary and the mid-ocean ridge as potential sources of vorticity when the wind forces the flow there. A western sponge layer is used to absorb the energy that occurs on the western boundary in order to surpress the generated vorticity. The first

part of this paper introduces the model equations and describes the design of the sponge layer. The second part shows the damping by a western sponge layer of a barotropic Rossby wave carrying energy westward. The tests are done with barotropic waves because they propagate much faster than baroclinic waves. Also, if the sponge layer surpresses the barotropic waves, it will certainly surpress more efficiently the baroclinic waves which need a longer time to cross the sponge. Finally, the third part of this paper discusses the damping by a western sponge layer of a non-linear, quasi-geostrophic, circular eddy moving westward.

I: THE TWO LAYER MODEL AND THE SPONGE LAYER

A. The Model Equations

Basically, the model is the one presented by Holland (1978). The vertical structure of the model is schematically shown in Fig. 1a. A two-layer ocean with a rigid top and a flat-bottom on the usual β-plane in a closed square basin is considered. The governing equations are the unforced, non-linear, potential vorticity equations for the two layers, coupled by the continuity equation applied at the interface.

$$\partial/\partial t(\nabla^2\psi_1)=J(f+\nabla^2\psi_1,\psi_1)-f_0 w_2/H_1-Am\nabla^6\psi_1 \qquad (1)$$

$$\partial/\partial t(\nabla^2\psi_3)=J(f+\nabla^2\psi_3,\psi_3)+f_0 w_2/H_3-Am\nabla^6\psi_3-\epsilon_3\nabla^2\psi_3 \qquad (2)$$

$$\partial/\partial t(\psi_1-\psi_3)=J(\psi_1-\psi_3,\psi_2)-g'w_2/f_0 \qquad (3)$$

The notations are the following. $H_{1,3}$ are the constant thickness of

Levels in Fig.1a:
- z=0 — LEVEL 0(w=0)
- — LEVEL 1(ψ₁)
- z=-H₁ — LEVEL 2(ψ₂,w₂)
- — LEVEL 3(ψ₃)
- z=-H — LEVEL 4(w=0)
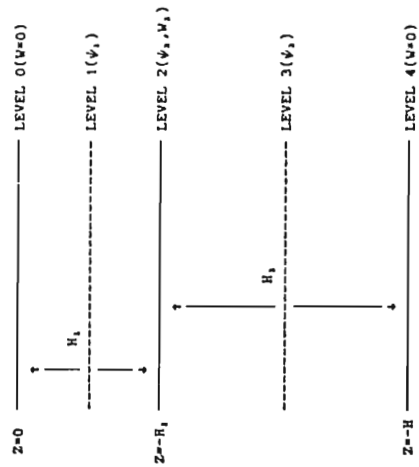
Fig.1a: Diagram for the vertical structure of the 2-layer quasi-geostrophique model (after Holland 1978).
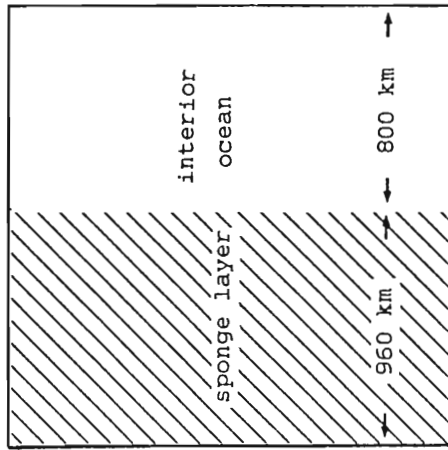
interior ocean

sponge layer

960 km   800 km

Fig.1b: The basin on which the governing equations are integrated. The box-size is 1760km. The eastern (unshaded) region is the interior ocean where the governing equations hold. The western (shaded) region is the sponge layer where enhanced barotropic damping occurs.
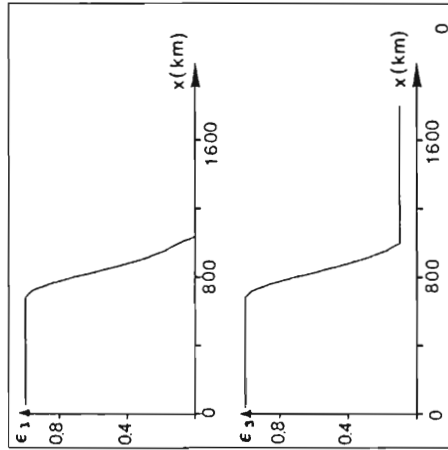
Fig.1c: The zonal variation of the bottom-like friction coefficients. Top curve for the upper layer ($\epsilon_1(x)$ is plotted). Bottom curve for the lower layer ($\epsilon_3(x)$ is plotted). Units are in $10^{-6}\,\mathrm{sec}^{-1}$.

layers 1,3 respectively. The total depth is $H=H_1+H_3$. $\psi_{1,3}$
are the streamfunctions at the various levels shown in Fig. 1a. The
horizontal velocity components are $u_{1,3}=\partial\psi_{1,3}/\partial y$ and
$v_{1,3}=\partial\psi_{1,3}/\partial x$. At the interface, the vertical velocity is w_2, the
streamfunction is given by $\psi_2=(H_3\psi_1+H_2\psi_3)/H$ and the deviation of the
interface height, positive upward, is $h_2=f_0(\psi_3-\psi_1)/g'$.

J is the Jacobian operator. $f=f_0+\beta(y-y_0)$ is the variable
Coriolis parameter (y_0 refers to the mid latitude of the basin
where f_0 and β are calculated). $g'=g\Delta\rho/\rho_0$ is the reduced gravity
(ρ_0=lower layer density and $\Delta\rho$=density difference between the two
layers). The enstrophy cascade towards the small scales is damped by
the biharmonic friction terms. If the eddy viscosity coefficient Am
is adequately chosen, this type of friction damps the grid-scale
waves very rapidly while it leaves the longer waves untouched. The
model dissipates energy mainly by bottom friction.

B. Design of a Sponge Layer

This section describes the design of a western sponge layer.
The same method would be used for a northern or southern sponge
layer. The finite-difference version of the governing equations are
to be integrated in a square basin. Each side of the box is treated
as a solid wall. For the tests the basin has been divided into two
parts. The eastern part of the basin is the interior ocean where the
governing equations hold (unshaded region in Fig. 1b). The western
half of the basin is the domain of the sponge layer where numerically

enhanced damping occurs (shaded region in Fig. 1b). The numerical
damping is ensured by enhanced barotropic linear bottom-friction. As
it is written in the governing equations (1) and (2), bottom friction
directly acts only on the lower layer dynamics. Its effects are
independent of the length-scale of the fluid motion. Its
characteristic damping time-scale is $1/\varepsilon_3$. Thus the bottom friction
in the interior ocean is baroclinic in character.

In the sponge, to ensure a barotropic damping the upper layer
energy must be damped as well. Therefore the upper layer equation
(1) is modified by the addition of a friction term similar to the
bottom friction term of equation (2). The sponge layer equations are
now

$$\partial/\partial t(\nabla^2\psi_1)=-\varepsilon_1\nabla^2\psi_1 \text{ +other terms of (1) unchanged} \qquad (1')$$

$$\partial/\partial t(\nabla^2\psi_3)=-\varepsilon_3\nabla^2\psi_3 \text{ +other terms of (2) unchanged} \qquad (2')$$

Equation (3) is unchanged. Note that for $\varepsilon_1=0$ equations (1')
and (1) are the same.

With $\varepsilon_1=\varepsilon_3$, equations (1') and (2') clearly show that the
damping now acts directly on the barotropic mode and is independent
of the length-scale of the motion. To get an enhanced damping in the
sponge layer, the friction coefficients ε_1 and ε_3 have larger values
in the sponge than in the interior. To prevent energy reflexion at
the limit between the interior and the sponge, the friction
coefficients gradually increase (as a Gaussian) from their interior
(minimum) value ($\varepsilon_1=0$ and $\varepsilon_3=10^{-7}$ sec^{-1} in the tests presented here)

to a maximum value of $\epsilon_{1,3} = 10^{-6}$ sec^{-1} over 320 km and are then constant to that value over the damping layer. This variation is displayed in Fig. 1c.

The damping layer is limited by a solid boundary on the outside where the condition of no flow across the boundary (slip boundary condition) is applied.

For the tests presented here, the box over which the finite-difference version of the governing equations is integrated has a 1760 km side. The grid resolution is 40 km which yeilds an integration domain of 47x47 points for each layer. The interior ocean zonally extends in the eastern part of the basin over 800 km (22 grid-points). The sponge layer covers the western part over 960 km (25 grid-points). The integration time step is 8 hours. Thus one year of integration of the model takes about one minute on a CRAY 1 computer, allowing a sufficient number of tests to select the sponge that gives the best damping for the problem to be solved.

Holland (1978) describes the numerics of the model. The values of the physical parameters used for the integration of the model are the following:

$g' = 2 \times 10^{-2}$ msec^{-2}, $H_1 = 1000$m, $H_3 = 4000$m, $f_o = 0.8854 \times 10^{-4}$ sec^{-1}, $\beta = 1.8 \times 10^{-11}$ m^{-1} sec^{-1}. The eddy viscosity coefficient is $Am = 5 \times 10^{+10}$ m^4 sec^{-1}. For this value of Am the grid-scale wave is damped over a time-step. The values of the bottom friction coefficients in the interior ocean are those mentioned earlier

(ε_1=0 and ε_3=10^{-7} sec^{-1}, which corresponds to an interior damping

time-scale of 116 days for the lower layer). In the sponge layer

these values are $\varepsilon_{1,3}$=10^{-6} sec^{-1}, which gives a damping time-scale of

12 days (36 time-steps) for the barotropic mode.

II. DAMPING OF A BAROTROPIC ROSSBY WAVE

This section presents the damping of a barotropic Rossby wave

which propagates energy westward. A wave source is continuously

maintained near the eastern boundary while the model is integrated.

In the experiments shown here, the source generates a barotropic wave

with a period of 96 days, a zonal wavelength of 2640 km, and a

meridional wavelength of half the basin. The group velocity is

Cg=22km/day. Time T=0 of the experiment is the time when the wave is

at 960 km from the western boundary (which means that the wave enters

the sponge at time T=0).

First the integration is done with no sponge layer (Fig. 2a).

The wave reaches the western boundary in less than a period and is

reflected in a wave of shorter wavelength which propagates energy

eastward at a much smaller group velocity (Cg≈3km/day).

(In Fig. 2a wave reflexion is apparent from the large values of

vorticity at the western boundary). After 4 periods (T=384), the

reflected wave still did not reach the middle of the basin.

Then the same experiment is run with the sponge layer (Fig.

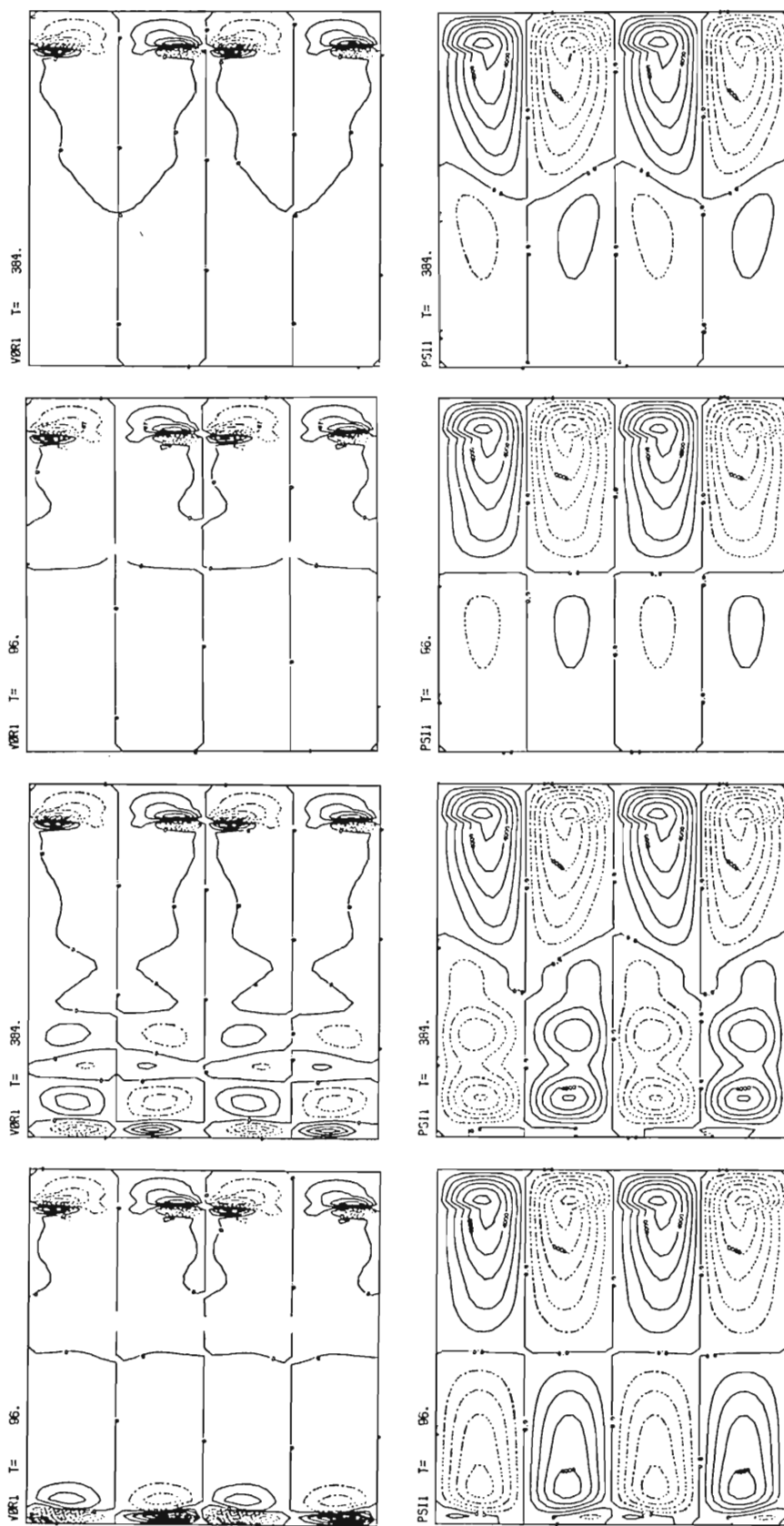2b). In that case, the wave never reaches the western boundary. The

Fig.2: The damping of a 96 day period barotropic Rossby wave. The flow pattern at T=0 is not plotted but the wave, continuously forced near the eastern boundary, only fills in the eastern half of the basin.

a(left): No sponge layer. Is plotted the upper layer vorticity (top) and streamfunction (bottom) after 1 period (96 days) and 4 periods (384 days). Reflexion is noticeable at the western boundary.

b(right): Sponge layer to the west. The same plotting than on the left. No reflexion is noticeable at the western boundary. The wave is damped before it crosses the sponge.

Contour interval are in 0.335x10⁻⁶sec⁻¹ for the vorticity and 1000 m²sec⁻¹ for the streamfunction.

absence of vorticity at the western boundary clearly shows that no wave reflextion occurs there. The incoming energy is continuously damped in the sponge. No reflexion is noticeable at the transition between the interior ocean and the damping layer. After 4 periods (T=384), the pattern of the flow still looks very much like the initial flow. (The little discrepancies noticeable in the flow pattern of Fig. 2 at T=96 and T=384 are not as a result of the sponge layer. They are due to the spin-up adjustment of the model and are also present in the case of the experiment with no sponge. The pictures of the flow pattern after 2, 3, and more periods are exactly the same as the picture shown at T=384).

It must be pointed out that, in the example shown here, the incident wave is damped even before it reaches the western boundary. Faster waves (of longer wavelength) can reach the western boundary before being totally damped, but their reflected waves (of shorter wavlength) are much slower and will vanish when returning back across the sponge layer. As designed in this test, the sponge layer will damp the fastest barotropic Rossby wave of a basin of 4000 km width and thus will surpress the normal modes of such a basin.

III. DAMPING OF A BAROCLINIC EDDY

This section presents the damping of a baroclinic, non-linear, quasi-geostrophic eddy. Oceanic non-linear structures are known to be very coherent and to have a long lifetime. Thus it is interesting to see how a sponge layer, which is very efficient on Rossby waves,

PSI1 T= 400.

PSI1 T= 240.

PSI1 T= 80.

PSI1 T= 400.

PSI1 T= 240.

PSI1 T= 80.

PSI1 T= 0.
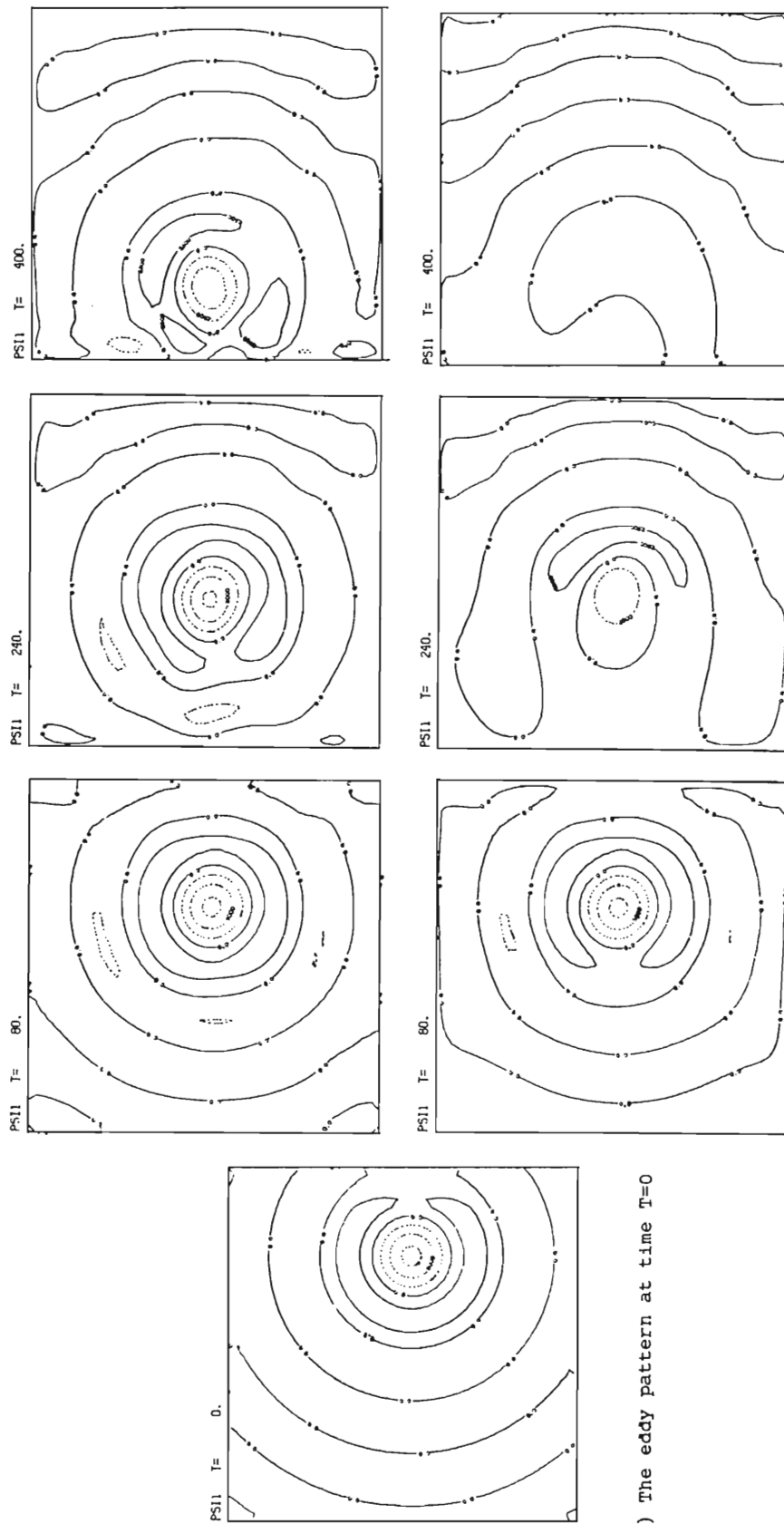
a) The eddy pattern at time T=0

Fig.3: The damping of a westward moving eddy. Is plotted the upper layer streamfunction. The translation speed of the eddy is westward at 3.16 km/day. Contour interval is 2500 m²sec⁻¹.

b-top: No sponge layer. The evolution of the eddy over 400 days.
c-bottom: Sponge layer. The damping of the eddy over 400 days.

acts on a non-linear eddy.

The experiment is done as it follows. At time T=0 the upper and lower streamfunctions are initialized with a non-linear eddy with the analytical expression:

$$\psi_1 = \psi_0 (1-\delta) J_0(r/R_0) \qquad\qquad \psi_3 = -\psi_0 \delta J_0(r/R_0) \qquad\qquad (4)$$

where ψ_0 is the amplitude of the streamfuction, δ is the aspect ratio (H_1/H), r is the distance to the center of the eddy, and R_0 is a parameter that fixes the radius and the translation speed of the eddy. J_0 is the Bessel function of order zero. Equation (4) is an exact solution of the frictionless version of the governing equations in an infinite domain. The upper layer streamfunction at T=0 is shown in Fig. 3a. The eddy, centered at 300 km off the eastern boundary, is cyclonic, its radius is 200 km, and its translation speed is 3.16 km/day. The lower layer streamfunction (not shown here) is like an anticyclonic eddy, much weaker in intensity than the upper layer eddy because of the aspect ratio coefficient in equation (4) (which means that the total vorticity of the eddy is zero).

After initialisation the eddy is left to itself while the model is integrated. The evolution with time of the eddy in the case of no western sponge layer is displayed in Fig. 3b. Only the upper streamfunction is shown. The eddy moves westward, reaches, and starts to interact with the western boundary after less than 400 days. The case of the sponge layer is illustrated in Fig. 3c. Here also only the upper streamfunction is displayed. The eddy is damped

over 400 days, before it even reaches the western boundary. Events
in the lower layer are similar to those described for the upper
layer.

IV.   CONCLUSION

This paper showed how a sponge layer was designed and tested in
a two-layer, quasi-geostrophic ocean model. The purpose of the
sponge is to damp the westward propagating Rossby waves at the
western boundary in order to prevent their reflexion. The sponge, as
it is designed in this study, damps the fast barotropic waves and
non-linear eddies relatively well. The parameters which define the
sponge are its width (960km), the maximum value of the friction
coefficients that ensure the enhanced barotropic damping
($\varepsilon_{1,3}=10^{-6}\sec^{-1}$), and the width of the domain over which these
coefficients increase from their minimum interior value to their
maximum value in the sponge (320km). It is possible to adjust these
parameters to change the character of the sponge layer. For example,
one may reduce the width of the sponge and increase the maximum value
of the friction coefficients and still have the same efficiency in
damping. But this will increase the reflexion at the transition
region between the interior and the sponge.

The choice of the sponge parameters is in fact dictated by the
main study for which the sponge is being designed. There will be a
compromise between the increase in computational cost due to the
sponge layer and how much wave reflexion is allowed in the model.

For the present case the main study investigates the generation of Rossby waves in the north-eastern Atlantic and the influence of the mid-ocean ridge on the propagation of these waves. The study is performed with a square-box model of 4000 km size. The model is forced with realistic winds and is planned to be integrated over tens of years. Thus over such a long integration and because, for the reasons mentioned in the introduction, it is important to avoid any significant energy which might radiate from the western boundary, the sponge layer must damp all the waves almost completely. Also, the transition from the interior ocean to the sponge layer must not reflect energy. The sponge presented here responds very well to these requirements and increases the computational cost of 20%.

REFERENCES

Cummins, P. F., L. A. Mysak and K. Hamilton, Wind-stress curl
generation of annual Rossby waves in the North Pacific, J. Phys.
Oceanogr., 16, 1179-1189, 1986.

Holland, R. H., The role of mesoscale eddies in the general
circulation of the ocean - Numerical experiment using a wind-
driven quasi-geostrophic model, J. Phys. Oceanogr., 8, 363-392,
1978.

Verron, J., Utilisation de frontières ouvertes pour la simulation
numérique d'un pavé d'océan, to appear in Oceanologica Acta,
1987.